Development of Magnesium-Based Multilayer PVD Coatings for Hydrogen Storage Applications

UNITED KINGDOM · CHINA · MALAYSIA

Christopher M. P. Fry

Thesis submitted to the University of Nottingham for the degree of Doctor of Philosophy

August 2013

Abstract

On the long list of solid-state hydrogen storage materials, magnesium hydride stands out for its relatively high hydrogen storage capacity of 7.7 wt%, combined with the low cost and abundance of magnesium. For practical applications however, issues such as the slow kinetics and the high stability of magnesium hydride must be resolved in order to reduce the potential operating temperatures of a magnesium-based solid-state hydrogen storage system. Catalysis has been widely used to improve the hydrogen storage kinetics and thin film techniques have been used to explore novel structures and combinations of materials in order to improve both the kinetics and thermodynamics of hydrogen storage in magnesium.

The original contribution to knowledge of this work lies in the study and understanding of the evolution of a range of novel thin film multilayer coatings and the effect of the structure, structural evolution and materials on the hydrogen storage properties of these materials, each consisting of 150 layers of magnesium, < 20 nm thick, separated by < 3 nm thick layers of a nickel-rich, iron-based transition metal mix, chromium and vanadium.

The samples, as well as a non-catalysed control sample, were produced by means of magnetron-assisted physical vapour deposition and delaminated from the substrate for volumetric, gravimetric and calorimetric hydrogen cycling measurements. The coatings were analysed both before and after hydrogen cycling to understand the structural evolution of the coatings from highly structured thin film multilayers to flaky thin film particles containing finely distributed nano-crystalline catalyst particles.

The formation of the intermetallic Mg_2Ni in one of the samples was found to be beneficial for the hydrogenation kinetics, whilst the dehydrogenation kinetics were found to be affected mostly by the nano-crystalline transition metal phases that formed in the catalysed samples during hydrogen cycling. This resulted in hydrogenation and dehydrogenation of magnesium hydride in less than 4 and 13 minutes at 250°C with activation energies as low as $60.6 \pm 2.5\,\mathrm{kJ\,mol^{-1}}$.

Acknowledgements

This thesis is dedicated to my grandfather, Mr A. C. Fry.

I would like to thank my supervisors, Prof. David Grant and Prof. Gavin Walker for providing the opportunity and support to carry out the research presented in this work.
Thank you also to Dr Nicholas Botterill and Eminate Ltd for the support in using the PVD coating machinery and to Dr Nigel Neate and Dr Michael Fay for their assistance with the X-ray diffraction and electron microscopy techniques used for sample characterisation.

To my friends and colleagues, especially Dr Andrew Patman, Dr Charles Carpenter, Dr Roberto Gil, Dr Emma Cruddace, Dr Xuanli Luo, Amy Prosser, Christopher Bennett and Joel Hamilton, many thanks for your companionship inside and outside of the laboratories and coffee rooms.

Thank you to my parents and grandparents for their life-long support and guidance and for their continued encouragement, patience and love.

Finally, thank you Amy — my partner, friend and most probably better half. You helped me through incredibly difficult times and brightened up the final years of my PhD with your love, patience and companionship.

This research was undertaken as part of the EPSRC Doctoral Training Centre in Hydrogen, Fuel Cells and their Applications.

Contents

Chapter 1

Introduction

1.1 Sustainable Energy for the 21st Century

In essence most scientists agree upon two simple facts: the fact that the worlds ever-rising CO_2 emissions need to be cut, and the fact that fossil fuel supplies are not endless. Therefore, it is vital that all players within the Energy System, nationally and internationally, find and pave a pathway from conventional (mostly fossil) sources of energy to sustainable ones, thus creating a stable and sustainable energy system.

Many ways of doing this have been proposed and to date none alone can provide the world with an easy, quick, and cost-effective way to solve the energy dilemma it is facing. The available technologies, even in combination, are not able to provide the amount of energy needed to make fossil fuel technologies obsolete; hence for the immediate future solutions need to be found to combine renewable energy technology with clean fossil fuel technology (MacKay, 2009).

With its 2008 climate change act (Great Britain, 2008) the UK government set itself the target of reducing greenhouse gas emissions by 80% with

respect to the levels generated in 1990, which is a phenomenal challenge. Indeed, the year 2012 saw a 3.5% increase in emissions to an equivalent of 552.5 million tonnes of CO_2 (UK DECC, 2013) as a result of an increased use of coal for electricity generation, highlighting, 10 years since the first government white paper on reducing greenhouse gas emissions in 2003, that there is still a long way to go before meeting the 2050 target (DTI, 2003).

The largest single proportion of energy use in the UK is taken up by the transport sector, accounting for 38% of the UK's energy consumption in 2008 (UK DECC, 2009) and 24% of UK CO_2 emissions in 2012 (UK DECC, 2013). The electricity supply sector in contrast accounted for nearly a third of the UK's 2012 CO_2 emissions (UK DECC, 2009), whilst, in 2008, electricity provided only 18% of the UK energy demand (UK DECC, 2009). This highlights one of the potential dangers associated with the current trend towards electrification of the UK's automotive sector — the numbers suggest this might result in a migration of an enormous share of the energy demand onto a more polluting system. Without a dramatic increase in the proportion of clean renewable energy adding to the fuel mix for the UK's electricity generation, a mere 3.3% in 2010 (European Commission and others, 2013), this might result in the opposite of the sought-after reduction in greenhouse gas emissions. There is hope however that the UK will meet its renewables target of 15% by 2020 (European Commission and others, 2013), although an increased electricity demand caused by continued electrification of the transport sector might add to the challenge.

Potential solutions to help de-carbonise the UK's energy system include power generation from wind, solar and geothermal energy, hydroelectricity

(including from tidal and wave kinetics) and renewable biofuels. Technical challenges of harvesting the energy from these sources of renewable energy aside, the intermittency of a lot of these technologies creates a need for energy storage on an enormous scale. Several methods exist, including chemical storage in batteries and combustible fuels, and physical storage in the form of potential or thermal energy. One of the proposed routes to a sustainable energy system is via hydrogen. Not a source of renewable energy in itself, hydrogen may be used as a versatile vector to store and distribute energy from renewable sources.

1.1.1 The Hydrogen Economy

Section 1.1 highlights the need for a change to the UK's energy system in order to reach the country's greenhouse gas emission reduction targets by 2050. This change will be required on a large scale and will involve a great deal of technological as well as political, social and financial challenges.

Fuel	Specific Energy (kWh kg^{-1})	Energy Density (kWh l^{-3})
Liquid Hydrogen	33.3	2.4
Liquid Natural Gas	13.9	5.6
Petrol	12.8	9.5
Diesel	12.6	10.6
Methanol	5.5	4.4

Table 1.1: A comparison between the specific energy and system energy density of different liquid fuels (Edwards *et al.*, 2008)

The large specific energy density of hydrogen compared with other fuels, highlighted in table 1.1, along with the versatility of hydrogen as an energy vector make it attractive as a foundation for a new, renewables-based energy system. Hydrogen can act not only as a combustible fuel, providing heat which can be used directly or converted into useful kinetic and electrical energy, but also in fuel cells, directly producing electricity and heat. This leads to many domestic, transport and industrial applications that can be directly fuelled by hydrogen gas.

Provided the sustainable production and transmission of hydrogen to the end-user can be guaranteed, technical challenges still exist in the efficient and reliable use and storage of hydrogen. Whilst fuel cells are very expensive ($ 1833 kW^{-1} in 2004 (Tsuchiya, 2004)) and, using automotive applications as an example, cannot yet compete with the most modern, diesel-fuelled

internal combustion engines in terms of well-to-wheel efficiency (Rousseau and Sharer, 2004), there is a lot of scope for future development. Tsuchiya (2004) predict a cost of $ 38 kW^{-1} in 2020, which is comparable to the cost of internal combustion engines.

Bossel (2006) describes the scale of the challenge in replacing the current energy system with one based on a hydrogen economy. The same issues, including for example the enormous scale of hydrogen generation however, are also present with the alternative: full electrification of the energy system would require an increase of electricity generation on a similar scale. Both systems have potential advantages and disadvantages but both have in common a chicken-and-egg scenario which is keeping the world's energy system in a vicious circle of fossil-fuel dependence. The impasse can be broken, but that requires a level of commitment to one or more technologies which must be carefully judged in order to avoid a 'lock-in' scenario whereby a large investment is made in one technology making it very difficult to adapt other technologies in years to come. This highlights the importance of continued research into hydrogen and fuel cell technology which can contribute to an incremental process of continuous decarbonisation of the world's energy system and thus help break the vicious circle.

1.2 Hydrogen Storage

Despite the high specific energy of hydrogen (33.3 $kWh\,kg^{-1}$) compared with fossil fuels, as shown in table 1.1, the volumetric energy density of hydrogen gas, even at 200 bar, is only 0.53 $kWh\,l^{-1}$, compared with 9.5 $kWh\,l^{-1}$ and 10.6 $kWh\,l^{-1}$ for petrol and diesel, and even liquid hydrogen has an energy density of only 2.37 $kWh\,l^{-1}$ (Edwards *et al.*, 2008). This highlights the necessity for the development of alternative, more compact and energy efficient methods of storing hydrogen.

Often cited are the targets for on-board hydrogen storage presented by the U.S. Department of Energy (DOE) in 2009 (US DOE, 2009) which are summarised in table 1.2.

Storage Parameter	2017 Target	Ultimate Target
Gravimetric Capacity	5.5 wt%	7.5 wt%
Volumetric Capacity	0.04 $kg(H_2)\,l^{-1}$	0.07 $kg(H_2)\,l^{-1}$
Storage System Cost	\$ 2-4 gge^{-1*}	\$ 2-4 gge^{-1*}
System Fill Time**	3.3 min	2.5 min

Table 1.2: United States Department of Energy hydrogen storage system targets (US DOE, 2009) *gallon gasoline equivalent **for a 5 kg H_2 store

Hydrogen can be stored either in the form of compressed gas, as a liquid, or in a solid form. Whilst, depending on pressure, compressed hydrogen gas can far exceed the gravimetric storage capacity DOE targets with a gravimetric capacity of up to 13 wt% at 800 bar in a lightweight composite cylinder, the volumetric targets cannot be met (Züttel, 2004). Liquefaction of hydrogen can enhance the volumetric storage capacity of hydrogen to up to 0.07 $kg(H_2)\,l^{-1}$, well beyond the DOE targets outlined in table 1.2 whilst gravimetric capacities are said to vary with the size of the tank (Züttel, 2004). By

combining liquefaction and compression technologies, Aceves *et al.* (2010) have been able to produce a storage solution storing ca. 5.7 wt% with a volumetric capacity of 0.033 $kg(H_2)\,l^{-1}$. Liquid storage does however suffer from evaporative losses when the store is not being used (Berry and Aceves, 1998) which necessitates the need for thermally well-insulated storage vessels which will reduce the volumetric capacity of 0.07 $kg(H_2)\,l^{-1}$ listed by Züttel (2004). In addition, both compressed and liquid hydrogen storage systems have energy penalties associated with the compression and liquefaction of hydrogen gas which, depending on the pressures and temperatures employed can exceed 40% lower heating value (LHV) (Heung and Stamford, 2003), as would be the case for the 800 bar storage solution suggested by Züttel (2004). Added to this are safety concerns with high-pressure hydrogen vessels (Varin *et al.*, 2008), venting of the evaporative losses from liquid hydrogen stores (Aceves *et al.*, 2010) and hydrogen embrittlement of metallic pressure vessels and cryogenic containers (Sandí, 2004).

Due to the physical limitations and the energy penalties imposed by compression and liquefaction of hydrogen gas, solid-state hydrogen storage has seen a lot of attention in research laboratories. There are a range of ways to store hydrogen in a solid form, either by physisorption in metal-organic frameworks (MOF), porous carbons, carbon nano-tubes (CNT) and zeolites, or by chemically binding hydrogen to other elements. This can be in the form of complex metal hydrides such as $LiBH_4$, interstitial metal hydrides such as $LaNi_5$ or binary hydride materials such as magnesium (di-)hydride. These materials have the potential of storing large quantities of hydrogen in small volumes and at moderate pressures and temperatures, closer to those required

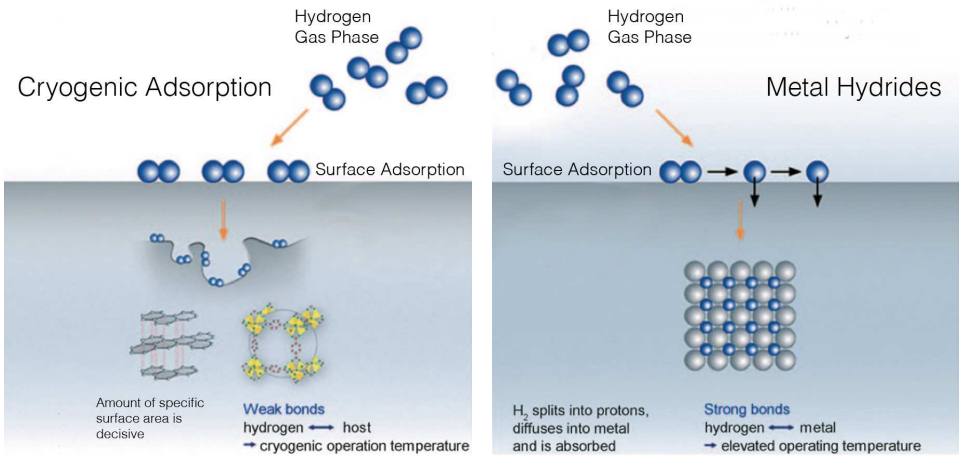

(a) (b)

Figure 1.1: Graph illustrating the processes behind physisorption and chemisorption, adapted from Eberle *et al.* (2009)

for the end application. Figure 1.1 shows a schematic of the the processes behind physisorption and chemisorption adapted from Eberle *et al.* (2009).

1.2.1 Physisorption

Physisorption relies on van der Waals interaction between molecular hydrogen and surfaces. The low enthalpy of adsorption of between 4 and 10 $kJ\,mol^{-1}$ H_2 associated with this type of bond means that hydrogen storage has to take place at low temperatures (Sandrock, 1999). Typical excess hydrogen storage capacities, i.e. the hydrogen that is adsorbed onto the porous material, of up to ca. 7 wt% (Yan *et al.*, 2009) are commonly measured at 77 K which requires a cryogenic storage system incurring energy penalties, albeit notably lower than those incurred by liquefaction. The hydrogen storage capacities of these materials are largely dependent on the surface area of the materials (Züttel, 2004), but the pore geometry has also been shown to

affect the hydrogen storage properties of porous materials (Nijkamp *et al.*, 2001).

Despite the high theoretical gravimetric capacities of up to 7 wt% that have been reported for some of these materials (Yan *et al.*, 2009), volumetric capacities fall short of the DOE targets (Walker, 2008, chapt. 10). Since these porous materials require low temperatures of around 77 K to reach their high gravimetric capacities, in practical applications the cryogenic storage vessel as well as additional heat management hardware will further reduce both the volumetric and gravimetric capacities of these systems.

1.2.2 Chemically Bound Hydrogen

Inherently safe due the high stability of hydride materials, and providing the highest volumetric capacities, chemically bound, solid-state hydrogen storage materials can reversibly store hydrogen without the energy penalties associated with high pressures or low temperatures. Although materials such as $LiBH_4$ can provide as much as 18.5 wt% hydrogen (Orimo *et al.*, 2005), the gravimetric capacity of hydride materials is strongly dependent on the operating temperature, i.e. high-capacity materials generally demand high temperatures to release hydrogen at the required pressures in a short amount of time, and some of the high-capacity, complex hydrides suffer from poor reversibility (Züttel, 2004).

In general, reversible hydrogen storage in metals and alloys is governed by the following equation

$$2\,\mathrm{M} + \mathrm{xH_2} \overset{\Delta H}{\rightleftharpoons} 2\,\mathrm{MH_x}. \tag{1.1}$$

In order for the reaction between hydrogen and a suitable metal to occur, the correct thermodynamic conditions must be fulfilled. The change in the standard Gibbs free energy, which indicates whether or not a reaction will occur, can be used to relate the pressure and temperature of a hydride storage system to the direction of the reaction, i.e. whether, given sufficient metallic or hydride material, hydrogen is released or stored. Given the relationship of the equilibrium constant K with pressure, the following relationship between the equilibrium constant K and the hydrogen pressure can be derived (Andreasen, 2004)

$$K^{-1} = \frac{p_{H_2}}{p^0} \tag{1.2}$$

where p^0 is the the thermodynamic reference pressure (1 bar) and p_{H_2} is the actual hydrogen pressure.

The change in the standard Gibbs free energy ΔG^0 shares the relationship

$$-RT \ln K = \Delta G^0 \tag{1.3}$$

with the equilibrium constant K (Andreasen, 2004).

The change in the standard Gibbs free energy is defined as (Amann *et al.*, 1989)

$$\Delta G^0 = \Delta H^0 - T\Delta S^0 \tag{1.4}$$

which, in conjunction with equation 1.3 can be rearranged to

$$\ln \frac{p_{H_2}}{p^0} = \frac{\Delta H^0}{RT} - \frac{\Delta S^0}{R} \tag{1.5}$$

which is known as the van't Hoff equation (Varin *et al.*, 2008).

Given the standard enthalpy ΔH^0 and entropy ΔS^0, this relationship can be used to derive the equilibrium conditions of the system for a given temperature or pressure, including the often quoted T_{1bar} which is the temperature at which the reaction will occur under atmospheric pressure. By plotting empirical data of $\ln(p)$ vs T^{-1} from the mid-points of the dehydrogenation plateaus of a series of pressure-composition isotherms (PCI), the enthalpy and entropy of the dehydrogenation reaction can be derived from the slope and intercept of the straight line relationship between the data points. The slope of the van't Hoff plot is equal to $\Delta H R^{-1}$, highlighting the thermal stability of the material tested, whilst the intercept is equal to $\Delta S R^{-1}$. ΔS is near-constant for most metal hydrides as it describes the entropy change due to the evolution of hydrogen gas from the hydride material (Grochala and Edwards, 2004).

The mid-point of the dehydrogenation plateau is used to gain an average value for the equilibrium pressure, accounting for the slope and hysteresis often seen in equilibrium curves. The reason for the sloping and hysteresis of the equilibrium curves is explained both in terms of measurement errors and in terms of physical properties. Kinetic limitations result in measurements taken for incomplete reactions which will worsen both the hysteresis and sloping effects which are physically explained by localised defects and surface inhomogeneities in the case of hysteresis and stress due to lattice expansion in the case of the slope of the plateau (Walker, 2008, chapt. 12).

The relationship between the composition of a hydrogen storage material, temperature and pressure is illustrated in figure 1.2, showing a series of PCI measurements with equilibrium curves for a magnesium-based material at

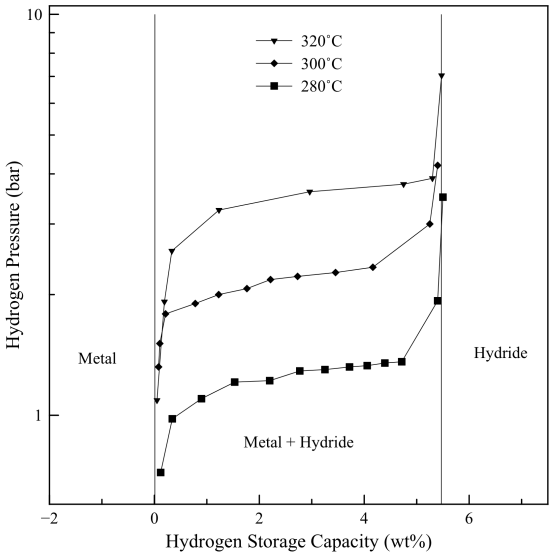

Figure 1.2: Graph showing the general relationship between the pressure, temperature and composition of a hydride material using the values of a catalysed MgH_2 sample

280°C, 300°C and 320°C, taken from this work. For a given temperature, an increase in hydrogen pressure will lead to hydrogen absorption, a decrease in hydrogen pressure will lead to a hydrogen release from a hydride material until the material is either saturated with, or depleted of hydrogen. Similarly, for a given hydrogen pressure, raising the temperature will lead to a release of hydrogen until the equilibrium pressure at the elevated temperature is reached, reducing the temperature leads to hydrogen absorption until the the equilibrium pressure at the reduced temperature is reached, or until saturation or depletion are achieved.

Although the thermodynamics present a very important material property that needs to be considered when choosing materials for hydrogen storage applications, there are other factors that need to be considered. The

reversibility, capacity, cycling stability and the reaction kinetics of materials are arguably equally important (Sandrock, 1999). Whilst the thermodynamics determine the theoretical pressure at which hydrogen is released from a hydride material at a certain temperature, the reaction kinetics determine whether the reaction will happen in a course of minutes, hours, days, months or years, sharing a relationship with temperature. In practise this means, even though a material might in theory release 1 bar of hydrogen at room temperature, the kinetics of the dehydrogenation might require the material to be heated to several hundred °C for any release of hydrogen to occur.

1.2.3 Types of Hydrides

Hydrogen reacts with a whole range of different elements and compounds to form hydrides, with an equally large range of different hydrogen storage properties, cost and abundance. Much research has been done in understanding the properties of many of these hydride materials that exist, assembled in a comprehensive database of existing metal hydride systems and their properties, looked after by the US Department of Energy's Fuel Cell Technologies Program (US DOE, 2013).

The properties of these materials have been widely discussed in the published literature (Grochala and Edwards, 2004; Sakintuna *et al.*, 2007; Sandrock, 1999) and broadly speaking, metal hydrides fall into the three categories of binary hydrides, intermetallic hydrides and complex hydrides, all of which have different properties with associated advantages and disadvantages.

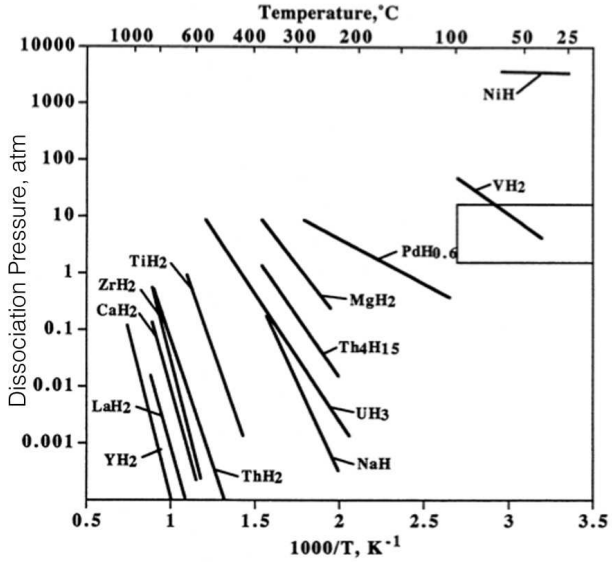

Figure 1.3: Graph comparing the pressure-temperature relationship for a range of different elemental hydrides, adapted from Sandrock (1999)

Binary Hydrides

Binary hydrides are hydrides formed by a single, elemental metal and hydrogen. Many of these hydrides are formed at temperatures and pressures well outside the range for any feasible application or have capacities too low to prove useful. Figure 1.3 highlights the pressure-temperature relationship for a range of different elemental metal hydrides, illustrating that only vanadium (di-)hydride lies within the 1-10 atm, 0-100°C range indicated on the graph (Sandrock, 1999). The low hydrogen storage capacity of 1.9 wt% and the high cost of around \$ 30 kg^{-1} between 2010 and 2013 (Infomine, 2013c) put it well out of reach of hydrogen storage targets as discussed in section 1.2.

Grochala and Edwards (2004) identify a range of these binary hydrides that, based on their potential hydrogen storage capacity, have potential for

future hydrogen storage applications, including lithium, boron, carbon, nitrogen, oxygen, sodium, aluminium and magnesium. The only elemental hydrides that are reversible are identified as LiH and MgH_2 with respective theoretical capacities of 12.7 and 7.7 wt%. Unfortunately, due to the high stability of the compound, lithium hydride releases 1 bar of hydrogen at 910°C which makes it unsuitable for most hydrogen storage applications (Vajo *et al.*, 2004), especially since the material releases aggressive vapours at these temperatures (Grochala and Edwards, 2004). That leaves magnesium as the only fully reversible, high-capacity binary hydrogen storage material that is practical for use in solid-state hydrogen storage applications.

Hydrides of Alloys

In an attempt to alter the extreme nature of either high stability or low stability of many of the hydrides formed by single elements, alloys and solid-solutions of hydride forming materials have been employed to create hydrogen storage materials that will reversibly store hydrogen at the conditions set out by the DOE (Sandrock, 1999). Stoichiometric alloys include compositions of AB_5, AB_2, AB and A_2B, where A is generally a stable hydride forming lanthanide element, calcium or mischmetal, whilst B is a transition metal that forms unstable hydrides (Sandrock, 1999). Much like the hydrides formed by solid-solution alloys which are non-stoichiometric, hydride forming alloys of transition metals which can be 'tuned' to promote hydrogen storage at near-ambient temperatures, the hydrides formed by intermetallics are generally characterised by low hydrogen storage capacities (typically < 2 wt%) due to the heavy elements they are composed of (Sandrock, 1999).

Complex Hydrides

Complex hydrides fall into two groups of ionic compounds formed between transition metals and elements from Group IA or IIA (e.g. Mg_2NiH_4) and those formed by non-transition elements (e.g. $NaBH_4$). Although these complexes can have very high hydrogen storage capacities (up to 18.5 wt% (Orimo *et al.*, 2005)), most suffer from poor reversibility, making them unsuitable for applications where repeated storage and release of hydrogen is required (Sandrock, 1999). Bogdanovic and Schwickardi (1997) show, for their titanium-doped $NaAlH_4$ sample, that the addition of catalysts may allow reversible storage of up to 4.2 wt%, however, the re-hydrogenation requires high pressures exceeding 100 bar and the dehydrogenation kinetics are very slow ($>$ 4 h).

The trade-off between hydrogen storage capacity, weight, cost and energy that is associated with metal hydride systems makes magnesium hydride a prime candidate for the development of new hydrogen storage materials due to its good reversibility coupled with its relatively high hydrogen storage capacity of 7.7 wt% at moderate temperatures (T_{1bar}=284.8°C), the low cost of magnesium (\$ 2-6 kg^{-1} between 2008 and 2013 (Infomine, 2013a)) and its abundance in the earth's crust (1.9 wt% (Fleischer, 1954)). It is for these reasons that magnesium was chosen as a main point of focus for this work.

1.3 Thesis Outline, Aims and Objectives

Following a critical review of the current literature surrounding the use of thin film technology to develop magnesium-based hydrogen storage materials and the effect of transition metal catalysts on the hydrogen storage properties of magnesium hydride in chapter 2, this work primarily explores novel hydrogen storage materials based on thin film multilayer technology. The principal aim is to study the effect of different transition metal catalysts, including nickel, chromium and vanadium, on the hydrogen storage properties of magnesium-based thin film multilayers with a view to understand and improve the hydrogenation and dehydrogenation kinetics of the chemical reaction between magnesium and hydrogen.

The main objectives of this work are to

- Develop a process to enable the production of thin film multilayer materials in a form and quantity suitable for characterisation using machinery designed for analysing powder samples
- Characterise the microstructure, hydrogen storage properties and the resulting microstructural evolution of these materials
- Explore the effects of different catalyst materials on the thermodynamics, capacity and activation of hydrogen storage in magnesium-based thin film multilayers
- Investigate and model the hydrogen storage kinetics and reaction mech-

anisms of transition metal-catalysed magnesium-based thin film multilayers

- Investigate potential advantages of transition metal-catalysed thin film multilayer materials over materials of similar composition in the literature

- Understand the effect of and relationship between the process employed, the materials used, the structural evolution and the hydrogen storage properties of the materials generated

Chapter 3 describes in detail the equipment and parameters used to manufacture and characterise a range of magnesium-based multilayer hydrogen storage materials. Chapter 4 presents the results of in-depth structural characterisation as well as a detailed study of the hydrogen storage properties of these materials which are then discussed in chapter 5 in order to assess the materials' performance and to understand the effect of their composition and microstructure on the hydrogen storage properties. Finally, chapter 6 draws on the findings made and suggests options for future development of next-generation hydrogen storage materials, based on conclusions that are made from this work.

Chapter 2

Literature Review

2.1 Magnesium Hydride

Having established that magnesium hydride is one of the prime candidates for solid-state hydrogen storage materials due to the many virtues including its low cost, high capacity and reversibility, and the abundance of magnesium, it is necessary to look at some of the reasons that are holding researchers back from marketing magnesium hydride as the one-stop quick-fix for the hydrogen storage problem.

Magnesium hydride was first fabricated by pyrolysis of ethyl magnesium halides in 1912 by Jolibois (1912) and many other routes of magnesium hydride production have since been proposed including the direct synthesis of magnesium hydride from elemental magnesium and hydrogen which requires high temperatures and hydrogen pressures (Walker, 2008, chapt. 13). Reactive milling (Huot *et al.*, 1995) has been shown to accelerate the process substantially to a matter of hours as opposed to days (Bouaricha *et al.*, 2001). Eigen *et al.* (2007) stress the importance of economical production of large quantities of light metal hydride materials in the event of the emergence of

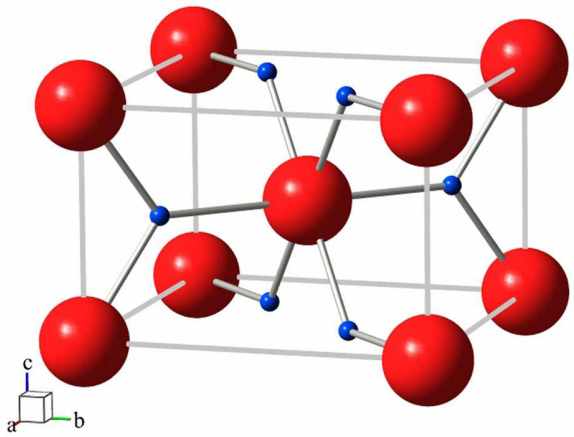

Figure 2.1: Crystal structure of rutile, body-centred tetragonal MgH_2 created using Balls and Sticks (Ozawa and Kang, 2004)

a hydrogen economy including solid-state hydrogen storage. This is an additional factor which adds a further level of complexity to the hydrogen storage problem.

The reaction $Mg + H_2 \overset{\Delta H}{\rightleftharpoons} MgH_2$ occurs when hydrogen atoms, dissociated at the surface of hexagonal close-packed (HCP) magnesium, diffuse into the magnesium lattice, forming a solid solution (α-phase) where hydrogen atoms occupy tetrahedral interstitial sites. This is then followed by the formation of rutile, body-centred tetragonal magnesium hydride (β-phase), with the space group $P4_2/mnm$, and lattice parameters $a = 0.452$ nm and $c = 0.302$ nm (San-Martin and Manchester, 1987), illustrated in figure 2.1.

The hydrogen storage properties of magnesium hydride are characterised by a dehydrogenation enthalpy of $\Delta H = 72.9\,kJ\,mol^{-1}\,H_2$ and an entropy of

$\Delta S = 132.2\,J\,K^{-1}\,mol^{-1}\,H_2$ (Bogdanovic *et al.*, 1999), which, using equation 1.5, results in the release of 1 bar of hydrogen at 278.4°C (T_{1bar}). In reality however, temperatures as high as 400°C are required to hydrogenate and dehydrogenate magnesium, and even at these temperatures the kinetics are very slow, taking several hours to hydrogenate (Zaluska and Zaluski, 1999).

Multiple ways of improving the hydrogen storage properties of magnesium hydride have been proposed, including attempts to speed-up the hydrogenation and dehydrogenation kinetics by modification of the microstructure and catalysis, and the use of thermodynamic destabilisation to promote a drop in T_{1bar}.

2.1.1 Thermodynamic Destabilisation

Following the first synthesis of magnesium hydride from elemental magnesium and hydrogen by Wiberg *et al.* (1951) using a magnesium iodide catalyst, the thermodynamics and kinetics of the reaction between magnesium and hydrogen were first reported by Ellinger *et al.* (1955). Fine magnesium turnings were hydrided under 71 bar of hydrogen at up to 450°C, showing that the materials will react without a catalyst. The hydrogenation enthalpy was measured at ΔH = -67 $kJ\,mol^{-1}\,H_2$ and the kinetics of the reaction were quantified with an activation energy of $E_a = 221.9\,kJ\,mol^{-1}$. Vigeholm *et al.* (1983) further studied the behaviour of magnesium hydride and established a dehydrogenation enthalpy of $\Delta H = 70\,kJ\,mol^{-1}\,H_2$ with a corresponding entropy of $\Delta S = 126\,J\,K^{-1}\,mol^{-1}\,H_2$. Given that the entropy of hydrogen release from magnesium hydride is governed by the evolution of hydrogen from the hydride material (Grochala and Edwards, 2004), with an entropy of $\Delta S =$

130.7 $\mathrm{J\,K^{-1}\,mol^{-1}\,H_2}$, the true value of enthalpy is likely to be slightly higher, in line with the generally accepted enthalpy of dehydrogenation between ΔH = 72.9 $\mathrm{kJ\,mol^{-1}\,H_2}$ (Bogdanovic *et al.*, 1999) and ΔH = 74.5 $\mathrm{kJ\,mol^{-1}\,H_2}$ (Stampfer *et al.*, 1960). A degree of variation might be expected given that these values were measured by different means. Whilst Stampfer *et al.* (1960) used a series of PCIs to measure the enthalpy and entropy of the dehydrogenation reaction as described in section 1.2.2, Bogdanovic *et al.* (1999) used calorimetric methods, showing that, unlike the PCI method, the results are not affected by the particle size of the hydride material.

In order to reduce T_{1bar} it is necessary to reduce the enthalpy of dehydrogenation as the two are directly proportional according to equation 1.5. This has been with done with some success by alloying magnesium with elements such as copper (Reilly and Wiswall, 1967), nickel (Reilly and Wiswall, 1968), aluminium (Tanniru *et al.*, 2010), silicon (Vajo *et al.*, 2004) and germanium (Walker *et al.*, 2011). A dehydrogenation enthalpy of ΔH = 14 $\mathrm{kJ\,mol^{-1}\,H_2}$ was measured for a mixture of magnesium and germanium, corresponding to a T_{1bar} of -91.6°C (Walker *et al.*, 2011).

This is achieved by changing the reaction pathway from $MgH_2 \xrightarrow{\Delta H} Mg + H_2$ to $2\,MgH_2 + Ge \xrightarrow{\Delta H} Mg_2Ge + 2\,H_2$, whereby hydrogen is released via the formation of a new intermetallic Mg_2Ge alloy phase, illustrated in figure 2.2. This considerable reduction however means that hydrogenation of the sample at temperatures that allow sufficiently fast kinetics would have to occur at very high pressures further highlighting the trade-off nature of solid state hydrogen storage media.

An alternative way of reducing the enthalpy of dehydrogenation is pro-

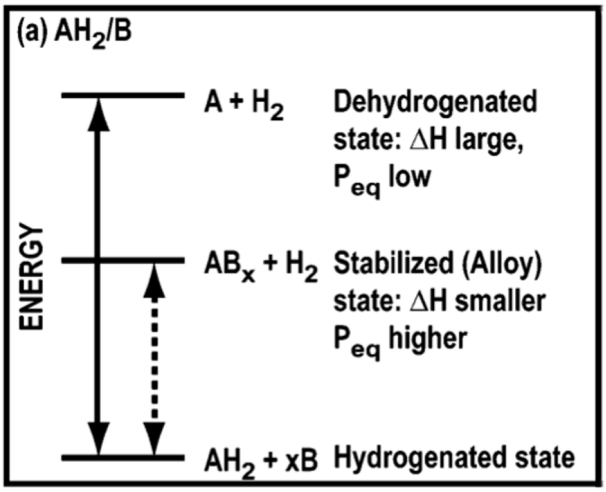

Figure 2.2: Diagram illustrating the destabilisation of a metal hydride through alloy formation (Vajo *et al.*, 2004)

vided by introducing nanostructure and structural defects into magnesium hydride by ball milling. Ball milling is a process whereby the hydride material is ground, often in a planetary arrangement, by a number of steel ball bearings which collide with the hydride material causing repeated fracturing and cold welding of the sample, resulting in a reduced particle- and grain size (Berube *et al.*, 2007). Due to the high-energy nature, the technique can also be used to some degree to promote alloying between different elements and incorporation of catalysts into the hydrogen storage medium.

Varin *et al.* (2006a) manage to reduce the dehydrogenation enthalpy of magnesium hydride with a grain size of 8 nm to $\Delta H = 57\,kJ\,mol^{-1}\,H_2$ by controlled reactive milling for 150 hours, and this reduction in enthalpy has been thoroughly analysed by Berube *et al.* (2008), who use three mechanisms

to explain the phenomenon. They establish a connection between the particle size and the corresponding surface area, the grain size and the corresponding grain boundary energy, and excess volume caused by the formation of non-crystalline regions due to the deformation of the material during ball-milling. This suggests that any destabilisation observed in nano-sized magnesium hydride is a result of excess energy from the ball milling process.

This is supported by calculations showing that, although grain sizes below 10 nm reduce the dehydrogenation enthalpy of magnesium hydride, a reduction to 1 nm lowers the enthalpy by only $5\,\mathrm{kJ\,mol^{-1}\,H_2}$ (Dai *et al.*, 2009). These calculations have been verified by the use of nanoconfinement of magnesium hydride in a matrix of lithium chloride, which results in a reduction of the dehydrogenation enthalpy of magnesium hydride of $2.84\,\mathrm{kJ\,mol^{-1}\,H_2}$ for a grain size of 7 nm (Vajo, 2011). This supports the argument that the destabilisation measured by Varin *et al.* (2006a) is a result of excess energy rather than a true destabilisation of the hydride.

In practise most of these systems have proven to have difficulty with reversibility and cycling stability as well as slow kinetics, which results in the actual temperatures at which hydrogen may be released being well above the theoretical equilibrium temperature for hydrogen release at 1 bar.

2.1.2 Improving Reaction Kinetics

Since, as is established in section 2.1.1, changing the thermodynamic properties of the interaction between magnesium and hydrogen is difficult, alternative ways of improving the hydrogen storage properties of magnesium hydride have been widely studied. By modifying the kinetics of the hydrogenation and dehydrogenation reactions, i.e. accelerating the rate of reaction and reducing the activation energy E_a, hydrogen storage and release in magnesium hydride in less than 2.5 minutes, as demanded by the DOE for transport applications (see table 1.2), might be possible closer to the equilibrium temperature at atmospheric pressure, as opposed to the slow kinetics ($>$ 1 h) observed even at temperatures above 400°C (Zaluska and Zaluski, 1999).

Ball-Milling

There exists a relationship between the particle- and grain size of magnesium hydride and the reaction kinetics, which can be exploited by ball-milling and various other processing routes. Zaluska *et al.* (2001) show a dramatic reduction in the hydrogenation time of ball-milled magnesium powder with a grain size size of less than 50 nm which absorbs 6 wt% in ca. two hours at 300°C, compared with $<$ 0.5 wt% for the micron-sized control sample. A further increase of the reaction rate is achieved with increased grain refinement and Berube *et al.* (2007) conclude that this improvement in hydrogenation kinetics is a result of a combination of the reduced grain size shortening the diffusion pathways of hydrogen through magnesium hydride and the introduction of lattice defects and new surfaces speeding up the nucleation of the hydride phase, limited by the interface energy barrier that has to be

overcome during the nucleation of a new hydride particle. Similarly, the dehydrogenation kinetics are improved by ball milling due to the creation of new surfaces improving the recombination of hydrogen atoms, nucleation sites and diffusion pathways (Berube *et al.*, 2007).

Catalysis

Catalysts modify reaction kinetics and reaction routes without changing the reactants and products of a chemical process, and the addition of catalysts to magnesium hydride has been shown to promote favourable reaction kinetics, often in combination with the reduced particle-and grain size achieved by ball-milling. At the surface of metals, certain catalysts like palladium (Zaluski *et al.*, 1995a) can accelerate the hydrogenation kinetics by promoting the dissociation of hydrogen atoms by what is called the 'spillover effect' (Berube *et al.*, 2007; Mitchell *et al.*, 2003; Zaluska and Zaluski, 1999). This is understood to be the dissociation and chemisorption of hydrogen on and into the catalyst particle followed by the transfer of hydrogen atoms into the bulk of the catalysed material (Gross *et al.*, 2008). In addition, surface catalysts are believed to negate the effect of any passivating layer on the surface of the metal, increasing the resistance to contamination by oxygen (Zaluski *et al.*, 1997). Figure 2.3 illustrates the spillover mechanism by which surface catalysts are believed to accelerate hydrogenation reactions and activation of hydrogen storage materials.

Oxygen contamination has been shown to be responsible for reduced kinetics due to poor dissociation of hydrogen on magnesium oxide (Bazzanella *et al.*, 2011), which can be reversed by activation, involving repeated evacua-

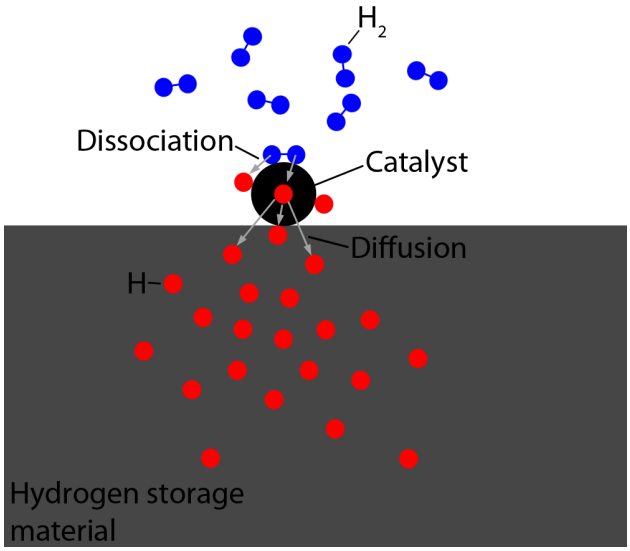

Figure 2.3: Diagram illustrating the 'spillover' effect of a surface catalyst

tion and pressurisation of the sample at temperatures around 400°C (Danaie *et al.*, 2011). This is said to be a result of the exposure of metal surfaces due to breaking of the oxide layer caused by volume expansion upon hydrogenation. The need for activation may be removed by the addition of catalysts (Zaluski *et al.*, 1997).

The bulk of research on the combination of magnesium hydride with a range of catalysts lies in catalysts well-distributed throughout the particulates. The mechanisms by which these catalysts modify the reaction rates and mechanisms are not well understood (Berube *et al.*, 2007), but many systems and their benefits for hydrogen storage kinetics in magnesium hydride have been explored, including mixtures of magnesium with transition metals such as chromium (Bystrzycki *et al.*, 2005), cobalt (Hanada *et al.*, 2005), copper (Hanada *et al.*, 2005), iron (Montone *et al.*, 2012), manganese

(Liang *et al.*, 1999a), nickel (Liang *et al.*, 1999a), niobium (Huot *et al.*, 2002), palladium (Zaluska and Zaluski, 1999), titanium (Liang *et al.*, 1999a), vanadium (Liang *et al.*, 2000) and zirconium (Zaluska *et al.*, 2001). There have also been reports of systems using additives of other elements such as carbon (Amirkhiz *et al.*, 2009), and catalysis with intermetallics such as FeTi (Wang *et al.*, 2002), TiMn (Hu *et al.*, 2003), CrV (Kalisvaart *et al.*, 2012) and $PdFe_3$ (Von Zeppelin *et al.*, 2002).

Similarly, metal oxides have beneficial effects on the hydrogen storage kinetics of magnesium hydride allowing fast (< 1 h) hydrogenation and dehydrogenation at temperatures as low as 300°C (Dehouche *et al.*, 2002). As well as improving the hydrogen storage kinetics of magnesium hydride by providing pathways, depending on their oxidation state (Oelerich *et al.*, 2001), hard metal oxide catalysts enhance the ball milling process, creating defects in the hydride phase which provide further pathways for hydrogen diffusion (Jung *et al.*, 2006). Clearly, a whole range of materials of different elemental and relative composition have been produced and tested for their hydrogen storage kinetics and, given the equally broad range of conditions under which these materials have been tested, including temperatures between room temperature and over 400°C, and pressures between vacuum conditions and 200 bar, a comparison is very difficult as shown by Jain *et al.* (2010) who compiled a comprehensive table comparing the hydrogen storage kinetics and capacity of a range of materials which were all measured by different research groups and under different conditions. Using the activation energy of the dehydrogenation reaction, which can be established both from the reaction rate which will be discussed in section 5.7, and by using calorimetric data which

will be discussed in section 5.8, a comparison can be made. Table 2.1 compares a selection of different catalysed magnesium systems with as-received magnesium hydride, highlighting the improvements that can be made over as-received magnesium hydride using various transition metal catalysts.

Composition	Activation energy	Reference
MgH_2	120-156 kJ mol^{-1}	(Huot *et al.*, 1999)
MgH_2+5 at.% Ti	71.1 kJ mol^{-1}	(Liang *et al.*, 1999a)
MgH_2+5 at.% V	62.3 kJ mol^{-1}	(Liang *et al.*, 1999b)
MgH_2+5 at.% Mn	104.6 kJ mol^{-1}	(Liang *et al.*, 1999a)
MgH_2+5 at.% Fe	67.6 kJ mol^{-1}	(Liang *et al.*, 1999a)
MgH_2+5 at.% Ni	88.1 kJ mol^{-1}	(Liang *et al.*, 1999a)
MgH_2+1-5 at.% Nb*	51-78 kJ mol^{-1}	(Bazzanella *et al.*, 2011)

Table 2.1: A collection of activation energies reported for magnesium hydride and different transition metal catalysed magnesium hydride samples *thin film

Of great importance is the size and distribution of the catalyst throughout the magnesium matrix as the catalytic reaction is said to occur mainly at the interface between the catalyst and the magnesium(-hydride) (He *et al.*, 2010; Zaluska *et al.*, 2001). Small, well distributed (nano-)catalysts offer a large area of contact with the storage medium which is often achieved by a short, low-energy ball-milling process following the main, high-energy milling process (Berube *et al.*, 2007). Similarly, the amount of catalyst material must be kept to a minimum since it does not usually store any hydrogen at the operating conditions and they often consist of heavy transition metal elements, which reduces the hydrogen storage capacity.

Cycling Properties

One important hydrogen storage property of any hydrogen storage system is its cycling behaviour. Ideally, the hydrogen storage properties of any system would remain at their optimum for a large number of cycles, approaching 10,000 for a system that is used daily for a lifetime of 25 years. In reality, this is rarely the case for solid-state systems.

Improving the kinetics of the hydrogenation and dehydrogenation of magnesium hydride involving the processes discussed requires modification of the microstructure and composition of the materials used, and it has been shown that care must be taken to ensure the improved kinetics do not deteriorate during many cycles at elevated temperatures.

For example, there have been conflicting reports regarding the cycling stability of ball-milled nano-MgH_2. Whilst some authors warn of and report degradation of the nanostructure and the associated kinetic benefits (Berube *et al.*, 2007; Dal Toè *et al.*, 2004; Huhn *et al.*, 2005; Pelletier *et al.*, 2001), others claim that ball-milled nano-structures, including those of magnesium hydride, can be stable even at temperatures above the re-crystallisation temperature (Eckert *et al.*, 1993; Zaluska and Zaluski, 1999). One study shows a dramatic increase in the grain size of ball milled magnesium hydride, increasing from ca. 32-79 nm to ca. 279-284 nm, depending on the milling conditions, during the first dehydrogenation at 300°C (Paik *et al.*, 2010). Furthermore, there have been reports of an inverse relationship between the hydrogen storage capacity of magnesium hydride and milling time. Although this may well be a result of contamination with heavy transition metal ele-

ments such as iron and tungsten from the milling process (Huot *et al.*, 2013), this might also be caused by the increase in grain boundaries which might have a reduced hydrogen storage capacity (Hanada *et al.*, 2004). Since catalysed samples are often synthesised by ball-milling and are presented in a similar nano-crystalline form, their cycling behaviour is affected in a similar way and can also vary greatly between different samples.

Nickel and Magnesium Hydride

Small additions of well-dispersed nickel (< 2 at.%) to magnesium have been shown to result in favourable hydrogen storage kinetics as a result of surface catalysis (Holtz and Imam, 1999) but, given the right thermal conditions, nickel and magnesium can also interact chemically. Unlike the thermodynamic destabilisation promoted by elements such as silicon (Vajo *et al.*, 2004), where the reaction pathway $Mg + H_2 \rightleftharpoons^{\Delta H} MgH_2$ is changed to one of $AB_x + H_2 \rightleftharpoons^{\Delta H} AH_2 + xB$, nickel forms an A_2B alloy with magnesium that reversibly stores hydrogen in the reaction $Mg_2Ni + 2\,H_2 \rightleftharpoons^{\Delta H} Mg_2NiH_4$ with a reported dehydrogenation enthalpy of $\Delta H = 64.4\,kJ\,mol^{-1}\,H_2$ and an entropy of $\Delta S = 122.2\,J\,K^{-1}\,mol^{-1}\,H_2$ (Reilly and Wiswall, 1968) for the ternary hydride. This leads to a reduced equilibrium temperature T_{1bar} of 254°C.

Furthermore, Mg_2Ni has much faster hydrogenation and dehydrogenation kinetics compared with magnesium hydride, hydriding in ca. 15 min as opposed to > 1h at 350°C (Holtz and Imam, 1999), which can be further improved by mechanical grinding (Zaluska *et al.*, 2001). Since stoichiometric Mg_2NiH_4 has a theoretical hydrogen storage capacity of only 3.6 wt% due to

the 2:1 ratio of magnesium to nickel, efforts have been made to exploit the low-temperature kinetic benefits of the alloy in mixtures with magnesium hydride, whereby the kinetic properties of the ternary hydride are retained for the whole system, lowering the binary hydride's kinetic dehydrogenation temperature whilst providing a capacity proportional to the amount of Mg_2Ni added to the system (Berube *et al.*, 2007). Examples include hydride mixture capacities above 5 wt% (Zaluska *et al.*, 2001). Finally, the addition of transition metal catalysts to Mg_2Ni has been shown to further improve the hydrogen storage kinetics of the alloy (Bobet *et al.*, 2002; Zaluski *et al.*, 1995b), which raises the question of how a mixed system of MgH_2 and Mg_2NiH_4 would react to the addition of a transition metal catalyst.

2.2 Thin Films

Thin films offer an alternative route to creating hydrogen storage materials with potential for different properties compared to their bulk-counterparts. A whole range of magnesium-based thin films have been produced using different methods and additives in an attempt to improve the hydrogen storage properties of the hydride.

Thin film technology offers several advantages that can be exploited in order to improve the hydrogen storage properties of metal hydrides. Using thin film deposition techniques it is possible to control the microstructure of coatings as well as synthesising alloys, composites and nano-scale multilayers of metals at (near-)room temperature (Baldi and Dam, 2011; Ouyang *et al.*, 2006). Co-deposition techniques also allow the creation of metastable phases of materials that are normally immiscible, with a high level of homogeneity

(Baldi *et al.*, 2009b), and provide materials with a high surface area. Thin film techniques offer good control over process contamination, and protective coatings can be applied to prevent oxidation during transfer of samples in air (Jain *et al.*, 2010).

This section explores a range of thin film systems for hydrogen storage applications that can be found in the literature, focussing on those aiming to improve the hydrogen storage properties of magnesium hydride.

2.2.1 Thin Film Techniques

A number of ways of generating thin film coatings for hydrogen storage applications have been employed, including electron-beam evaporation (He *et al.*, 2010; Niessen and Notten, 2005), pulsed-laser deposition (Barcelo *et al.*, 2010; Patel *et al.*, 2008), arc vapour deposition (Blawert *et al.*, 2008), ion beam sputtering (Chen *et al.*, 2002) and magnetron-assisted physical vapour deposition (Baldi *et al.*, 2009a; Kalisvaart *et al.*, 2012).

One of the major benefits of vapour deposition processes is the high cooling rates of up to 10^6 K s^{-1} which can be achieved, allowing the formation of homogeneous solid solutions of materials that might have very different melting temperatures, without precipitation (Blawert *et al.*, 2008). For magnesium-based hydrogen storage applications this might enable better catalyst distribution.

Electron-Beam Physical Vapour Deposition

Electron-beam evaporation is a thermal evaporation process which employs a high-energy electron beam to vaporise materials, a schematic of which is

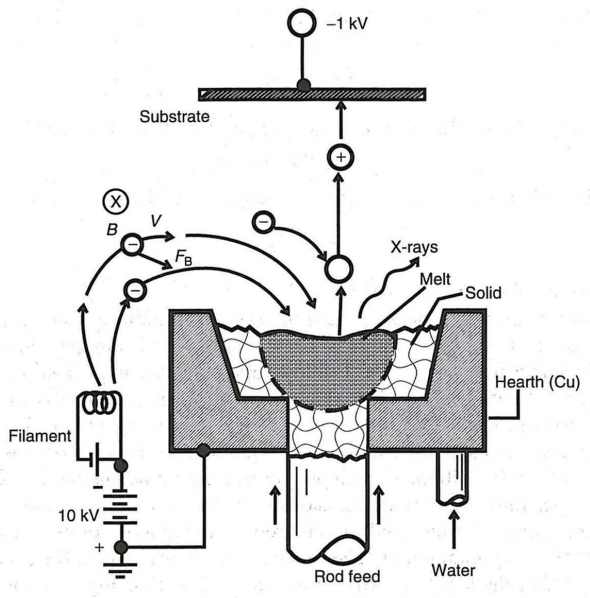

Figure 2.4: Schematic of a typical electron-beam coating process (Sree Harsha, 2005, chapt. 5)

shown in figure 2.4.

Situated in a high-vacuum environment of around 10^{-2} Pa, the beam, emitted from the cathode with a potential of between 4 and 20 kV, is controlled by an electro-magnetic field, re-directing it onto the target material which acts as an anode, where some of the kinetic energy the electrons carry is converted into thermal energy, melting and vaporising the target material. The vapour forms a coating on the substrate that is placed in front of the vapour source with typical deposition rates of around 100 Å s^{-1} for magnesium (Ohring, 2002; Sree Harsha, 2005).

Arc Vapour Deposition

A thermal evaporation process similar to electron-beam vapour deposition, cathodic arc vapour deposition relies on a high-current, low voltage arc that

is struck between a cathodic target material and an anode under vacuum, resulting in a highly energetic region known as the *cathode spot*, which results in vaporisation of the cathode material with a high degree of ionisation (> 85% of the vaporised material), which can be exploited by the use of a negative bias on the substrate, which results in dense coatings even at non-normal angles. The cathode spots will move randomly between different locations on the cathode unless they are controlled by an electromagnetic system, resulting in more even erosion of the target material. Compound targets can be used and the stoichiometry is generally retained whilst anode erosion and vaporisation can be minimised by the choice of a high-melting temperature anode material in combination with sufficient anode cooling (Sanders and Anders, 2000; Sree Harsha, 2005).

Pulsed-Laser Deposition

A further thermal evaporation process, pulsed-laser deposition forms coatings by vaporising materials under high-vacuum. Pulses of high-powered laser beams are focussed onto the target material, causing electronic excitation and ablation of the target material into a directional plume of target material that forms a coating on a substrate placed in its path (Ohring, 2002, chapt. 3). The composition of the plume and the deposited coating is generally the same as that of the target material, which allows deposition of composite materials.

Ion Beam Sputtering

Sputtering is the process of momentum exchange between particles (Penning and Moubis, 1940), resulting in a release of particles from the target material

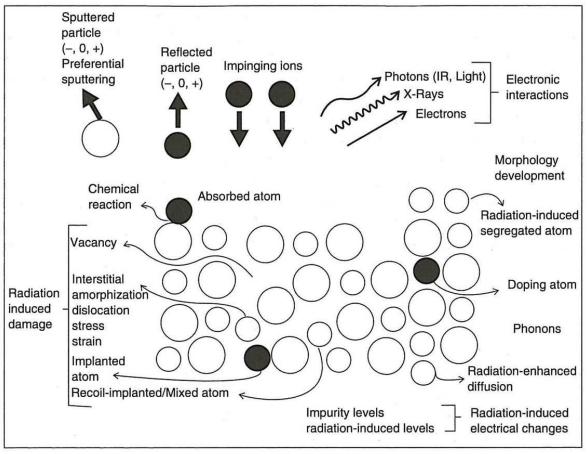

Figure 2.5: Schematic of the effect of an impact by high-energy particles (Sree Harsha, 2005, chapt. 7)

(Wehner, 1955), mostly in the form of neutral atoms (Urbassek and Hofer, 1993). When an energetic ion impacts a surface it may be reflected back, adsorb onto the surface, scatter, eject and sputter surface atoms, or become implanted in the target material, depending on the energy of the ion (Ohring, 2002, chapt. 4). Figure 2.5 shows a schematic of the different interactions that might occur upon impact of a high energy particle on a sputtering target. When an energetic ion is accelerated towards the cathode target, the kinetic particle can cause the emission of light, X-rays and secondary electrons in electronic collisions with the target. Nuclear collisions between the impacting particles and the sputtering target result in atoms being ejected (sputtered) from the cathode whilst the ions are either reflected or become implanted in the target material (Sree Harsha, 2005, chapt. 7).

In the case of ion beam sputtering it is an external ion beam that provides a source of ions which are accelerated onto the surface of the target material in a vacuum environment. This ion flux is charge-neutralised, which allows

sputtering of non-conductive materials, and the flux, incident angle and energy of the ions are independent of one another, which allows a high degree of control over the process conditions. The flux of sputtered target material has an energy of typically one order of magnitude higher than evaporation processes, which results in coatings with better adhesion to the substrate and higher density (Sree Harsha, 2005, chapt. 7).

Magnetron-Assisted Physical Vapour Deposition

Magnetron-assisted physical vapour deposition, also known as *magnetron sputtering*, is a sputtering process that does not rely on an external ion-source but creates and interacts with a plasma. Figure 2.6 shows a schematic of a magnetron sputtering process showing the main hardware elements as well as a schematic of the interaction between the plasma and the sputtering process.

Plasma is the 4^{th} aggregate state of matter, describing a weakly ionised gas consisting of atoms as well as equal numbers of positively charged ions and electrons, resulting in an electrically neutral but conductive phase (Sree Harsha, 2005, chapt. 3). In magnetron sputtering an inert gas, e.g. argon, is injected into a vacuum chamber at pressures around 10^{-3} mbar. The magnetron, which is a water-cooled device supporting the target material that contains an arrangement of magnets employed to generate a magnetic field in front of the target material, acts as a high-voltage cathode (typically in the range of 100s of volts).

In a DC plasma, stray electrons near the cathode are accelerated towards the anode and ionise gas atoms in their paths, releasing two electrons in the

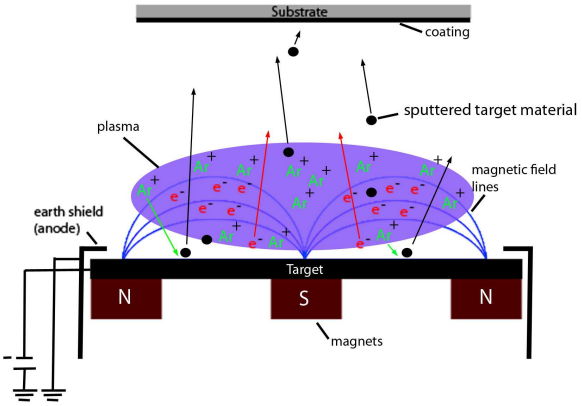

Figure 2.6: Schematic of a simple magnetron sputtering set-up

process. These are accelerated and, in a cascading effect, cause further ionisation which releases further electrons and so on. Meanwhile the ions are accelerated towards the cathode where, in a sputtering process as described in section 2.2.1, electrons are released which set-off a new cascade of ionisation. This process, known as *Townsend discharge*, governs the formation of a plasma (Ohring, 2002, chapt. 4).

Figure 2.7 shows the structure of a DC plasma. In the highly active area near the cathode, the very thin *Aston dark space* contains low energy electrons being accelerated away from the cathode, and high energy ions about to collide with the cathode. Moving away from the cathode, the *cathode glow* area is thought to emit light via the de-excitation of positive ions through neutralisation. The *cathode dark space*, also known as *Crookes dark space*, provides most of the drop in potential between the cathode and the neutral

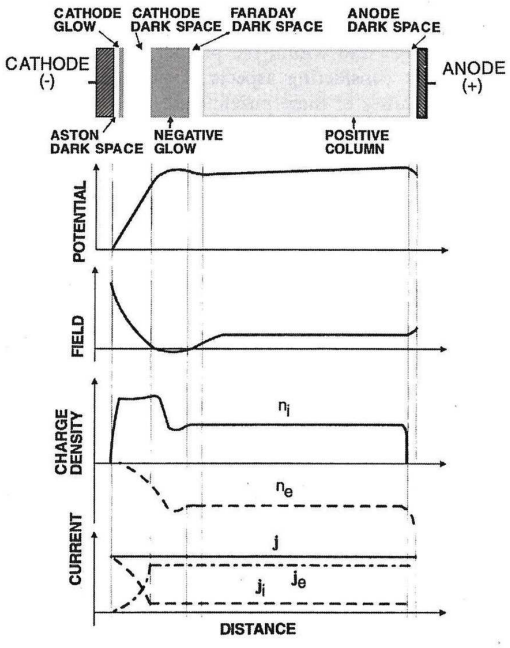

Figure 2.7: Schematic of a DC plasma (Ohring, 2002, chapt. 4)

plasma. This region sees the acceleration of electrons emitted from the cathode which causes the formation of plasma, and the acceleration of ions from the plasma in the opposite direction. The *negative glow* region is caused by photon emission as a result of gas ionisation caused by the collision of high-energy electrons with the gas. The *Faraday dark space* and *positive column* are not normally seen as the substrate is placed inside the *negative glow* (Ohring, 2002, chapt. 4).

The introduction into the system of a magnetic field from an arrangement of magnets, as found e.g. in a planar magnetron, results in the creation of an $E \times B$ field. These are usually arranged in such a way that the magnetic field lines run parallel to the surface of the cathode, resulting in the emitted electrons, entering the magnetic field perpendicular to the magnetic field

lines, being deflected into a cycloidal path, constraining them to a small area in front of the target.

The electrons are effectively trapped in this small region in front of the target known as the *race track* where the gas ionisation is increased, leading to a very intense plasma. This then results in a series of interconnected benefits for the sputtering process. The increased ionisation increases the ion bombardment of the target, resulting in a higher sputtering rate which in turn leads to more ionisation due to higher emission of secondary electrons, ultimately leading to a higher deposition rate at reduced voltages (Kelly and Arnell, 2000). Similarly, due to the higher ionisation efficiency, the process can operate at pressures one order of magnitude lower than a conventional DC plasma, which results in reduced collisions of the sputtered flux with the gas phase, leading to a more directional, less scattered flux producing denser coatings with a faster deposition rate, further increasing the efficiency of the system by concentrating the flux in a smaller area (Kelly and Arnell, 2000; Ohring, 2002, chapt. 5).

The techniques have all shown to provide useful means for generating novel hydrogen storage materials and some might have certain financial and technological advantages such as the ease of co-sputtering from multiple targets and/or composite targets, but there has to date not been a direct comparison assessing the direct benefit of one coating technique over another on the hydrogen storage properties of a coating.

2.2.2 Magnesium Coatings

The structure and hydrogen storage behaviour of thin film coatings has been the subject of many reports in the literature. In an attempt to understand the hydrogenation behaviour of pure magnesium thin films Léon *et al.* (2002) identify the effect of sample geometry, particle size, oxygen content, material preparation and particle morphology on the (de-)hydrogenation behaviour of magnesium hydride, discussed in section 2.1.2, as the reason that no general mechanism has been proposed for the reaction between magnesium and hydrogen. This highlights the complexity of the topic even before addition of catalysts and alloying elements to the magnesium-hydrogen system.

The structure of magnesium coatings is generally one with a high level of grain orientation and is highly dependent on the process conditions employed during deposition (Blawert *et al.*, 2008; Léon *et al.*, 2002). Störmer *et al.* (2007) discuss the effect that the gas pressure and deposition angle have on the corrosion properties of pure magnesium thin films. The coatings, produced by magnetron sputtering, all exhibit a strong crystal orientation with the <001> direction coinciding with the axis of growth, which is characteristic of magnesium coatings (Blawert *et al.*, 2008; Higuchi *et al.*, 2002; Qu *et al.*, 2010a). The paper exposes a strong relationship between the deposition pressure and angle, and the surface roughness, density, and corrosion rate of magnesium coatings. In addition, Blawert *et al.* (2008) study the effect different coating techniques including magnetron sputtering, ion beam sputtering and vacuum arc deposition have on the structure and corrosion resistance of pure magnesium coatings, concluding that there is no relationship

between the latter and the deposition technique employed.

It has been shown that different magnesium microstructures created using thin film techniques can promote different hydrogen storage properties. He *et al.* (2010) produced a series of highly oriented magnesium "nanoblades" by glancing angle deposition, some of which were coated with, and some of which were co-deposited with 4.6 at.% vanadium. A relationship between the size of vanadium clusters that formed upon hydrogen cycling and the angle of deposition of the coating was found, and it was concluded that a high angle of deposition results in fast kinetics with activation energies improving from $69.4 \pm 0.6\,\mathrm{kJ\,mol^{-1}}$ to $35.3 \pm 0.9\,\mathrm{kJ\,mol^{-1}}$ due to increased levels of porosity and improved contact between the magnesium and vanadium catalyst phases.

A number of reports exist that study the hydrogen storage behaviour of pure magnesium coatings. Akyildiz *et al.* (2006) studied the hydrogenation behaviour of a pure magnesium thin film with a thickness of 420 nm, produced by thermal evaporation, which did not fully hydrogenate in 6 hours at 400°C. The authors also noticed a significant amount of grain growth due to the elevated temperatures the thin film was subjected to. In contrast, Léon *et al.* (2002) manage to fully hydrogenate an air-exposed 30 μm coating of pure magnesium, similarly prepared by thermal evaporation, at 350°C in less than 17 h, absorbing the first 6 wt% in 400 min. The second cycle of hydrogenation took place at a much faster rate, absorbing the first 6 wt% in only 200 min, which is explained by defects introduced into the structure during the first cycle facilitating hydrogen penetration in the second. The authors show that the microstructure of the magnesium coating is not restored after dehydrogenation, transforming the highly oriented coating to a crystalline

structure with random grain orientation. The grain size however increases only slightly within the experimental error (not quantified) from 54 to 60 nm during the two cycles.

The air-exposed sample discussed by Léon *et al.* (2002) highlights that small amounts of oxide contamination are not necessarily detrimental to the hydrogen storage properties of magnesium hydride, as discussed in section 2.1.2. Studies on the effect of magnesium oxide on the hydrogen storage properties of magnesium thin films have shown that small amounts of nanocrystalline magnesium oxide, inserted between a magnesium coating and a palladium surface catalyst, can in fact improve the hydrogen storage kinetics by providing nucleation sites for hydride growth in an Mg-MgO-Pd thin film structure (Hjort *et al.*, 1996). Increased levels of oxygen in the interface region between the magnesium and palladium layers in this thin film structure however were shown to present a diffusion barrier, slowing the hydrogenation kinetics. Ingason and Olafsson (2006) observe similar properties for a magnesium thin film deposited by sputtering under argon for 30 minutes with varying amounts of oxygen contamination in three two-minute intervals. Again, an initial improvement in reaction kinetics is measured with increasing oxygen:argon ratios of 0, 0.32:40 and 0.56:40, followed by slowing kinetics at a ratio of 0.64:40. Improved hydrogen storage kinetics are explained in this case by oxide crystallites dispersed in the magnesium film providing diffusion pathways for hydrogen. Similarly, oxide crystallites may well act as nucleation sites for hydride growth.

2.2.3 The Mg/Pd System

Much research has been done on magnesium/palladium coatings. In fact most thin films systems to date include a capping layer of palladium in order to prevent oxygen contamination of the underlying thin film during transfer of the sample from the vacuum deposition system to the material characterisation machinery, and to promote dissociation of hydrogen in a surface catalyst role (Siviero *et al.*, 2009; Yamamoto *et al.*, 2002).

It has been shown that magnesium coatings, capped with, or sandwiched between layers of palladium will reversibly hydrogenate at room temperature (Higuchi *et al.*, 1999, 2002; Yoshimura *et al.*, 2004). The hydrogen storage behaviour of these thin films is affected both by the sputtering conditions (Higuchi *et al.*, 1999), where a lower degree of crystallisation reduces the dehydrogenation temperature of palladium-capped magnesium coatings, and the thickness of the magnesium layer (Higuchi *et al.*, 2002). An increase in thickness from 25 nm to 800 nm of a magnesium coating sandwiched between two 50 nm layers of palladium was shown to result in a decrease in dehydrogenation temperature of over 100°C.

The optical reflectance of thin, magnesium-based films changes depending on the state of hydrogenation and this is used in *hydrogenography* where the hydrogenation and dehydrogenation behaviour of such coatings is assessed by means of measuring the change in reflectance and transmission of light where a hydrogenated film transmits light as opposed to a metallic film which reflects it (Dam *et al.*, 2007). Yoshimura *et al.* (2004) show that the transformation from a metallic film to a hydrogenated one can occur at room

temperature in less than 4 seconds, which is useful for sensor devices that require optical switching.

The effect of palladium on the hydrogen storage behaviour of magnesium thin films has been explained by an elastic constraint process whereby, as the hydrogenated film is heated, the hydrided palladium layer releases hydrogen and applies a compressive stress on the magnesium hydride layer beneath it, making it unstable and causing it to release hydrogen at temperatures as low as 87°C (Higuchi *et al.*, 2002). Baldi *et al.* (2009a) take this further, showing that alloy formation by the magnesium and palladium layers at the interfaces between the two causes this compressive stress in the magnesium layer, effectively destabilising the thermodynamics and increasing the plateau pressure of the dehydrogenation reaction. They show that a decreased magnesium layer thickness results in an increased plateau pressure at the same temperature and thus an increased level of destabilisation which is contrary to the results presented by Higuchi *et al.* (2002). Crucially however, Higuchi *et al.* (2002) produce films an order of magnitude thicker than those presented by Baldi *et al.* (2009a) and their explanation for the effect of thickness on dehydrogenation behaviour lies in the levels of anisotropic deformation of thinner, more oriented films, resulting in lower levels of hydrogen-induced expansion in the stress direction.

Despite the promising hydrogen storage properties of these thin films of magnesium and palladium, especially for switchable mirror applications, there are two major drawbacks. The cost of palladium is prohibitively high at $ 500-900 kg^{-1} between 2010 and 2013 (Infomine, 2013b), which means up-scaling such materials would make little economic sense. From a techno-

logical point of view it has been shown that the alloy formation between the magnesium and palladium phase is not restricted to the interface region but will continue to grow an Mg_6Pd phase which results in poor cycling behaviour with a large loss of capacity (Siviero *et al.*, 2009).

In an attempt to further develop and improve these thin film composites, a range of different magnesium-based thin film systems have been developed. This includes similar layered structures as well as composite structures.

2.2.4 Next Generation Switchable Mirror Systems

Several alternative magnesium-based switchable mirror systems have been shown to promote fast hydrogenation and dehydrogenation kinetics at low temperatures, including multilayers of magnesium and titanium (Baldi *et al.*, 2010; Tajima *et al.*, 2009), and alloys of magnesium/manganese (Richardson *et al.*, 2001), magnesium/iron (Richardson *et al.*, 2001), magnesium/cobalt (Richardson *et al.*, 2002), magnesium/nickel (Richardson *et al.*, 2001) and magnesium/chromium/vanadium (Kalisvaart *et al.*, 2012).

The magnesium/nickel system has seen a great deal of attention, due to alloy formation of magnesium and nickel, and the formation of the ternary Mg_2NiH_4, as discussed in section 2.1.2. Much like magnesium/palladium thin films, palladium-capped magnesium/nickel coatings can readily hydrogenate and dehydrogenate at room temperature and, much like magnesium/palladium coatings, degradation of the switching process is observed, albeit after more than 100 cycles (Bao *et al.*, 2006).

Inserting a thin layer of a metal immiscible in both magnesium and palladium has been shown to prevent Mg_6Pd alloy formation, thus improving the

cycling behaviour of the thin film and retaining the surface catalyst activity of the palladium cap. Baldi *et al.* (2009c) show that depositing a 2 nm layer of titanium between a magnesium coating and a palladium cap reduces the plateau pressure of the thin film at a given temperature with respect to a magnesium/palladium thin film without the titanium 'buffer'. This results in faster kinetics and better cycling stability of the switchable mirror coating over 4 cycles at 60°C. Similarly, Bao *et al.* (2006) show that a 2 nm titanium layer in-between their magnesium/nickel alloy with a thickness of 40 nm and its palladium cap of 6 nm thickness increases the cycling stability of their switchable mirror well beyond 400 cycles. This confirms the Mg_6Pd alloy formation is responsible for the poor cycling properties seen in magnesium-palladium thin film composites as well as the change in the thermodynamics of the interaction between the thin films and hydrogen.

Fritzsche *et al.* (2009) show that the insertion of 5 nm of tantalum between a magnesium-aluminium thin film produced by magnetron sputtering and a palladium cap can effectively prevent magnesium-palladium alloy formation. In contrast, the insertion of 7.5 nm of tantalum between a magnesium-chromium-vanadium thin film and a palladium cap, similarly deposited by magnetron sputtering, was shown to degrade due to magnesium-palladium alloy formation despite this tantalum interlayer (Zahiri *et al.*, 2012). Tan *et al.* (2009) studied the cycling behaviour of magnesium coatings with a palladium capping layer separated by a layer of different transition metals. Whilst, under the same conditions, some of the films' hydrogen storage properties degrade rapidly due to Mg_6Pd alloy formation (those with an iron interlayer or with no interlayer at all), others (including interlayers

of titanium and niobium) do not. The authors explain that this is caused by the different enthalpies of hydride formation of the metals, causing the niobium and titanium coatings to form and remain as hydrides during cycling experiments whilst the palladium and iron coatings remain metallic during cycling at 250°C. The metallic coatings allow rapid inter-diffusion resulting in the formation of Mg_6Pd and the resulting degradation of of the hydrogen storage properties of the thin films. Tantalum on the other hand, with an enthalpy of hydride formation of ΔH_f = -76 kJ mol^{-1} H_2, will hydrogenate and dehydrogenate under very similar conditions to magnesium (ΔH_f = -72.9 kJ mol^{-1} H_2) (Tan *et al.*, 2009), which is a likely explanation for why different results have been reported for the suitability of tantalum as a diffusion barrier for Mg_6Pd alloy formation.

2.2.5 Micron-Scale Coatings

Nano-scale thin films have favourable properties that make them valuable candidates for sensor applications. For hydrogen storage applications however, taking into account the substrate, the ratio of thin film to substrate must be increased. This can be achieved by delaminating micron-thick thin films from their substrate, resulting in free-standing thin films. The hydrogen storage properties of the gram quantities achievable using these thin films can then be tested using volumetric and gravimetric methods, comparable with those used for powder-based storage materials.

A range of micron-scale, magnesium-based coatings have been explored including multilayers of magnesium/nickel/palladium (1.7 μm thick and weighing 169 mg) (Ouyang *et al.*, 2006), magnesium/palladium (ca. 18 μm thick

and weighing 220 mg) (Ye *et al.*, 2010) and magnesium/iron/titanium (1.5 μm thick and weighing 10-15 mg) (Kalisvaart *et al.*, 2011), magnesium coatings with a thin surface catalyst (1.5 μm thick, weight not published) (Tan *et al.*, 2009) and magnesium coatings co-deposited with small amounts of transition metals such as nickel (0.6 μm thick, weight not published) (Chen *et al.*, 2002), iron (0.6 μm thick, weight not published) (Tan *et al.*, 2011) and mixtures of transition metals such as chromium with vanadium (1.5 μm thick, weight not published) (Zahiri *et al.*, 2012) and iron with chromium (1.5 μm thick, weight not published) (Fritzsche *et al.*, 2012). Unlike the nano-scale thin films which are only limited by the thermodynamics of the interaction between hydrogen and magnesium, these thicker coatings all require higher hydrogenation and dehydrogenation temperatures, due to kinetic constraints.

2.2.6 Multilayer and Co-Deposited Coatings

It has been established that both the grain size of the magnesium phase and the size and distribution of a catalyst phase has a large impact on the hydrogen storage kinetics of magnesium-based hydrogen storage materials. Nano-dispersion of transition metal catalysts in magnesium thin films can be achieved by co-depositing magnesium and the desired catalyst, or by depositing the film in alternating layers of magnesium and the desired catalyst in a multilayer structure. The latter allows tight control over the resulting microstructure as well as the overall composition of the thin film. It is also possible that, unlike with homogeneous, co-deposited thin films, depending on the materials used, the layer interfaces between the magnesium and catalyst layers might act as diffusion pathways, providing fast hydrogenation and dehydrogenation kinetics.

Furthermore, multilayering might constrain the grain size by keeping the magnesium in separated layers so grain growth in the bulk cannot occur. Kalisvaart *et al.* (2011) show, for a multilayer coating with alternating layers of magnesium and an iron-titanium composite, that a crystalline, or even amorphous layer of the transition metal composite can remain in-tact after hydrogen cycling at up to 300°C, and preserve the kinetic benefits of nanostructured materials.

The low content of catalytic material needed in order to retain a high hydrogen storage capacity restricts the thickness ratio of magnesium and catalyst layers in a multilayer structure, resulting in either thick magnesium layers or extremely thin catalyst material layers. This restricts the level of

catalyst distribution within the thin film structure which can be improved by co-deposition. The thickness of magnesium layers in multilayers has been shown to have a considerable impact on the kinetics and cycling stability of multilayer coatings whereby thinner magnesium layers have shown to be beneficial (Kalisvaart *et al.*, 2011).

In magnesium co-deposited with transition metal catalysts, the homogeneous distribution of the catalyst material is quickly lost to the formation of precipitates in the structure. It has been shown that segregation of magnesium and transition metal phases occurs after only one cycle of hydrogenation and dehydrogenation for a magnesium coating co-deposited with a chromium-vanadium mixture (Kalisvaart *et al.*, 2012). Baldi *et al.* (2009b) show a cluster-like structure in their co-deposited magnesium-titanium composite thin film, and although this means that the perfect homogeneous distribution of a catalyst material in a magnesium matrix created by co-deposition is rapidly lost, advantages over multilayer structures have been shown. Kalisvaart *et al.* (2011) compare their magnesium/iron-titanium multilayer structure to a co-sputtered sample of similar composition which exhibits a higher cycling stability both in terms of hydrogen storage properties and grain size. This is explained by iron-titanium precipitates forming, which, provided they are sufficiently small, help prevent the grain growth of the magnesium phase. The suggested mechanism is pinning which relies on the intersection of grain boundaries with suitably small particles. This results in a reduction of grain boundary energy which needs to be overcome, thus 'pinning' the grain size (Gladman, 1966).

2.2.7 Summary

Having established the scope of the hydrogen storage dilemma, the range of options for improvement, and the potential benefits of using thin film technology to develop novel, improved magnesium-based hydrogen storage materials, several options for further research and development arise.

It has been established that alloy formation in thin films can have a detrimental effect on the cycling stability of magnesium/palladium composites. It has also been shown however, that alloy formation of magnesium with certain other elements, such as nickel, can have potential advantages such as faster kinetics at lower temperature. Furthermore, it has been established that a fine distribution of metal or metal oxide catalysts within a magnesium matrix can promote very fast hydrogenation and dehydrogenation kinetics at reduced temperatures compared with pure magnesium hydride. Finally, a reduced grain size and increased diffusion pathways have proven to be beneficial for the hydrogen storage kinetics of magnesium hydride, which can be promoted by nanostructuring magnesium-based thin films in multilayers.

The effect of single catalyst materials in multilayers with magnesium has not been widely studied, certainly not with respect to gravimetric and volumetric hydrogen storage measurements in micron-thick coatings. Research on a magnesium/iron-titanium multilayer has shown some promising results, but the lower limits of the magnesium layer thickness might be further expanded. Furthermore, it has been shown that the multilayer structure is held together at temperatures below the recrystallisation temperature of the catalyst interlayer (Kalisvaart *et al.*, 2011), which severely restricts the types

of catalyst materials that can be used. The effect of recrystallisation of an immiscible transition metal interlayer has not yet been shown in magnesium/transition metal coatings.

The following chapter explains the equipment and processes used for thin film processing, microstructural testing and analysis of the hydrogen storage properties of the thin films that are presented in chapter 4. In order to meet the objectives outlined in section 1.3 these coatings explore the effect of pure vanadium and chromium catalyst layers on the hydrogen storage properties of thick, magnesium-based multilayer coatings. Similarly, the effect of recrystallisation of amorphous interlayers on the hydrogen storage properties and the corresponding structural evolution of these thin film structures is studied and a transition-metal catalysed, magnesium-rich magnesium/nickel alloy thin film multilayer is produced in order to study the effect of transition metal catalysts on magnesium/nickel thin films. A non-catalysed magnesium control sample is produced in order to identify any effects of the coating process on the hydrogen storage behaviour of these novel thin film materials.

Chapter 3

Experimental Methods

3.1 Introduction

Magnesium-based, transition metal catalysed thin films were fabricated by magnetron sputtering and then characterised both in terms of their microstructural evolution and their hydrogen storage properties.

This chapter details the processes involved in making the thin film multilayer samples and preparing them for structural- and hydrogen storage testing, and the characterisation methods employed.

3.2 Magnetron-Assisted Physical Vapour Deposition

A Teer Coatings UDP 650 closed field unbalanced magnetron-assisted physical vapour deposition (PVD) system, based on an argon plasma, was used to produce a range of different thin film multilayer coatings, consisting of layers of magnesium, separated by layers of different transition metal catalysts, and capped on both surfaces with a thin layer of palladium to prevent oxidation of the thin film and interaction with the substrate.

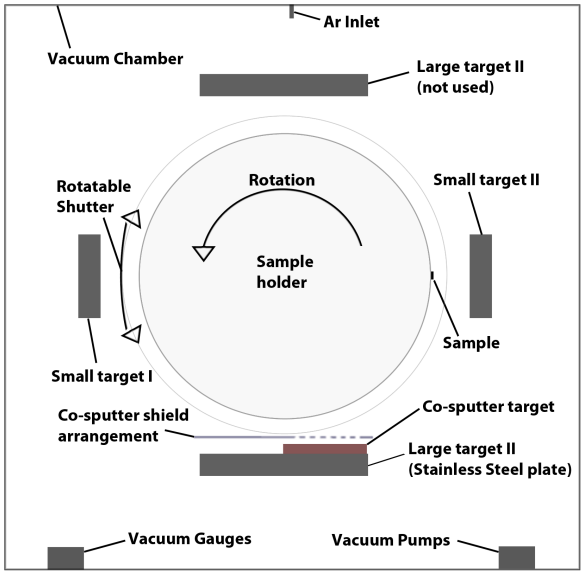

(a)

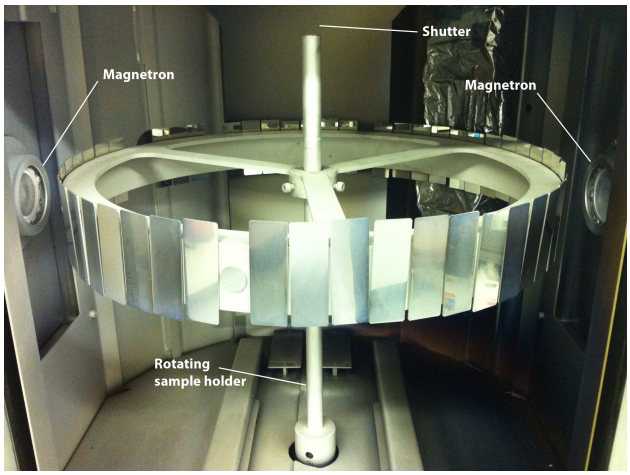

(b)

Figure 3.1: a) Top view schematic showing the 4-magnetron PVD system set-up around a central rotating sample stage and b) a photograph showing coated samples mounted on the sample holder post-deposition

The coating system, schematically depicted in figure 3.1a, was equipped with two opposing circular magnetrons (small target I + II), holding sputtering targets of 57 mm diameter. The other two opposing, planar magnetrons

(large target I + II) were of 175 by 380 mm dimension. Only one of these was employed during the coating processes (large target I) whilst the other (large target II) was covered with aluminium foil in order to prevent contamination of the underlying target. These magnetrons were arranged around a circular sample stage which could be rotated around a central axis inside the vacuum chamber and a single shutter would rotate around the same axis, both of which can be seen in figure 3.1b. Multilayer coatings were thus generated by rotating the sample holder, passing the substrates through the sputter flux of each of the magnetrons in turn.

This work discusses the structural evolution and hydrogen storage properties of 4 magnesium-based coatings, produced using this set-up. A range of different target materials were used in generating these coatings, tabulated in table 3.1.

Material	Dimensions	Purity	Source
Magnesium	3 mm × 57 mm dia.	99.95%	Testbourne
Nickel	3 mm × 57 mm dia.	99.95%	Goodfellow
Chromium	1 mm × 57 mm dia.	99.95%	Testbourne
Vanadium	1 mm × 57 mm dia.	99.95%	Testbourne
Palladium	3 mm × 57 mm dia.	99.99%	B'ham Metal
Stainless Steel (316L)	175 × 380 mm	N.A.	Unicorn Metals

Table 3.1: Table showing the size, purity and source of the different sputtering targets used in making the thin films presented in this work

3.2.1 Coating Conditions

A range of multilayer thin films consisting of 150 layers of magnesium, separated by thin layers of transition metal catalysts, were produced using this set-up. All samples were capped with a thin layer of palladium using the

coating conditions detailed in table 3.2 to prevent oxidation during sample transfer from the PVD vacuum chamber and the delamination process. After reaching a vacuum of 1×10^{-5} mTorr, each target was sputter-etched for 10 minutes at the final operating conditions shown in table 3.1 behind the shutter in order to remove any oxide layer generated during loading of the samples. A nickel-rich transition metal mixture (TM) was produced by co-sputtering nickel from the stainless steel 316L target (SS). The nickel target was mounted in a circular recess on the face of the stainless steel target, located in-line with the sample holder and centrally on the race track area of the target. As shown in figure 3.1a, a steel co-sputter shield arrangement was fixed in front of the entire target leaving only a circular window directly in front of the nickel target for the sputter flux to escape, in order to increase the ratio of nickel to stainless steel in the sputter flux. This nickel-rich transition metal mix separated the magnesium layers in the Mg/TM sample.

The magnesium multilayers and the palladium capping layers were deposited from each of the circular magnetrons neighbouring the stainless steel planar target. The multilayering was achieved by mounting the substrates on the circular sample holder, ca. 0.5 m in diameter, inside the PVD chamber, which was then set to rotate at 1 RPM for the duration of the process, creating layers of material as the substrates passed through the sputter flux of the magnetrons. During the deposition of the Mg/TM multilayer, the shutter was placed in front of the palladium target in order to prevent contamination by the sputter flux from the magnesium and TM targets. The palladium capping layer was deposited in two rotations using the conditions listed in table 3.2.

For the Mg/Cr and Mg/V samples that are discussed in this work, 150 magnesium layers were separated by thin layers of chromium and vanadium. In these cases the magnesium layers and the interlayers of chromium and vanadium were deposited using the two opposing circular magnetrons with a magnesium target mounted on one and a chromium or vanadium target mounted on the other. The Mg/TM, Mg/Cr and Mg/V samples were all given two coatings of their respective transition metal(-mix) between the top and bottom magnesium layer and the palladium cap in an attempt to prevent the formation of a magnesium-palladium alloy as discussed in section 2.2.3. A magnesium control sample ($Mg_{control}$) sample was produced using the same set-up; however, the transition metal targets were not employed, leading to 150 layers of magnesium being deposited without separating layers of a transition metal.

The palladium capping layers deposited on both surfaces of the Mg/Cr, Mg/V and $Mg_{control}$ samples were co-deposited in 5 revolutions from the stainless steel target using the arrangement employed in generating the nickel-rich transition metal mix. This was necessary due to the set-up of the PVD coating system. During sputter deposition of the multilayers, the shutter was kept in front of the palladium target in order to prevent contamination.

Tables 3.2a to 3.2d list the sputtering conditions employed during the deposition of the 4 samples, including the argon pressure and current on each of the magnetrons. These conditions resulted form a series of preliminary multilayer coatings consisting of 150 bi-layers of magnesium and titanium, using the same physical set-up that was employed for the Mg/Cr, Mg/V and $Mg_{control}$ sample.

Mg/TM

Target	Current	Ar Pressure
Magnesium	0.3 A	1.7 mTorr
Nickel (SS)	1 A	
Palladium	0.2 A	

(a)

Mg/Cr

Target	Current	Ar Pressure
Magnesium	0.35 A	1.7 mTorr
Chromium	0.04 A	
Palladium*	1 A	

(b)

Mg/V

Target	Current	Ar Pressure
Magnesium	0.3 A	1.7 mTorr
Vanadium	0.07 A	
Palladium*	1 A	

(c)

$Mg_{control}$

Target	Current	Ar Pressure
Magnesium	0.3 A	1.7 mTorr
Palladium*	1 A	

(d)

Table 3.2: Tables showing the sputtering conditions used during deposition of a) the Mg/TM sample, b) the Mg/Cr sample, c) the Mg/V sample and d) the $Mg_{control}$ sample. *co-sputtered from a stainless steel target

Table 3.3 lists the coating conditions that were employed for the Mg/Ti multilayer sample that was deposited onto a glass cover slip. The peak broadening of the Mg(002), Mg(004), Ti(002) and Ti(004) reflections in an XRD diffractogram that was produced was used to estimate the crystallite size of the magnesium and titanium phases at 13 $\pm$ 2 nm and 6 $\pm$ 1 nm respectively, as detailed in section 3.3. From SEM measurements of the cross-section of the coating, a coating thickness of 3 $\pm$ 0.1 μm was established, which allows ca. 20 $\pm$ 1 nm per layer, confirming the thickness of the magnesium/titanium bi-layers. This information was then used to derive the relative sputter rate of magnesium and titanium, for the given power settings, and to estimate the required target current for chromium, vanadium and palladium, given the relative sputter rates which were taken from the Gencoa Sputter Rate

Calculator (Gencoa Ltd., 2013).

Target	Current	Ar Pressure
Magnesium	0.27 A	1.7 mTorr
Titanium	0.45 A	

Table 3.3: Table showing the PVD system settings employed for the deposition of the magnesium/titanium calibration multilayer sample

The sputter yield for the co-sputter arrangement was calculated using the relative sputter yield of palladium, nickel and titanium of 3.1:1.6:1, given the known sputter rate of titanium from the small targets. The race track area of the small and large targets was measured at 1810 mm^2 and 16650 mm^2 respectively which was then used to calculate the current required to achieve the same current density calculated for the small target (2.5×10^{-4} A mm^{-2}).

3.2.2 Sample Preparation

The coatings were all deposited onto 2.5 × 7.6 cm glass microscope slides, which were coated with a layer of nitrocellulose to allow delamination. The nitrocellulose layer was produced by diluting nail varnish in acetone in a 1:5 ratio, and the solution was applied to the slides using a pipette. It was allowed to dry fully in air for 24 hours prior to the application of the PVD coating. For each sample a number of 19 mm diameter glass cover slips were also placed on the rotary sample holder to allow characterisation of the thin film by XRD, SEM and TEM.

After deposition of the magnesium-based thin films, the samples were submerged in acetone and subjected to up to 1 hour of ultrasound treatment

in a Camlab Transsonic TP690 Ultrasound bath to aid the dissolution of the nitrocellulose layer separating the coating form the glass substrate, resulting in the delamination of the thin film coatings from the substrate. The samples were then carefully rinsed in acetone up to 5 times, resulting in thin film flakes. Due to the high specific surface area of these flakes, they were placed into glass vials whilst still somewhat wet from the acetone treatment. The remaining acetone was then evaporated at 0.5 bar and the samples were placed and stored in an MBRAUN Unilab argon (purity 99.9999%) glove box ($O_2 < 0.1$ ppm, $H_2O < 0.1$ ppm).

3.3 Structural Characterisation Techniques

3.3.1 X-Ray Diffraction

The microstructure of the thin films was assessed both before and after hydrogen cycling using X-ray diffraction. The technique relies on the interaction between X-rays and crystallites changing the X-ray signal via constructive and destructive interference. The geometry of the interaction is linked to the geometry of the crystal structure via *Bragg's* law

$$n\lambda = 2d\sin\theta \tag{3.1}$$

where n is the order of diffraction, λ represents the wavelength of the X-ray signal, d is the distance between planes of atoms in a crystallite and θ is the angle between the line of the incident X-ray and the scattered X-ray signal.

The data collected for the different samples was compared with database

diffraction patterns for the different phases that were studied, including the JCPDS-ICDD Powder Diffraction File (Smith and Jenkins, 1996). The data was used for phase identification as well as to extract information about the microstructure of the coatings.

As well as the geometry of the thin films, the X-ray diffraction signal can provide information about the size and level of microstrain within the crystallites. The *Scherrer* equation (Klug and Alexander, 1974)

$$\tau = \frac{K\lambda}{\beta_P \cos\theta} \tag{3.2}$$

relates the full peak width β_P of the diffracted X-ray signal at half the maximum intensity (FWHM), the diffraction angle θ, the shape factor K, and the wavelength of the X-ray signal to the crystallite size τ.

Since line broadening can also be caused by inconsistencies in the diffractometer set-up and X-ray source, a coarse-grained, microstrain-free LaB_6 reference sample was used to produce a diffraction pattern with strain- and size broadening-free diffraction peaks over a wide range of angles of 2θ. Using the FWHM of these peaks a 2^{nd} order polynomial fit line was established for the relationship between the diffraction angle and the FWHM which equates to the instrument broadening β_I, which is subtracted from the FWHM to give the peak broadening caused by the crystallites studied. Figure 3.2 shows this 2^{nd} order polynomial fit line through the instrument broadening data.

Broadening of the diffraction peaks can also be caused by microstrain, which makes equation 3.2 valid only when there is no strain in the sample. Hall (1949) establishes that the line broadening β_S caused by microstrain,

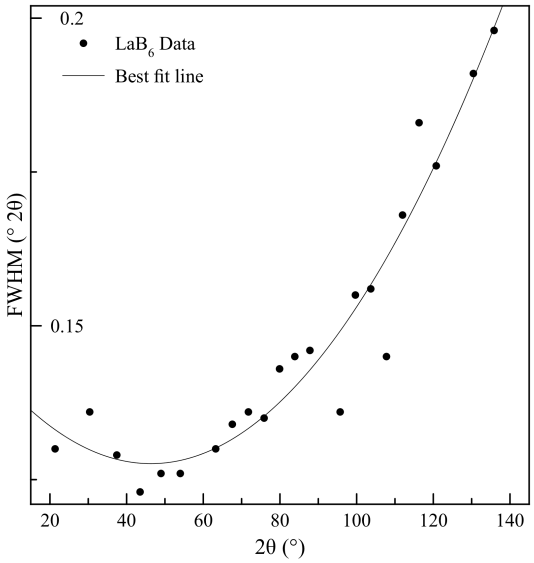

Figure 3.2: 2nd order polynomial fit line through the instrument broadening data for a LaB_6 reference sample

measured in values of 2θ, is linked with the broadening caused by small crystallites, β_P, via the relationship

$$\beta = \beta_P + \beta_S \tag{3.3}$$

which, given the relationship

$$\beta_S = -2\frac{\Delta d}{d}\tan\theta \tag{3.4}$$

derived by differentiating *Bragg's* law (equation 3.1), where the term $\frac{\Delta d}{d}$ is the effective strain, can be rearranged to give

$$\frac{\beta\cos\theta}{\lambda} = \frac{1}{\tau} - 2\frac{\Delta d}{d}\frac{\sin\theta}{\lambda} \tag{3.5}$$

which is known as the *Williamson-Hall* equation.

By plotting $\frac{\beta \cos\theta}{\lambda}$ against $\frac{\sin\theta}{\lambda}$ for a series of diffraction peaks, the microstrain and crystallite size can be derived from the slope and intercept of the resulting straight line *Williamson-Hall* plot (Cullity and Stock, 2001, chapt. 14), a representative example of which is shown in figure 3.3.

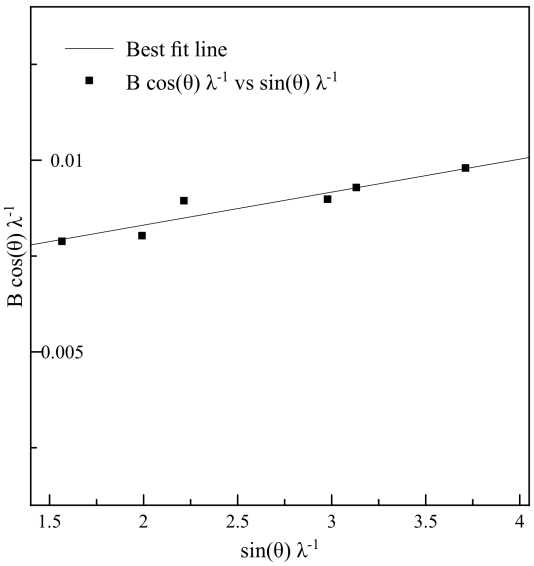

Figure 3.3: Williamson-Hall plot of the peak broadening data for the hydrogenated Mg/Cr sample

All samples were X-rayed on a Bruker D8 Advance diffractometer using monochromatic CuK_α radiation with a wavelength λ of 1.5418 nm, emitted through a 0.6 mm slit at 40 kV and 40 mA, in a Bragg-Bentano θ – 2θ configuration.

All samples were spun at the instrument-set speed of ca. 0.5 RPM during measurement to allow better crystallite homogenisation, and in the case of the as-deposited Mg/TM coating, the scan was complimented by a series of

unlocked-coupled scans. Since powder X-ray diffraction detects only planes of atoms which are parallel to the instruments horizontal plane, and assumes a random crystallite orientation, in a sample with strong crystal alignment this effectively tilts the sample, allowing the detection of planes of crystals that are not parallel to the horizontal plane.

Both the as-deposited thin film coatings and hydrogenated powders were scanned over a range of 20 – 100° 2θ, with a step size of 0.05° and a dwell time of 5 s for the coatings and with a step size of 0.03° and a dwell time of 10 s for the powders. The hydrogenated Mg/TM sample was scanned over a range of 20 – 85° 2θ, and the incident angles and 2θ ranges for the unlocked-coupled scans that were performed on the as-deposited Mg/TM sample with a step size of 0.05° and a dwell time of 15 s for the palladium peaks and 40 s for the magnesium peaks are presented in table 3.4.

Peak	Incident Angle	2θ range
Mg(104)	14.47°	79.10 – 84.50°
Mg(114)	9.38°	96.82 – 102.22°
Mg(105)	30.45°	101.95 – 107.35°
Pd(311)	9.93°	78.85 – 84.85°

Table 3.4: Table showing the scan parameters employed for the unlocked-coupled scans performed on the as-deposited Mg/TM coating

The as-deposited coatings were analysed on their glass substrate, which, due to the thickness of the coatings, did not interfere with the X-ray signal. During hydrogen cycling the samples decrepitated into a fine, flaky powder which was placed onto a single crystal silicone wafer in milligram quantities, oriented in such a way that it does not produce an X-ray diffraction signal using the $\theta - 2\theta$ Bragg-Bentano configuration. The hydrided powder samples

were placed onto the silicon wafers under argon and then covered with an amorphous polymer tape to limit oxidation of the hydride sample during the X-ray diffraction measurements.

3.3.2 Electron Microscopy

The microstructure and composition of the samples both before and after hydrogen cycling was analysed using a variety of electron microscopy imaging techniques including scanning electron microscopy (SEM), transmission electron microscopy (TEM) and energy-dispersive X-ray spectroscopy (EDX)

Scanning Electron Microscopy

Scanning electron microscopy works by scanning an electron beam across the surface of a sample. The interaction between the electron beam and the sample results in the emission of a range of waves and particles including secondary electrons, backscattered electrons and X-rays. In SEM, the secondary electrons provide information about the surface topography of the sample, whilst the backscattered electrons provide information about the atomic weight of the sample, resulting in Z-contrast. The X-rays emitted are a result of elastic collisions of the electron beam with the sample, providing information about the elemental composition of the sample.

The as-deposited thin film coatings' cross-sections and the hydrided powders were analysed by SEM using a Philips XL30 ESEM-FEG which was fitted with an Oxford Instruments silicon drift EDX detector. All imaging was done with an electron-beam voltage of 20 kV and at a working distance of 10 mm. The nitrocellulose-free glass coverslips that were coated alongside

the samples intended for delamination were fractured and mounted vertically on an SEM sample holder in order to observe and measure the thickness of the coatings. Charging of the non-conductive glass substrate was avoided by coating the fractured samples with a < 10 nm thick layer of platinum. EDX analysis was performed with the electron beam scanning an area of between 10 and 100 μm^2 on the surface of the coatings.

The hydrogenated coatings were imaged by dusting carbon tabs with a small amount of the thin film powders inside the argon glove box. The carbon tabs were then coated with a < 10 nm thick layer of platinum, in order to reduce oxidation of the powders during transfer into the electron microscope. A series of secondary electron images as well as backscattered electron images were produced in order to study the morphology of the hydrogenated samples. EDX analysis was used to study the elemental composition of the thin film powders.

Transmission Electron Microscopy

TEM analysis works by passing an electron beam through a sufficiently thin (typically < 100 nm) sample. As in SEM, a range of particles and waves, including secondary and backscattered electrons, and X-rays are emitted which can be used to analyse the elemental composition of the TEM sample. For TEM imaging however, the portion of the beam that is transmitted through the sample is used. A portion of the beam is scattered by the sample's crystal structure, resulting in contrast coming from the crystal structure of the sample in the remaining part of the electron beam.

The portion of the electron beam which is scattered by the crystal struc-

ture can be used to produce selected area electron diffraction patterns (SAED), which provide information about the crystal structure of the sample. These patterns appear in the form of a number of spots arranged in a circular fashion around the main electron beam, depending on the orientation of the crystallites present. Given a sufficient number of randomly oriented crystallites in the sample, producing a large number of spots, these can merge together to form a ring.

Bragg's law (equation 3.1) can be applied to these patterns, using the geometry between the the radius R of a diffraction ring, the camera length L which is fixed by the distance between the specimen and the photographic film or CCD used to record the TEM images, and the angle 2θ between the transmitted and the diffracted electron beam. Since θ is generally very small the approximation $\sin\theta \approx \theta$ can be made.

Therefore *Bragg's* law (equation 3.1) can be written as

$$n\lambda = 2d\theta. \tag{3.6}$$

The geometry of the TEM set-up dictates that $\tan 2\theta = R/L$ so that given $\tan\theta \approx \theta$ the equation

$$n\lambda L = Rd \tag{3.7}$$

can be derived by substituting θ in equation 3.6. Given the camera constant of 1.11 and 1.00 m respectively for both the JEOL 2100F and JEOL 2000FX II microscopes that were used in this work, and a wavelength of 2.5 pm for an electron accelerated by the 200 kV potential that was employed for TEM imaging, the radius of a diffraction ring can be used to calculate the d-spacing

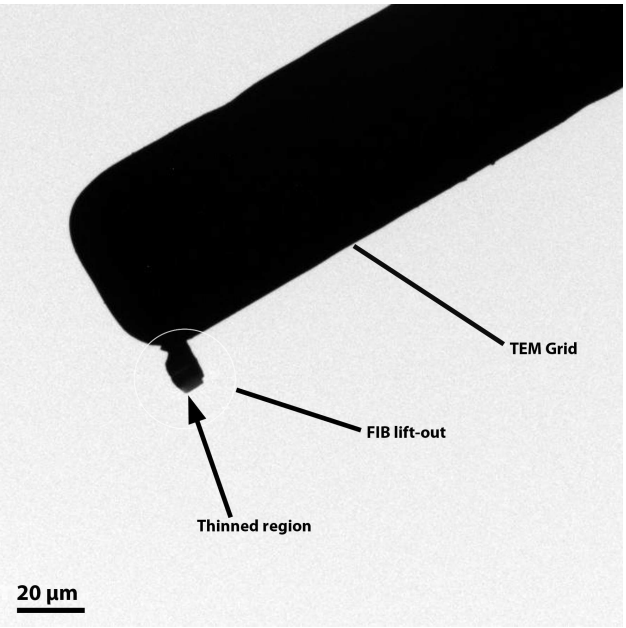

Figure 3.4: TEM image showing a FIB lift-out attached to a TEM grid

of the crystal plane it originates from.

TEM analysis was performed on the as-deposited Mg/TM, Mg/Cr and Mg/V samples, as well as on the hydrogenated Mg/TM, Mg/Cr and Mg/V samples. For the as-deposited thin film samples, FEI Quanta200 FIB/SEM and FEI Quanta 3D FEG FIB/SEM systems were used in the case of the Mg/TM and Mg/Cr samples, and the Mg/V sample respectively to produce TEM samples. In order to protect the multilayer structure, the samples were first coated with ca. 6 μm of tungsten following which a section was then milled out of the as-deposited samples using an ion beam. Figure 3.4 shows an example of one of the lift-outs which were were all 15 μm wide by 6 μm high (encompassing the multilayer as well as some of the glass substrate) and 250 nm thick. The ion beam was then used to thin the sample, to $<$ 150 nm in a wedge shape, producing regions of varying thickness. The lift-outs were

then mounted onto a copper TEM grid, in order to allow TEM imaging of the cross-section of the coatings. The samples were placed in liquid nitrogen and mounted onto a TEM sample holder in order to reduce oxidation during transfer into the JEOL 2100F transmission electron microscope that was used for the Mg/TM and Mg/Cr samples and the Philips Tecnai F20 microscope that was used for the Mg/V sample, fitted with Oxford Instruments INCA and ISIS EDX systems respectively.

A series of bright-field images were produced as well as electron diffraction patterns, confirming the microstructure of the thin film samples. In addition, scanning transmission electron microscopy (STEM) was used to generate high-angle annular dark field (HAADF) images which provide elemental (Z-)contrast, and nanometer-resolution EDX maps of the coatings' cross-section.

For TEM imaging of the hydrogenated powders a small amount (< 1 mg) of each of the samples was suspended in acetone in an argon environment. Outside the glove box, in a sealed glass vial, the suspension was treated in an ultrasound bath for 5 minutes and once the large particles, visible to the human eye, had settled to the bottom, a drop of the suspension was pipetted onto a holey carbon grid. With the carbon grid still moist with acetone in an attempt to minimise sample oxidation, the sample holder was mounted onto the TEM and evacuated. This caused the remaining acetone to evaporate, leaving very small thin film particles dispersed on the TEM grid.

The Mg/TM sample was imaged using the JEOL 2000FX II microscope, fitted with an Oxford Instruments INCA EDX system, whilst the Mg/Cr and Mg/V samples were imaged on the JEOL 2100F microscope. A series

of bright field images and diffraction patterns were collected for all samples, and the STEM functionality of the JEOL 2100F microscope was used for the Mg/Cr and Mg/V samples to generate EDX maps and HAADF images of the thin film particles.

3.4 Hydrogen Storage Measurements

The hydrogen storage properties of the thin film multilayers were measured using a range of volumetric, gravimetric and calorimetric methods including manually operated and automated Sievert's apparatuses, thermogravimetric analysis (TGA) and differential scanning calorimetry (DSC) in order to assess the capacity, thermodynamics, kinetics and cycling behaviour of the thin film materials.

3.4.1 Volumetric Sorption Methods

For a given volume, temperature and hydrogen pressure, the amount of hydrogen gas contained in the volume can be calculated using the virial equation (equation 3.8)

$$\frac{p\overline{V}}{RT} = 1 + B(T)\frac{1}{\overline{V}} + C(T)\frac{1}{\overline{V}^2} \tag{3.8}$$

relating the pressure p, molar volume $\overline{V}$, gas constant R, number of moles n and temperature T to the temperature dependent virial coefficients $B(T)$ and $C(T)$ which can be found in databases such as the one published by NIST (NIST, 2009).

If the volume of hydrogen gas (manifold) is then connected to a second volume containing a hydrogen storage material under vacuum (sample holder),

the pressure of the same amount of hydrogen gas expanded into the sum of the two volumes can be calculated. If the hydrogen storage material then absorbs a portion of the gas, a pressure drop will ensue. This pressure drop can be measured and used to calculate the quantity and mass of gas that has been absorbed by the hydrogen storage material and, given the mass of the hydride material (typically around 150 mg), the hydrogen storage capacity can be derived.

A twin-manifold Sievert's system, a schematic of which is shown in figure 3.5, was built using a Druck PTX 620-I pressure transducer with an accuracy of 0.08% FS and a range of 0 – 100 bar. The system was encased in an acrylic glass box and mounted on an aluminium frame in order to allow an arrangement of heaters, fans and thermocouples to maintain a constant temperature of 35 $\pm$ 0.5°C. The switchable manifold volume allowed switching between two different-sized manifold volumes by opening or closing the associated ball valve. The manifold was connected to hydrogen (purity 99.9999%) and helium (purity 99.996%) gas supplies as well as a Pfeiffer TPS 100 turbomolecular vacuum system, backed by an oil-free diaphragm pump.

The sample holder was fitted with a Watlow ring heater, which allowed temperature control within $\pm$ 1°C. Heat transfer between the ring heater and the sample was accounted for by measuring the temperature of the inner wall of the sample holder and recording it against the heater temperature. In the range of 250 – 350°C that was used for hydrogen storage measurements an offset of +7°C was measured between the temperature on the in- and outside of the sample vessel, which was used to estimate the sample temperature from the heater temperature.

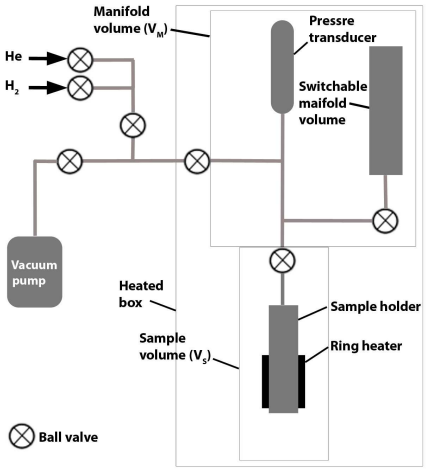

Figure 3.5: Schematic showing the twin-manifold Sievert's apparatus

The system volume was calibrated using stainless steel ball bearings and helium gas. The diameter of these ball bearings was measured in order to establish their volume, V_B, and they were then added to the sample holder volume V_S in three portions, providing 4 different sample volumes with a known ΔV. The mass of the gas in the system remains constant and hence, when opening the pressurised manifold volume V_M into the evacuated sample volume containing ball bearings (V_S - xV_B)

$$V_M \rho_M = (V_M + V_S - xV_B)\rho_{total} \tag{3.9}$$

is valid for the density ρ_M of the gas in the manifold and ρ_{total} for the gas expanded into the sample holder.

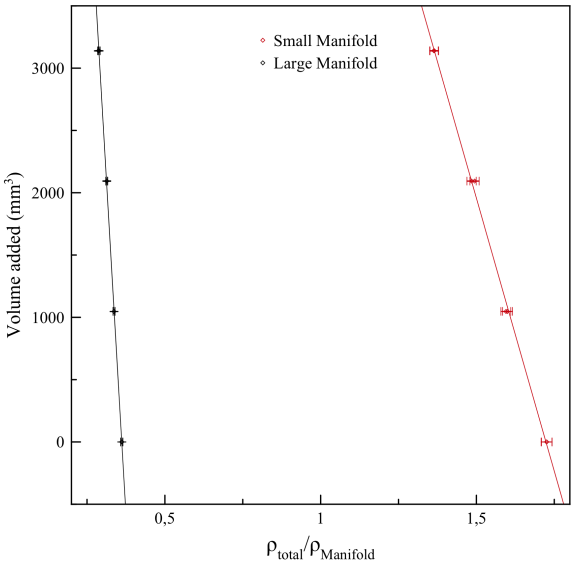

Figure 3.6: Graph showing the calibration data and linear regression lines for the twin-manifold Sievert's apparatus used in this work

This can be re-arranged to form

$$[(\frac{\rho_{total}}{\rho_M}) - 1]V_M = (V_S - xV_B) \tag{3.10}$$

where x is the number of ball bearings added to the sample holder, and by noting the pressure before and after expanding the helium gas from the manifold into the sample holder, using equation 3.8, the densities ρ_M and ρ_{total} of the gas can be calculated. By plotting $(\frac{\rho_{total}}{\rho_M})$ against xV_B for a range of x, the volumes V_M and V_S can be derived from the slope and intercept of the resulting straight line.

Figure 3.6 shows the calibration curves with two values measured for each of the 4 different sample volumes for the twin-manifold Sievert's apparatus that was used in this work. The manifold volumes were determined to be

42.76 ± 0.5 cm^3 and 8.76 ± 0.1 cm^3 for the large and small manifold respectively. Given the manifold volume, pressure and temperature, the effective volume of any sample holder containing an amount of hydrogen storage material at elevated temperature can be calculated using equation 3.10. This was done twice for every sample at every temperature in order to obtain an average value of the effective sample holder volume for each set of experiments.

Having two manifold volumes allows the more accurate measurement of both pressure-composition isotherms, since in a smaller volume a small amount of gas creates a larger change in pressure, and kinetic curves, since a larger manifold will allow the complete hydrogenation and dehydrogenation of a sample, providing a sufficiently small drop or increase in pressure to ensure sufficient over- or under pressure is present to complete the reaction. The lab-built Sievert's apparatus was used for the activation of the Mg/TM sample, presented in section 4.3.4, and to produce the dehydrogenation isotherms for the Mg/Cr, Mg/V and $Mg_{control}$ samples, presented in section 4.3.1.

In addition, a commercial, fully automatic Setaram PCTpro2000 Sievert's apparatus was used for hydrogen cycling experiments. The automation feature facilitated hydrogen cycling and PCI experiments whilst the large manifold volumes available on this instrument allowed the measurement of hydrogenation and dehydrogenation kinetics at reduced temperatures. The instrument has a known error of 1% of the reading of pressure and an accuracy of ± 5°C for the sample temperature control. The manifold temperature is set to 30 ± 1°C and in addition it was noticed that the temperature inside

the instrument follows a sinusoidal pattern varying ± 0.25 °C in a period of 40 min which gives rise to a degree of noise, especially for measurements taken using large manifold volumes. The PCTpro2000 was used to measure the pressure-composition isotherms for the Mg/TM sample, presented in section 4.3.1 and for the measurements of activation, kinetics and cycling stability presented in sections 4.3.4, 4.3.2 and 4.3.6.

3.4.2 Gravimetric Capacity Measurements

In addition to volumetric methods, gravimetric methods were used to asses the hydrogen storage capacity of the thin film multilayer samples. A Netzsch 209 F1 Iris thermobalance was used for thermogravimetric analysis (TGA) of the samples which has a resolution of 1 μg and a temperature range of 20 – 1000°C.

After 50 – 60 cycles of hydrogenation and dehydrogenation, approximately 2 – 3 mg of each hydrided sample was placed into an alumina crucible, which was encapsulated by an aluminium pan and lid arrangement, which was sealed in order to minimise oxidation of the samples during transfer from the argon glovebox to the instrument. The aluminium casings were then pierced with a needle to allow hydrogen gas to escape during the dehydrogenation experiments and the samples were placed on the instrument's sample carrier. The instrument then went through several cycles of evacuation and purging with argon, before starting the dehydrogenation experiments. The sample was held at a constant temperature of 30°C for 1 h in order to allow the system to stabilise and to establish a baseline under a flow of 100 ml min^{-1} of argon at atmospheric pressure, before measuring the mass loss during a

continuous heating process at $10^{\circ}\mathrm{C\,min^{-1}}$ from room temperature to up to 500°C under the same conditions.

In order to account for buoyancy, heat convection and gas flow effects interacting with the sample, an empty alumina crucible, encapsulated in an aluminium pan and lid, was placed on the microbalance and run under identical conditions to those employed for the hydride samples. From the difference between the two curves the true mass loss of the sample due to hydrogen evolution was determined.

3.4.3 Calorimetric Measurements

Differential scanning calorimetry (DSC) measures the heat flux into and out of a sample, providing information about the exothermic and/or endothermic nature of a chemical reaction. By heating a small amount (2 – 3 mg) of the hydrogenated thin film samples, placed in an alumina crucible encapsulated by an aluminium pan and lid arrangement identical to that used for the TGA measurements, at a controlled rate in a controlled atmosphere and comparing the heat flux to that into and from a reference sample consisting of a blank alumina crucible encapsulated in aluminium identical to the one used to account for buoyancy effects during TGA measurements, the heat flux necessary to undergo a chemical reaction in the hydrogen storage material can be measured.

After 50 – 60 cycles of hydrogenation and dehydrogenation, the hydrided samples were heated from room temperature under a 100 $\mathrm{ml\,min^{-1}}$ flow of argon at atmospheric pressure, at rates of 2, 5, 10 and $20^{\circ}\mathrm{C\,min^{-1}}$ to temperatures of up to 450°C in a series of dehydrogenation experiments. Upon

completion of each dehydrogenation experiment, the flow of argon was cut and hydrogen was introduced into the reaction chamber at 10 bar, after 3 cycles of purging the chamber with 3 bar of hydrogen. The sample was held for 30 minutes at 310°C under a flow of 200 $\mathrm{ml\,min^{-1}}$ of hydrogen to allow complete hydrogenation, as established previously from the volumetric kinetics experiments that were done at similar temperatures. Once the samples had cooled to room temperature, the chamber was purged 3 times with 3 bar of argon. The argon flow was once again set to 100 $\mathrm{ml\,min^{-1}}$ for the next dehydrogenation experiment. This data was then used in the evaluation of the reaction kinetics of the thin film multilayer samples using Kissinger analysis.

Homer Kissinger (Kissinger, 1956) describes a method of establishing the activation energy of a reaction using DSC. Using the equation Murray and White (1955) derive from the Arrhenius equation (4.3), where

$$Ae^{-\frac{E}{RT}} = \frac{E}{RT_m^2}\frac{dT}{dt} \tag{3.11}$$

he states that

$$\frac{d(\ln \frac{\phi}{T_m^2})}{d(\frac{1}{T_m})} = -\frac{E}{R} \tag{3.12}$$

where the heating rate $\phi = dT/dt$, also referred to as β (Varin *et al.*, 2008) or Q (Kelton, 1997), whilst E is the activation energy referred to in this work as E_a and T_m is the temperature at which a local maximum occurs for a DSC curve, referred to here as T_{peak}. This relationship is then used to derive the activation energy E_a from plots of $1/T_{peak}$ against $ln(\beta/T_{peak}^2)$ as shown in section 4.3.3.

Chapter 4

Results

4.1 Introduction

Thin film technology is becoming ever more common in the development of magnesium-based hydrogen storage materials due to the high level of flexibility and control the process offers in manufacturing nano-scale structures. As established in section 2, in an attempt to promote faster hydrogen storage kinetics at reduced temperatures, researchers have produced a range of thin film composites, alloys and multilayers with some success. It is well known that certain transition metals such as Cr, Fe, Ni, V, Ti and their oxides can act as catalysts, improving the reaction kinetics of hydrogen storage in magnesium. It is also well known that having a good dispersion of very small catalyst particulates in very fine-grained magnesium is favourable for fast kinetics whilst retaining as much hydrogen storage capacity as possible (Varin *et al.*, 2006b; Zaluska *et al.*, 2001). These conditions are fulfilled by thin film multilayers made up of very thin (< 20 nm) layers of magnesium separated by extremely thin (< 3 nm) layers of transition metal, with the exact thickness of the layers depending on the desired magnesium-to-transition metal ratio.

This promotes a very high area of contact between the active magnesium and the catalyst. Magnetron-assisted physical vapour deposition (PVD) is a thin film technique that allows atom-by-atom "tailoring of structures"(Qu *et al.*, 2010c), enabling the controlled and repeatable manufacture of highly structured multilayer thin films. The work presented in this chapter investigates the interaction of a range of such magnesium/transition metal thin film multilayers with hydrogen and the structural evolution of the materials during hydrogen cycling at elevated temperatures.

Sections 4.2 and 4.3 present the structural characterisation and hydrogen storage properties of the multilayer samples of magnesium multilayered with a nickel-rich transition metal mix (Mg/TM), chromium (Mg/Cr) and vanadium (Mg/V) as well as a non-catalysed magnesium control sample ($Mg_{control}$), prepared as discussed in section 3.2.1. The materials were investigated using XRD, SEM, TEM and EDX to determine the structural evolution the materials underwent during over 60 cycles of hydrogenation and dehydrogenation, and a combination of Sievert's-type apparatuses, DSC and TGA was used to determine the kinetic and thermodynamic properties of the thin film samples. Chapter 5 will then discuss the findings relating how the structural evolution and the different materials used affect the hydrogen storage properties of these materials.

4.2 Structural Characterisation of Thin Film Multilayers

4.2.1 X-Ray Diffraction

XRD studies were carried out in order to study the microstructural changes that the different multilayer materials underwent during hydrogen cycling at elevated temperatures. Diffractograms produced by performing locked-coupled scans of the Mg/TM, Mg/Cr, Mg/V and $Mg_{control}$ samples in their as-deposited state are presented in figure 4.1.

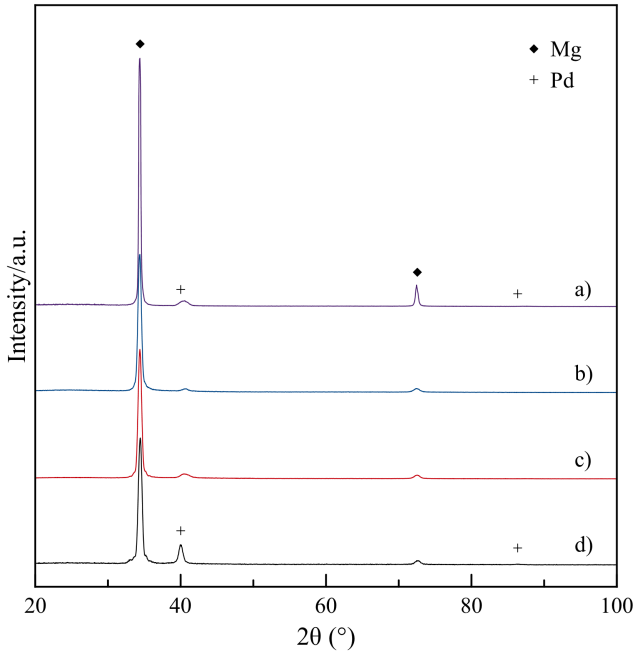

Figure 4.1: XRD pattern in the as-deposited state of the a) $Mg_{control}$, b) Mg/V, c) Mg/Cr and d) Mg/TM samples.

All 4 samples show clear diffraction peaks from the (002) and (004) planes of the magnesium phase at 34.4 and 72.5° 2θ, as well as from the (111) and,

in the case of the Mg/TM coating, also the (222) planes from the palladium capping layers at 40.1 and 86.6° 2θ. The samples exhibit signs of strong directional growth of magnesium crystals in the <001> direction and growth in the <111> direction for the palladium layers and there is no evidence of diffraction from any of the transition metal interlayers in the Mg/TM, Mg/Cr and Mg/V diffraction patterns. There is however evidence for a shift to higher angles of 2θ by ca. $0.4 \pm 0.05°$ ($\triangleq$ 0.01 Å) of the palladium (111) peaks coming from the Mg/Cr, Mg/V and $Mg_{control}$ samples.

Figure 4.2 shows a series of unlocked-coupled scans that were performed on the Mg/TM sample to confirm the crystal structure and orientation of the magnesium and palladium crystals superimposed on a section of the original locked-coupled scan of the same sample. Diffraction peaks can be observed from the (311) planes in the palladium layers (82.1° 2θ) and the (104), (114) and (105) planes in the magnesium layers (81.54, 99.22 and 104.25° 2θ) by adjusting the incident angle of the X-ray source by the interplanar angle between the basal planes and the planes in question.

As described in section 3.3.1, the *Scherrer* equation (equation 3.2) was applied to the full width at half of the maximum intensity (FWHM) of the magnesium (002) and (004) diffraction peaks and an average value for the crystalline size of ca. 16 ± 3 nm was estimated. The palladium (111) and (222) peaks were used in a similar fashion to calculate an average grain size of the palladium crystallites of ca. 14 ± 2 nm. Peak broadening measurements were also done for the Mg/Cr, Mg/V and $Mg_{control}$ samples and from the peak broadening at FWHM of the respective diffraction peaks of the (002) and (004) planes the average crystallite size for the Mg phase was estimated

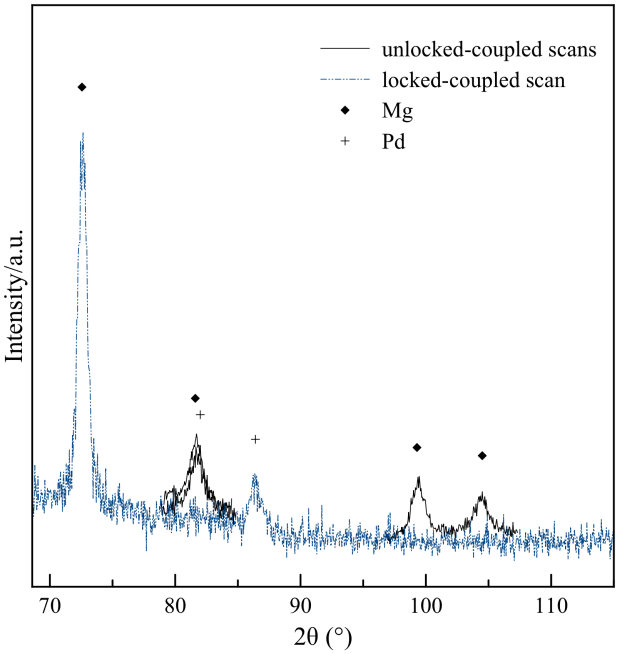

Figure 4.2: XRD pattern showing a series of unlocked-coupled scans overlaid on the original locked-coupled scan of the as-deposited Mg/TM thin film between 2θ values of $80 - 120^{\circ}$

at ca. 17 ± 3 nm for the Mg/Cr coating, 16 ± 3 nm for the Mg/V coating and 50 ± 16 nm in the case of the $Mg_{control}$ sample.

The as-deposited and then delaminated samples were all of shiny, metallic appearance but, after up to 60 cycles of hydrogen cycling at up to 350°C, all 4 samples had undergone significant morphological changes. To the naked eye, the samples seemed to have disintegrated into very fine, grey, flaky powders which facilitated further characterisation using SEM, TEM, XRD, DSC and TGA. X-ray diffraction patterns from these powders reveal that there was significant change, not only in the morphology of the samples, but also in the microstructure.

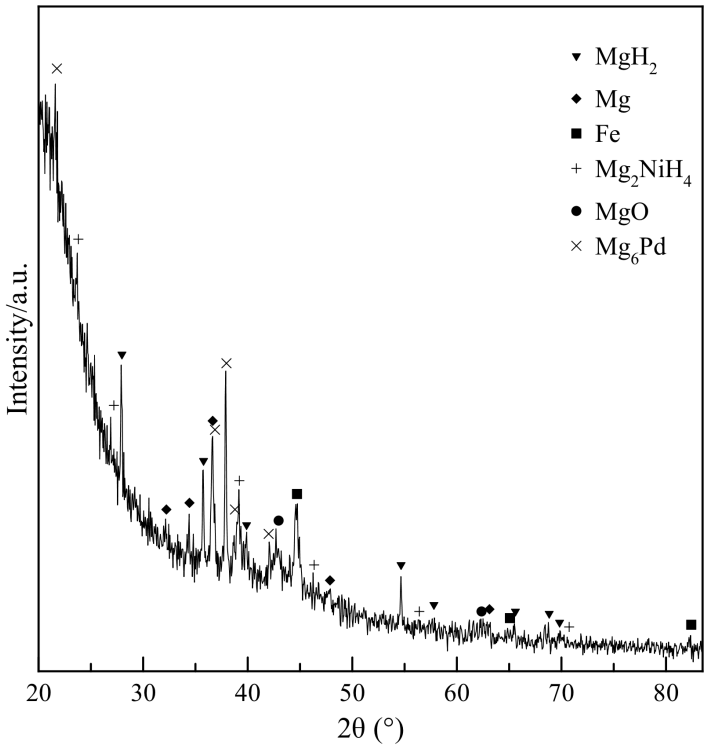

Figure 4.3: XRD pattern of the hydrogenated Mg/TM sample after 60 cycles of hydrogenation and dehydrogenation

The diffraction pattern for the hydrogenated Mg/TM sample shown in figure 4.3 suggests a significant change of the material's crystal structure after hydrogen cycling. As well as diffraction lines corresponding to magnesium hydride, magnesium oxide (periclase) and traces of unreacted magnesium, the diffraction pattern suggests the presence of Mg_6Pd and Mg_2NiH_4 phases as well as a crystalline, body centred cubic (BCC) iron. Furthermore, the diffraction peaks have become sharper which suggests that, as well as the formation of new phases, a degree of grain growth has occurred during hydrogen cycling.

The peak broadening of the magnesium hydride peak at around 54.7° 2θ was used to calculate an average grain size of the magnesium hydride phase post cycling of around 85 ± 35 nm. The broadening of the iron peak at around 36.6° 2θ corresponds to a grain size of ca. 50 ± 16 nm. The peaks corresponding to the Mg_2NiH_4, Mg_6Pd and periclase phases were too convoluted and weak in intensity to extract any useful information about the grain size of these phases.

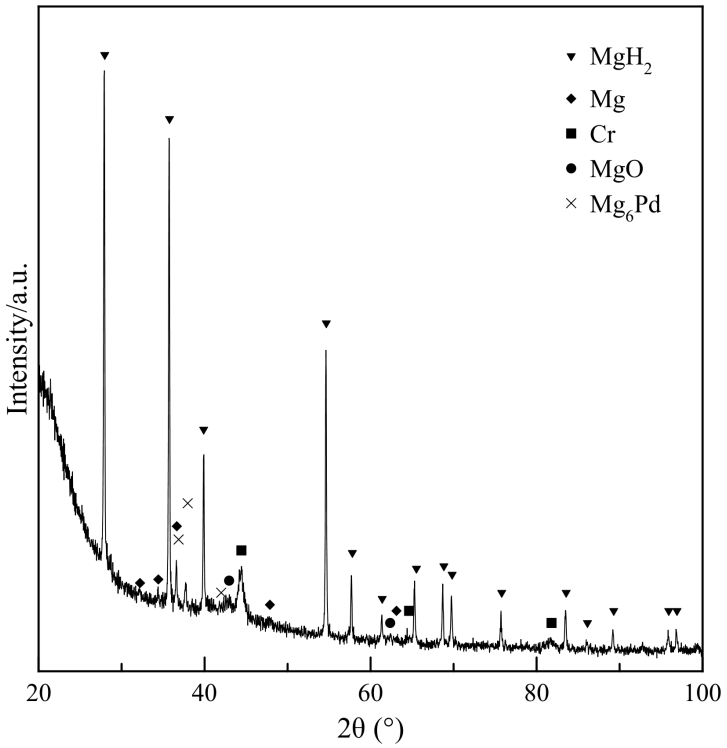

Figure 4.4: XRD pattern of the hydrogenated Mg/Cr sample after 60 cycles of hydrogenation and dehydrogenation

Similar measurements were performed for the Mg/Cr, Mg/V and $Mg_{control}$ samples. Figure 4.4 shows a diffraction pattern for the hydrided MgCr sample

after 60 cycles of hydrogenation and dehydrogenation. The pattern reveals significant changes in the material's crystal structure during hydrogen cycling. Diffraction peaks matching database values of magnesium hydride, as well as much lower intensity peaks corresponding to patterns of magnesium, magnesium oxide (periclase), Mg_6Pd and crystalline, BCC chromium can be identified. The average grain size of the magnesium hydride phase was estimated to be ca. 136 $\pm$ 50 nm from the peak broadening at full width half maximum using the *Williamson-Hall* plot shown in figure 3.3. The *Scherrer* equation was applied to the chromium peak from which a crystallite size of ca. 20 $\pm$ 5 nm was derived. The magnesium oxide peaks, although detectable, were, in the case of the peak at 62.4° 2θ, too low in intensity and, in the case of the peak at 43° 2θ, too convoluted with the Mg_6Pd peak at 41.7° 2θ to extract useable information about the crystallite size of the oxide phase.

After hydrogen cycling the now hydrided Mg/V sample exhibited a very different diffraction pattern from that of the as-deposited sample. Shown in figure 4.5, the pattern exhibits a series of intense, sharp looking peaks that match database values for magnesium hydride. In addition the pattern contains a range of smaller peaks that match database values for magnesium, magnesium oxide (periclase), V and Mg_6Pd. Using *Williamson-Hall* plots the average grain size of the magnesium hydride phase was estimated to be ca. 100 $\pm$ 39 nm from the peak broadening of the corresponding peaks. The magnesium oxide, vanadium and Mg_6Pd peaks are too convoluted with the neighbouring peaks to be able to extract the FWHM.

Figure 4.6 shows a diffraction pattern of the $Mg_{control}$ sample after hy-

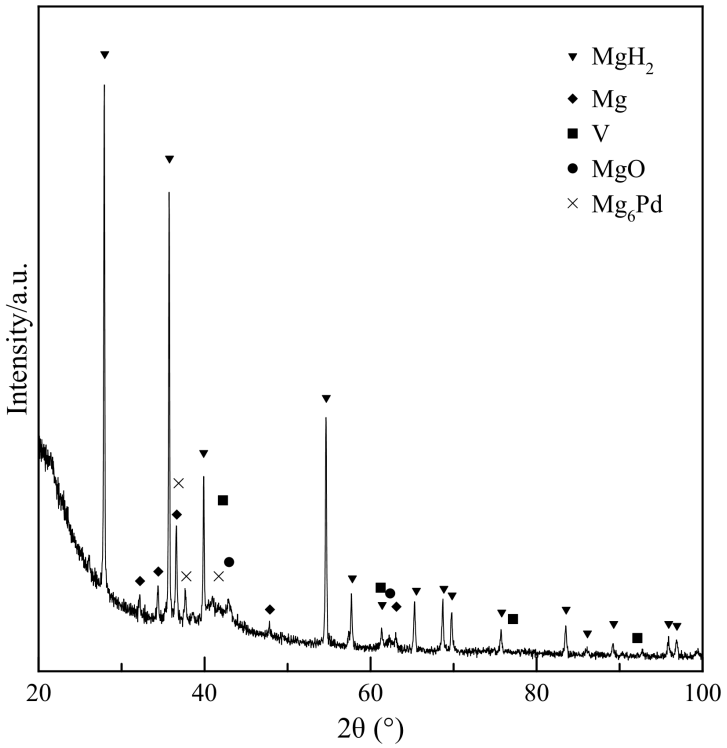

Figure 4.5: XRD pattern of the hydrogenated Mg/V sample after 60 cycles of hydrogenation and dehydrogenation

drogen cycling and one of as-received magnesium hydride (Alfa Aesar, 98% MgH_2). The $Mg_{control}$ sample's pattern contains low intensity peaks matching database patterns for magnesium, magnesium oxide (periclase) and Mg_6Pd in addition to a strong magnesium hydride pattern. The magnesium hydride peaks are very sharp and thus make an estimation of the grain size using the peak broadening impossible as the grain size exceeds the limit of grain size that can be measured using XRD. The *Scherrer* equation was used to estimate the crystallite size of the periclase phase at around 22 ± 6 nm from the FWHM of the magnesium oxide peak at around 43° 2θ.

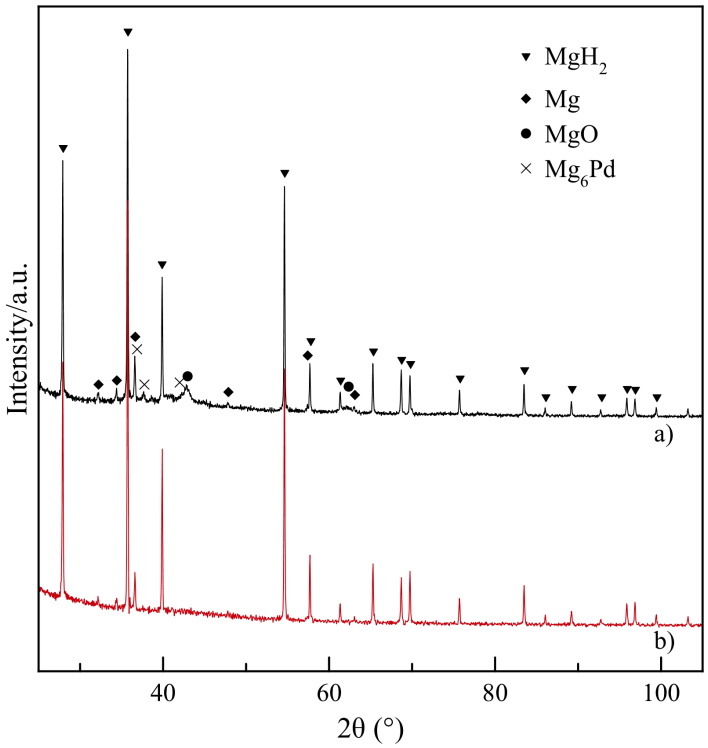

Figure 4.6: XRD patterns of a) the hydrogenated $Mg_{control}$ sample after 60 cycles of hydrogenation and dehydrogenation and b) as-received magnesium hydride

Similarly the pattern of the as-received magnesium hydride powder exhibits sharp peaks matching database values for magnesium hydride as well as low-intensity peaks corresponding to the diffraction pattern of magnesium.

4.2.2 Electron Microscopy

SEM

Electron microscopy studies by SEM and TEM were conducted to understand the structural changes the different multilayer materials underwent during hydrogen cycling.

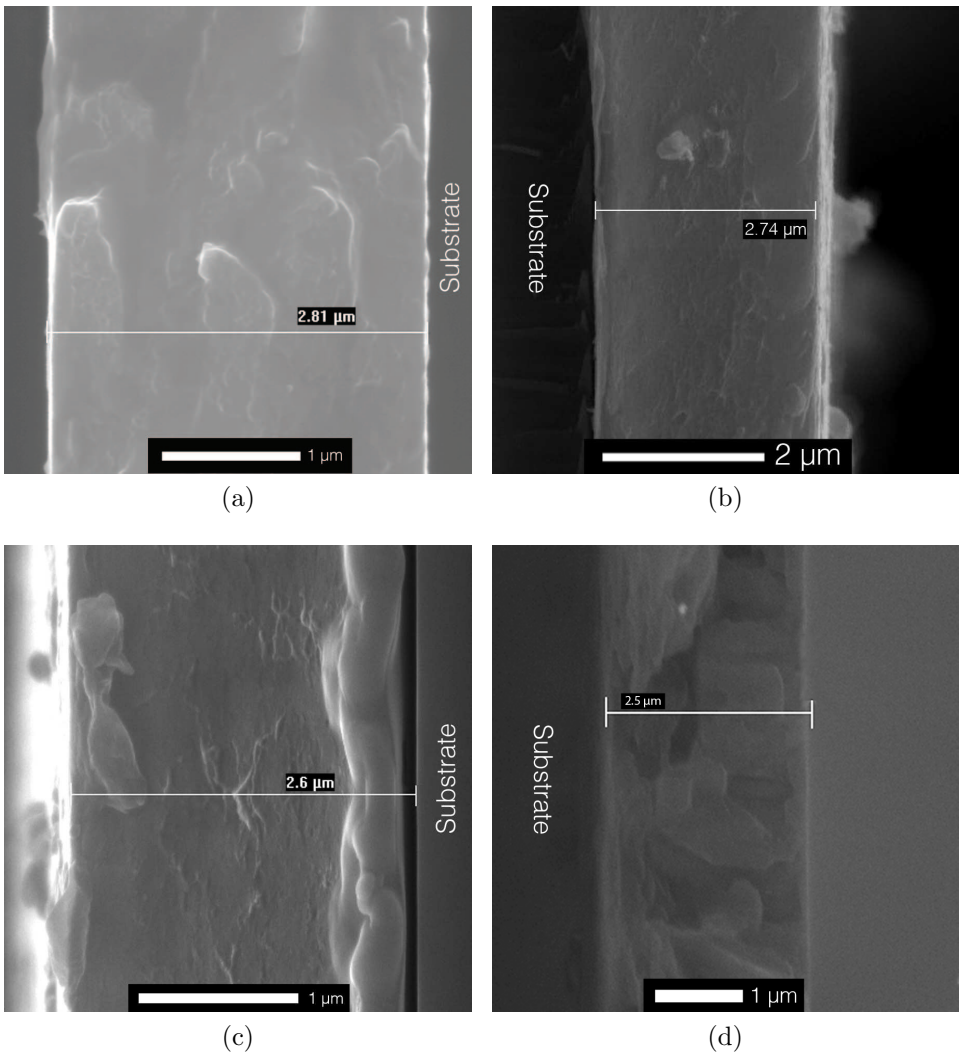

Figure 4.7: Cross-sectional SEM images of the a) Mg/TM, b) Mg/Cr, c) Mg/V and d) $Mg_{control}$ samples showing the thickness of the as-deposited thin films

Figure 4.7 shows SEM micrographs of the cross-section of the Mg/TM, Mg/Cr, Mg/V and $Mg_{control}$ multilayer thin films in their as-deposited state, revealing the total film thicknesses of the samples as 2.81 ± 0.1, 2.74 ± 0.1, 2.6 ± 0.1 and 2.53 ± 0.1 μm respectively. The thickness of the 4 samples in the region of 2.53 – 2.81 μm, given that around 40 25.4 × 76.2 mm glass slides were coated for each sample, resulted in around 300 mg of useable hydrogen storage material after sample delamination. This allowed volumetric and gravimetric hydrogen uptake measurements using conventional Sievert's and thermogravimetric apparatuses as opposed to using resistive or optical methods which, as discussed in section 2.2.3, are often relied upon to measure hydrogen uptake in thin films.

Figure 4.8a shows SEM images of the Mg/TM powder after 60 cycles of hydrogenation and dehydrogenation in its hydrogenated state. The image reveals that the powder-like sample retained some of its thin-film structure, containing flaky particles of a wide range of sizes ranging from tens of nanometres to tens of millimetres. Figure 4.8b and 4.8c show backscattered and secondary electron images of an Mg/TM particle that is representative of the smallest particles in the sample. By comparing the two images it becomes evident that there are a large number of very small, bright, circular features in, on or under the particle which, given the backscattered electron contrast, is indicative of nano-sized particles of elements heavier than the bulk of the material. This might suggest that the amorphous, uniformly distributed layers of catalyst material have formed a number of nano-sized particles during hydrogen cycling. Figure 4.8d shows one of the larger flakes in the Mg/TM sample, highlighting that these particles are porous and appear to be made

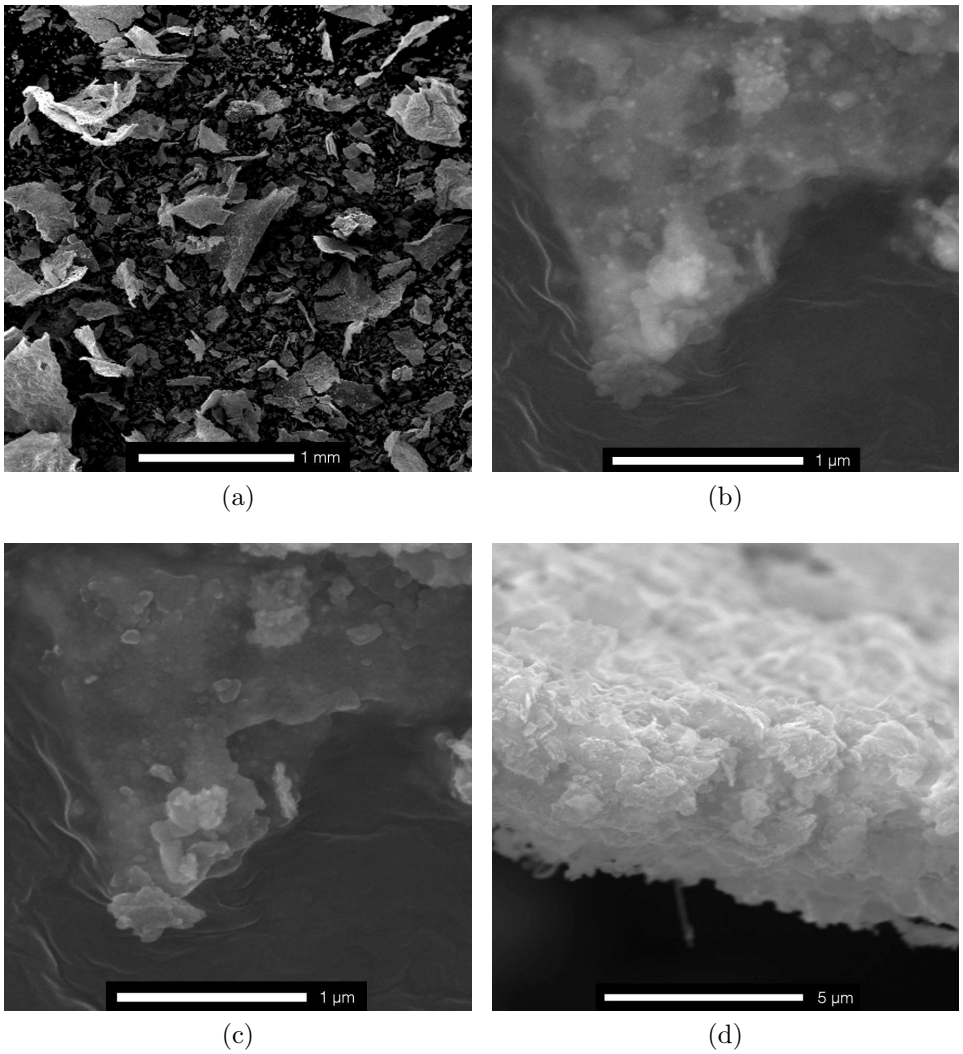

(a) (b)

(c) (d)

Figure 4.8: SEM images of the Mg/TM sample in its hydrogenated state after 60 cycles of hydrogenation and dehydrogenation showing a) a low-magnification view of the powder morphology, b) a high-magnification backscattered electron image of a small Mg/TM particle, c) a high-magnification secondary electron image of a small Mg/TM particle and d) an image of a larger Mg/TM flake

up of much smaller flakes in random orientation.

Figures 4.9 and 4.10 contain a collection of images showing the morphology of the Mg/Cr, Mg/V and $Mg_{control}$ samples after 60 cycles of hydro-

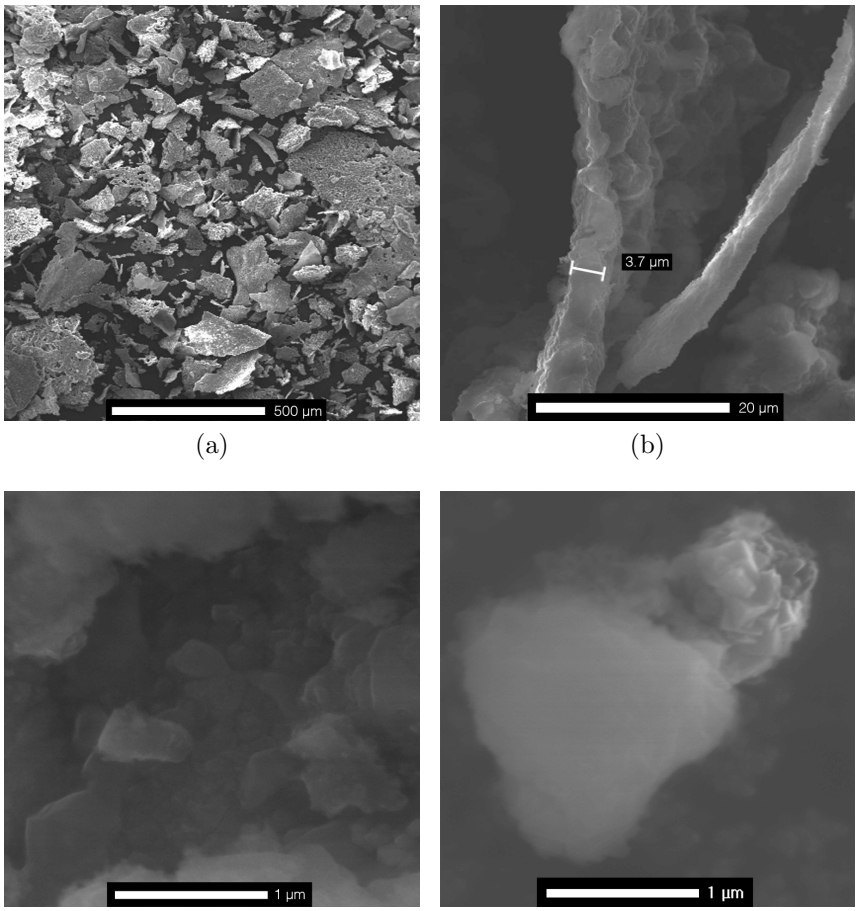

(a) (b)

(c) (d)

Figure 4.9: SEM images of the Mg/Cr and Mg/V samples in their hydrogenated state after 60 cycles of hydrogenation and dehydrogenation showing a) a low-magnification view of the Mg/V powder morphology, b) a larger Mg/V flake illustrating the cross-section of a hydrogenated thin film flake, c) a high-magnification secondary electron image showing a small Mg/Cr particle and d) a high-magnification secondary electron image showing a small Mg/V particle

genation and dehydrogenation in their hydrogenated state. Figure 4.9a is representative for both the Mg/Cr and Mg/V samples, and both samples appear to be made up of a mixture of what looks like porous thin film flakes and smaller particles which, as shown in the higher magnification image in

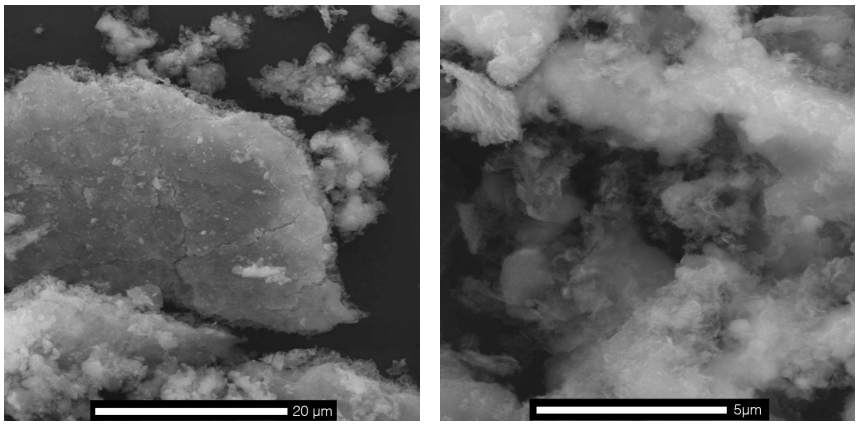

(a) (b)

Figure 4.10: SEM images of the $Mg_{control}$ sample in its hydrogenated state after 60 cycles of hydrogenation and dehydrogenation showing a) a low-magnification view of the $Mg_{control}$ sample's morphology and b) a high-magnification secondary electron image highlighting the smaller $Mg_{control}$ particles

figures 4.9c and 4.9d, themselves appear to be made up of thin plates of material. The $Mg_{control}$ sample on the other hand, although similar in terms of particle size, exhibits different morphological features. As demonstrated in figure 4.10a the sample also contains what looks like porous flakes. These flakes differ from the catalysed samples however in that they appear to have a smoother surface. The smaller particles shown in figure 4.10b have a different texture to that found in the catalysed samples. The sample is porous in appearance and lacks the plate-like structures seen in the other samples.

All particles have in common the fact that they have retained a large width to thickness ratio where the thickness is consistently significantly smaller than the width and height, resulting in the flat, flake-like appearance of the powder. Figure 4.9b is representative for all samples, showing that this thickness is not the same thickness as the original, as deposited

thin film or indeed the same for all particles and suggests the thin film has disintegrated not only in the thin film growth direction but also in planes parallel to the thin film surface. The thickness of this particle, one of the the largest and therefore most intact thin film flakes from the Mg/V sample, was measured at 3.7 ± 0.2 μm.

EDX data was collected both for the thin film samples and the hydrogenated powders in order to assess the composition of the samples. In the case of the as-deposited thin films EDX data was collected in a selected area in the range of 10-100 μm^2 on the surface of the thin film whilst the data for the thin film powders was collected from the bulk in an area covering 5-10 thin film flakes. Tables 4.1 and 4.2 show a comparison of the 4 different samples' compositions, both in the thin film state and in the hydrogenated state post cycling.

	Mg/TM at.%	Mg/Cr at.%	Mg/V at.%	Mg at.%
Mg	87.7 ± 0.5	96.3 ± 0.4	94.1 ± 0.4	99.4 ± 0.4
Ni	6.9 ± 0.1	0	0	0
Fe	3.5 ± 0.1	0	0	0
V	0	0	5.2 ± 0.2	0
Cr	0.9 ± 0.1	3.3 ± 0.1	0	0
Mn	0.1 ± 0.1	0	0	0
Pd	0.9 ± 0.1	0.4 ± 0.1	0.7 ± 0.1	0.6 ± 0.1

Table 4.1: Composition of the 4 thin film multilayer samples in their as-deposited form measured by EDX

	Mg/TM at.%	Mg/Cr at.%	Mg/V at.%	Mg at.%
Mg	87.8 ± 0.4	95.1 ± 0.4	93.0 ± 0.4	99.2 ± 0.4
Ni	6.3 ± 0.1	0	0	0
Fe	3.3 ± 0.1	0	0	0
V	0	0	6.4 ± 0.2	0
Cr	0.9 ± 0.2	4.3 ± 0.2	0	0
Mn	0.1 ± 0.1	0	0	0
Pd	1.6 ± 0.1	0.6 ± 0.1	0.6 ± 0.1	0.8 ± 0.1

Table 4.2: Relative composition of the metal elements in the 4 thin film multilayer samples in their hydrogenated powder form after 60 cycles of hydrogenation and dehydrogenation measured by EDX

TEM

The physical set-up of the PVD coating unit as described in section 3.2 dictates that a layer of transition metal is deposited onto the palladium coated substrate, followed by a layer of magnesium, which in turn is followed by a layer of transition metal and so on, until the process is completed with a final transition metal and palladium capping layer.

The TEM images presented in figures 4.11 and 4.12 show a series of images of a FIB-SEM lift-out taken from the Mg/TM sample. These images confirm that the coating conditions did in fact result in 150 bi-layers in the thin film with alternating magnesium and transition metal layers. Figure 4.11a shows the full cross-section through the Mg/TM thin film showing clearly the uniform, orderly nanostructure of the thin film throughout the entire coating. The convergent beam electron diffraction pattern shown in inlay i) was taken from the small area, centrally located within the cross section of the sample, highlighted in inlay ii), incorporating a transition metal interlayer and about half of the two neighbouring magnesium layers, in the central

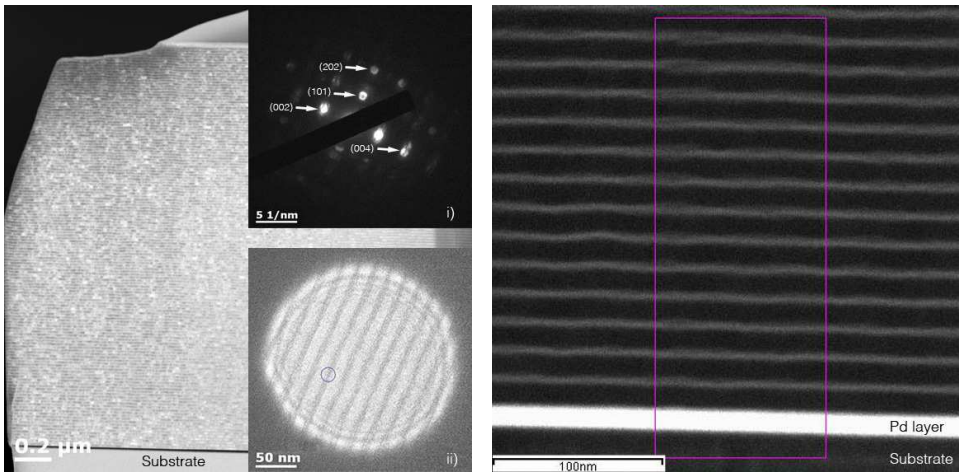

(a) (b)

Figure 4.11: Cross-sectional TEM images of a FIB-SEM lift-out of the Mg/TM thin film multilayer in its as-deposited state showing a) a view of the entire multilayer structure on the glass substrate with i) a convergent beam electron diffraction pattern from the area highlighted in ii), located in the central region of the multilayer structure and b) a high-angle annular dark-field (Z-contrast) image of the first 14 bi-layers

region of the sample. The pattern exhibits only characteristic discs for HCP magnesium crystallites with no evidence of crystallinity in the transition metal interlayer. Figure 4.12a shows a high-resolution TEM image of the uppermost 4 bi-layers of the thin film coating which highlights the uniform structure of layer separation present throughout the entire cross-section of the Mg/TM sample.

The thickness of the individual magnesium and transition metal layers was measured by intensity profiling across several multilayers using high-resolution TEM images such as the one shown in figure 4.12b. An average thickness of 16.5 $\pm$ 0.1 nm/layer was measured for the magnesium layers and 2.5 $\pm$ 0.1 nm/layer for the transition metal interlayers. The palladium layer

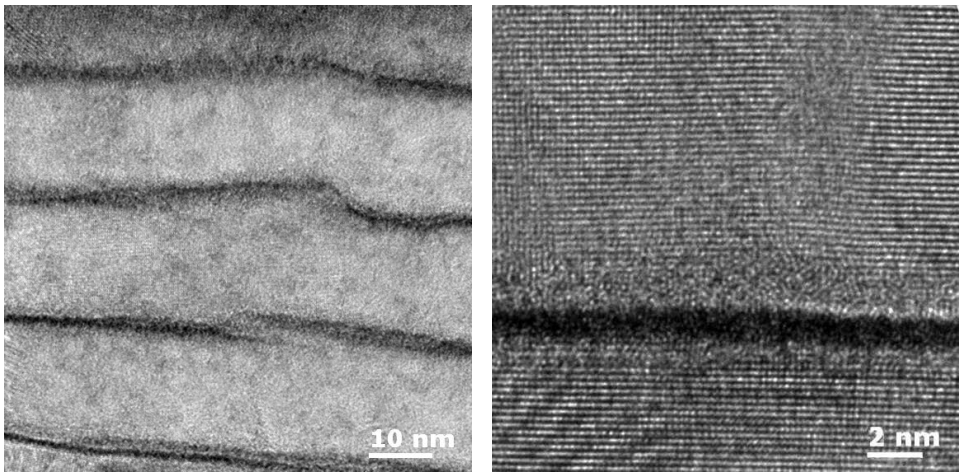

(a) (b)

Figure 4.12: Cross-sectional TEM images of a FIB-SEM lift-out of the Mg/TM thin film multilayer in its as-deposited state showing a) a high-resolution TEM image of the top 4 bi-layers and b) a high-resolution TEM image of a magnesium-transition metal interface

at the top of the sample had been coated with tungsten in the FIB TEM sample preparation process, which made measuring its thickness difficult. The thickness of the palladium layer at the bottom of the sample however was measured to be 14.4 ± 0.1 nm.

High resolution images of the Mg/TM coating such as the one shown in figure 4.12b exhibit lattice fringes in the thin film growth direction, which is perpendicular to the substrate. Using these lattice fringes a d-spacing of 2.58 ± 0.03 Å was measured, which matches the database value of 2.605 Å for the Mg(002) planes. These lattice fringes are interrupted at each magnesium-transition metal interface and, unlike for the magnesium layers, the electron signal coming from the transition metal interlayers does not provide evidence of any form of crystallinity.

Figure 4.11b show a Z-contrast, high-angle annular dark-field TEM im-

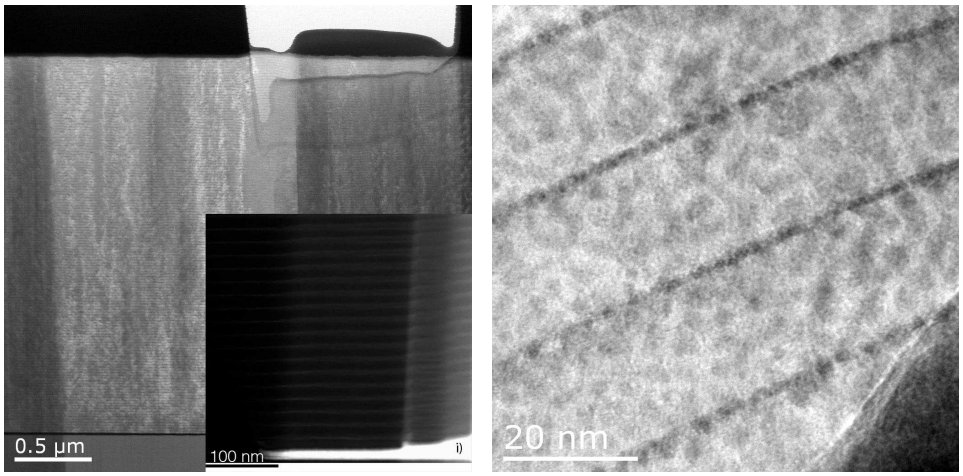

(a) (b)

Figure 4.13: Cross-sectional TEM images of a FIB-SEM lift-out of the Mg/Cr thin film multilayer in its as-deposited state showing a) a view of the entire multilayer structure on the glass substrate with i) a STEM image of the bottom 18 bi-layers and b) a high-resolution TEM image of 4 bi-layers located towards the top of the coating

age of the bottom 14 layers of the Mg/TM multilayer including the bottom capping layer of palladium. The image also highlights the area of the sample that features in the series of EDX maps shown in figure 4.15.

Similar studies were undertaken for the Mg/Cr and Mg/V thin film multilayers in their as-deposited state. Shown in figure 4.13 are TEM images showing the cross-section of the Mg/Cr coating which reveal that the coating is made up of 150 layers of magnesium with a thickness of ca. 18.0 $\pm$ 0.1 nm, separated by chromium layers with a thickness of ca. 0.8 $\pm$ 0.1 nm. Figure 4.13a shows that the Mg/Cr sample is nano-structured by uniform layers throughout the entire cross-section of the coating. This layer separation is evident throughout the entire structure, including the uppermost layers. Figure 4.13b shows layers 142-146 which show no signs of homogeni-

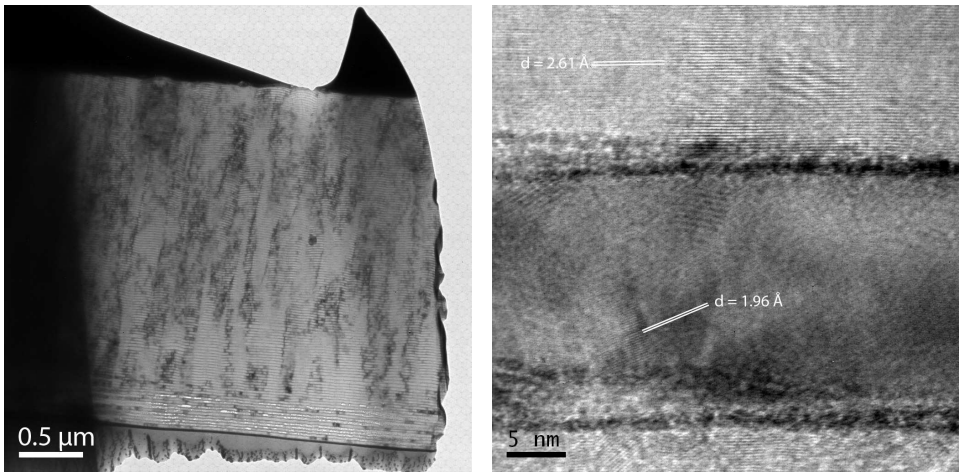

(a) (b)

Figure 4.14: Cross-sectional TEM images of a FIB-SEM lift-out of the Mg/V thin film multilayer in its as-deposited state showing a) a view of the entire multilayer structure on the glass substrate with and b) a high-resolution TEM image of 2 bi-layers from the central part of the coating

sation of the layers. The inlay in figure 4.13a shows a STEM image of a the bottom 18 bi-layers of the sample, including the bottom palladium capping layer. This region of the sample was used for EDX mapping.

Figure 4.14 shows cross-sectional TEM images of the Mg/V sample. Figure 4.14a reveals that the coating is made up of 150 layers of magnesium, with a thickness of 17.0 ± 0.1 nm, separated by layers of vanadium that are 1.2 ± 0.1 nm thick. Lattice fringes in the growth direction of the thin film, coming from the magnesium layers shown in figure 4.14b, correspond to a d-spacing of 2.61 ± 0.03 Å which matches the database value of 2.605 Å for Mg(002) planes. The image also shows lattice fringes corresponding to a d-spacing of 1.94 ± 0.03 Å which matches the database value of 1.900 Å for planes of Mg(102). The magnesium crystal structure is interrupted at the interface with the vanadium layers which show no evidence of crystallinity.

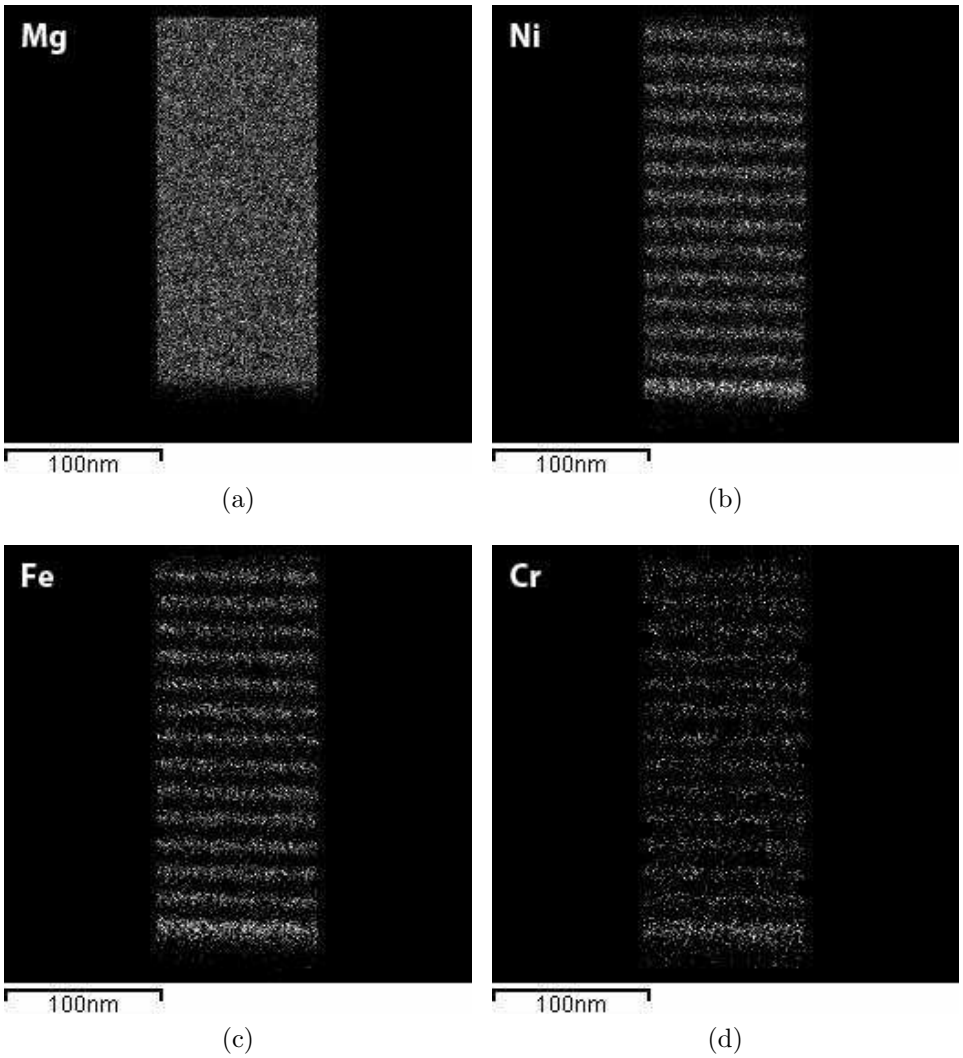

Figure 4.15: STEM EDX map of the bottom 14 bi-layers of the Mg/TM multilayer in its as-deposited state showing the EDX signal of a) magnesium, b) nickel, c) iron and d) chromium originating from the region of the sample highlighted in figure 4.11b

Figure 4.15 shows a collection of EDX maps of the Mg/TM sample area highlighted in figure 4.11b showing the non-homogeneous X-ray signal coming from the different elements in the sample. Distinct lines can be seen for the X-ray signal of nickel (figure 4.15b), iron (figure 4.15c) and chromium (figure

4.15d) corresponding to the bright lines coming from the transition metal interlayers shown in figure 4.11b.

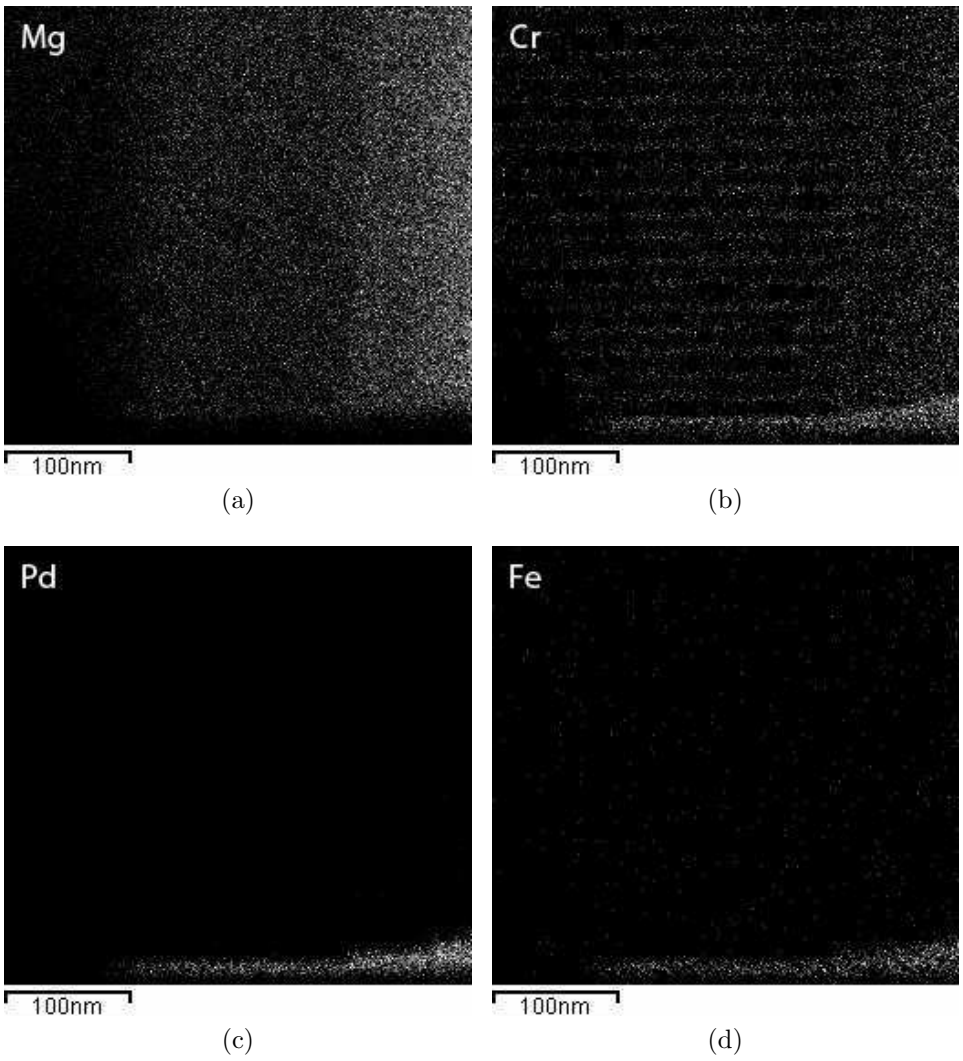

Figure 4.16: STEM EDX map of the bottom 18 bi-layers of the Mg/Cr multilayer in its as-deposited state showing the EDX signal of a) magnesium, b) chromium, c) palladium and d) iron

Figure 4.16 contains EDX maps of the Mg/Cr sample area presented in the inlay of figure 4.13a, showing the X-ray signal corresponding to the elemental magnesium, chromium, iron and palladium present in the sample.

The catalysed samples were examined by TEM, post cycling in their hydrogenated state. Figure 4.17 shows a collection of TEM images which highlight some of the structural changes the Mg/TM sample underwent during hydrogen cycling.

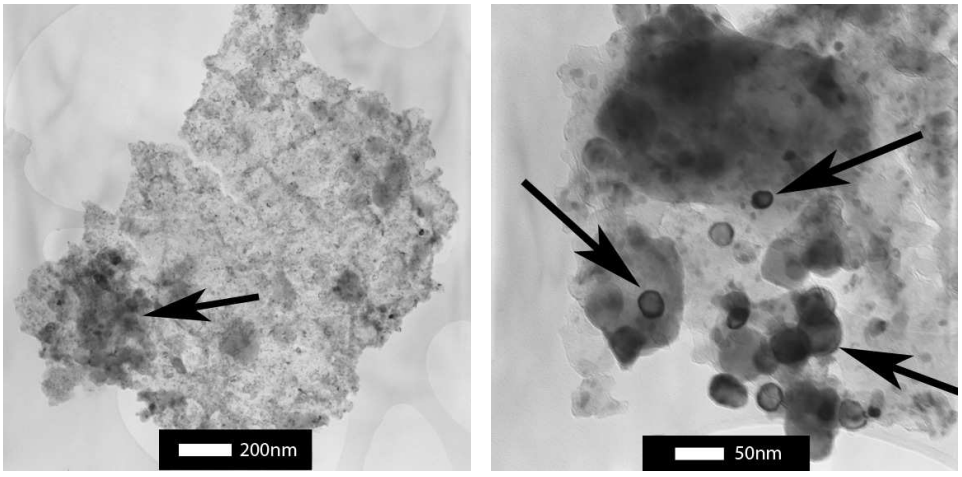

(a) (b)

Figure 4.17: TEM images showing a) an Mg/TM multilayer thin film particle in its hydrogenated state and b) a catalyst-rich region of such a particle

Figure 4.17a suggests that the Mg/TM particles exhibit a level of heterogeneity with darker regions and circular features in parts of the sample such as the one highlighted by an arrow in figure 4.17a. Figure 4.17b presents a higher resolution image of such a darker region which, like the region highlighted in figure 4.17a, contains small circular features. EDX analysis showed that the composition of these darker regions differs from the bulk of the thin film particles. Measured in the central region and the darker region of the particle shown in figure 4.17a the magnesium content drops from around 91.0 $\pm$ 0.4 at.% to 81.0 $\pm$ 0.4 at.% whilst the nickel, iron and chromium content rises. The results of the EDX study are presented in table 4.3

Element	Central Region	Dark Region
Mg	91.0 ± 0.4 at.%	81.0 ± 0.4 at.%
Ni	3.7 ± 0.1 at.%	6.9 ± 0.1 at.%
Fe	trace	8.0 ± 0.1 at.%
Cr	trace	2.6 ± 0.1 at.%
Mn	trace	trace
Pd	5.2 ± 0.1 at.%	1.5 ± 0.1 at.%

Table 4.3: EDX post cycling

EDX analysis on the area rich in small, circular features shown in figure 4.17b suggests these features are rich in iron with the magnesium content having dropped to 50.0 ± 0.3 at.% whilst the iron and chromium content were 42.8 ± 0.3 at.% and 6.1 ± 0.1 at.% respectively, with traces of nickel and palladium.

Figure 4.18 compares an electron diffraction pattern from the magnesium-rich area of the Mg/TM thin film particle shown in 4.17a with one from a particle containing iron-rich circular features as highlighted in figure 4.17b. Both patterns exhibit strong diffraction rings which were indexed to match database values for magnesium oxide. The pattern in figure 4.18b however exhibits additional diffraction spots which match database d-spacings for iron and chromium.

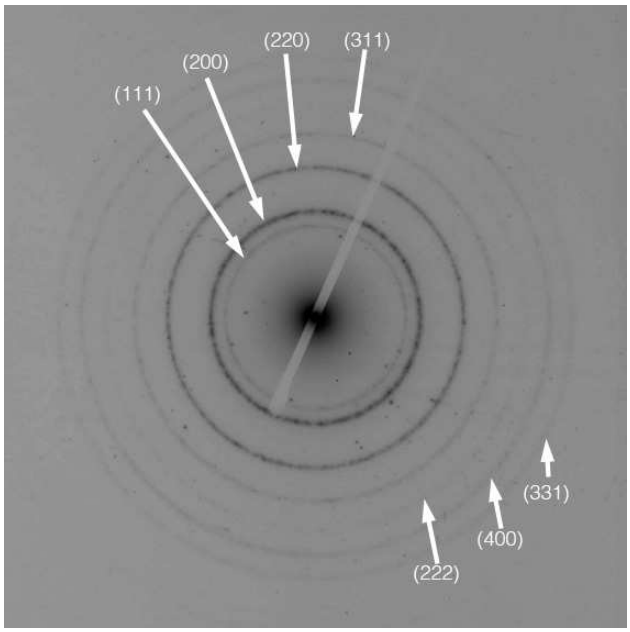

(a)

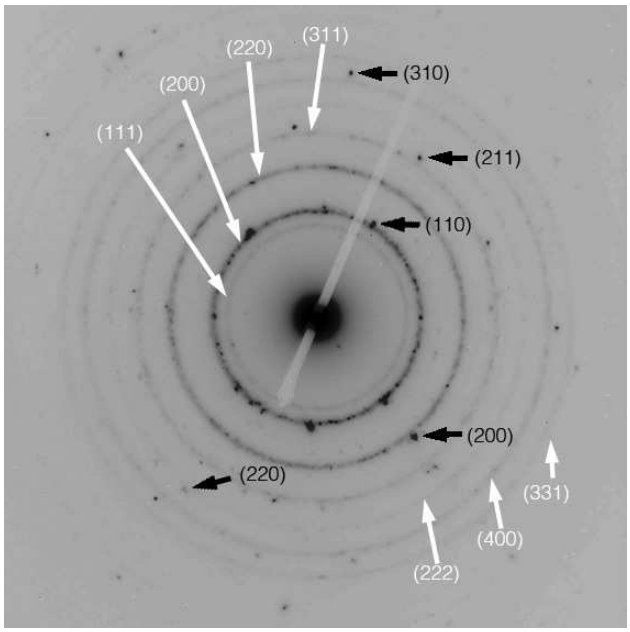

(b)

Figure 4.18: SAED images of a) a magnesium-rich area of an Mg/TM thin film particle in its hydrogenated state indexed to periclase (white arrows) and b) an iron-rich area of such a particle indexed to BCC iron (black arrows)

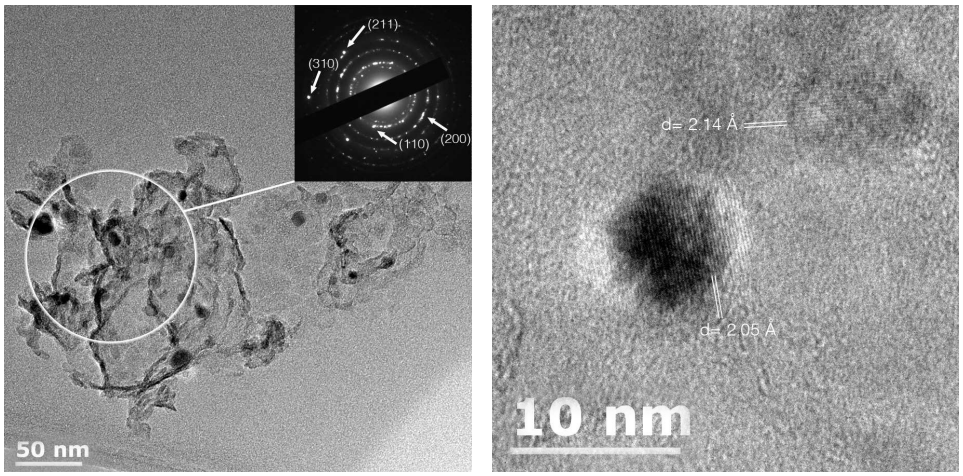

(a) (b)

Figure 4.19: Bright-field TEM images showing a) an Mg/Cr thin film particle in its hydrogenated state after 60 cycles of hydrogenation and dehydrogenation along with an SAED pattern from the area highlighted, indexed for chromium and b) lattice fringes in high-resolution TEM coming from a dark feature in the sample and the surrounding material

A representative collection of TEM images of the Mg/Cr sample in its hydrogenated state is shown in figure 4.19. Figure 4.19a highlights that the Mg/Cr sample has a heterogeneous distribution of darker features throughout the bulk of the material. Figure 4.19b shows a high-resolution TEM image of such a dark feature which exhibits lattice fringes. Using intensity profiling, the distance between these lines was measured at 2.05 ± 0.03 Å which matches the database d-spacing of BCC chromium (110) planes (d = 2.039 Å). The image also exhibits lattice fringes coming from the material surrounding the dark feature which correspond to the (200) planes of magnesium oxide (d = 2.106 Å) with a measured d-spacing of 2.14 ± 0.03 Å. The electron diffraction pattern in figure 4.19a was taken from the area highlighted in the figure. It shows clearly a series of diffraction rings that correspond to

the diffraction pattern for magnesium oxide. In addition, several spots have been identified and matched to the diffraction pattern of chromium.

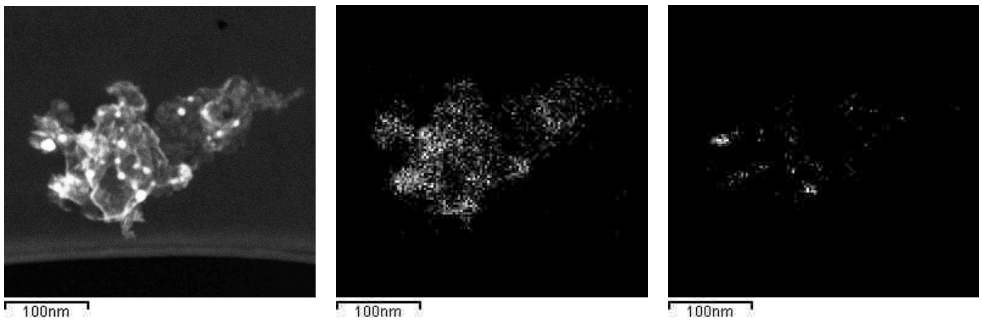

(a) (b) (c)

Figure 4.20: STEM images showing a) an HAADF image of an Mg/Cr particle in its hydrogenated state, b) an EDX map of the magnesium signal coming from the same particle and c) an EDX map of the chromium signal coming from the same particle

Scanning transmission electron microscopy was used to generate high-angle annular dark field images of the Mg/Cr sample as well as a series of EDX maps in order to produce the images in figure 4.20. The atomic contrast in figure 4.20a highlights the locations in the sample that are made up of heavier elements and the EDX maps in images 4.20b and 4.20c show that the areas of high Z-contrast correspond with the chromium EDX signal coming from the same locations in the sample.

Figure 4.21 shows a series of TEM images of the Mg/V sample in its hydrogenated state. Figure 4.21a shows that the Mg/V sample also has a heterogeneous distribution of darker features throughout the bulk of the structure. Figure 4.21b shows a high-resolution TEM image of one of these dark features with clearly visible lattice fringes. The separation of these lattice fringes was measured using intensity profiling and corresponds to a

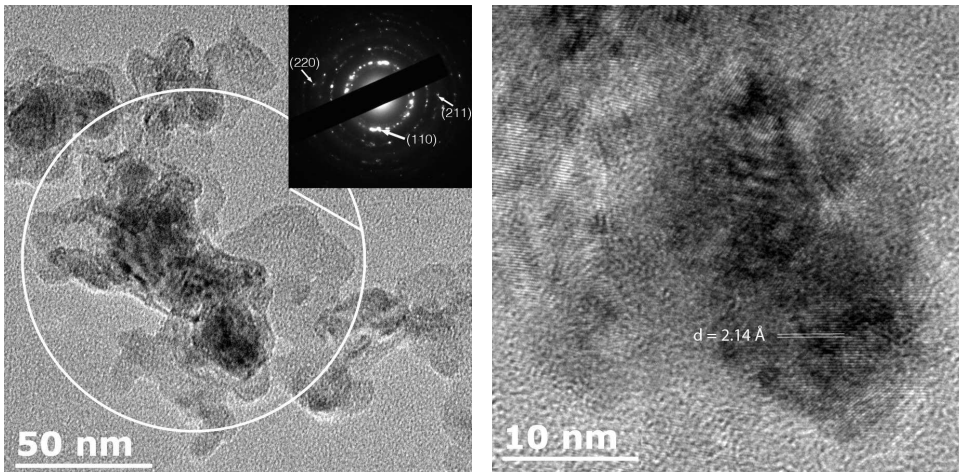

(a) (b)

Figure 4.21: Bright-field TEM images showing a) an Mg/V thin film particle in its hydrogenated state after 60 cycles of hydrogenation and dehydrogenation along with an SAED pattern from the area highlighted indexed for vanadium and b) lattice fringes in high-resolution TEM coming from the dark region of the sample

d-spacing of 2.14 ± 0.03 Å which is in agreement with database values of the d-spacing of the (110) planes of BCC vanadium (d = 2.141 Å). The SAED pattern overlaid onto figure 4.21a originated from the area highlighted in the image and shows a series of spots that correspond to database d-spacings of magnesium oxide (periclase). In addition several spots, highlighted in figure 4.21a, can be identified that match database d-spacings of BCC vanadium.

The images shown in figure 4.22, similar to those shown in figure 4.20, show high-resolution elemental composition maps for magnesium and vanadium in figures 4.22c and 4.22b which are matched to the Z-contrast image shown in figure 4.22a. These images show clearly that, what are darker features in the bright-field images in figure 4.21, appear as bright features in Z-contrast, which is indicative of heavier elements. The EDX maps then

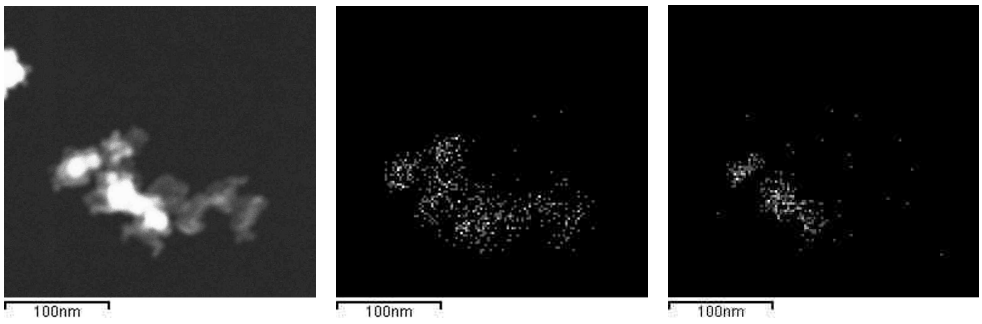

(a) (b) (c)

Figure 4.22: STEM images showing a) an HAADF image of an Mg/V particle in its hydrogenated state, b) an EDX map of the magnesium signal coming from the same particle and c) an EDX map of the vanadium signal coming from the same particle

confirm that these bright features are in fact vanadium.

4.3 Hydrogen Storage Properties of Thin Film Multilayers

4.3.1 Thermodynamics

A range of hydrogenation and dehydrogenation experiments were undertaken to understand the behaviour of the four thin film materials during their reaction with hydrogen. Pressure-composition isotherms were taken for the Mg/TM sample at temperatures between 250°C and 350°C in 20°C steps resulting in 6 isotherms, three of which are presented in figure 4.23a for clarity. The three graphs, and especially the smaller aliquot step dehydrogenation reaction at 250°C, exhibit two distinct plateaus, measured for all temperatures between cycles 10 and 20.

From the midpoints of two plateaus for the dehydrogenation reactions at

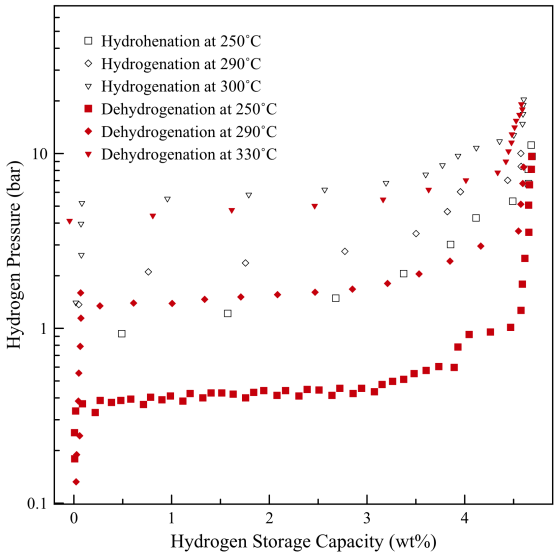

(a)

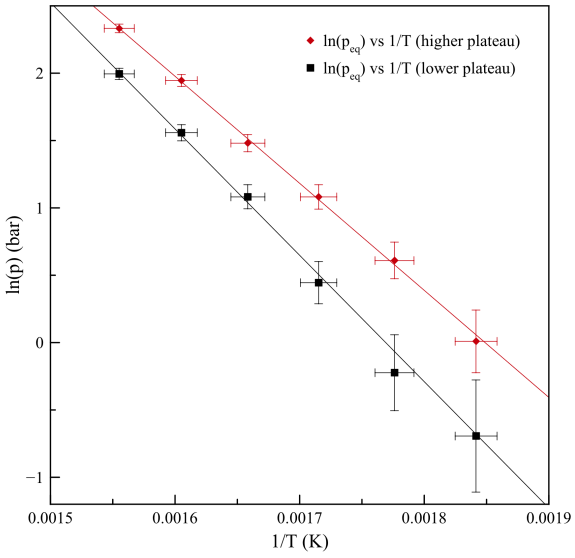

(b)

Figure 4.23: a) Pressure-composition isotherm of the Mg/TM sample at a range of different temperatures and b) the corresponding van't Hoff plots for the two dehydrogenation plateaus

the 6 different temperatures, two van't Hoff plots were produced as shown in figure 4.23b. The slope and intercept of the linear regression line for the two plots were used to calculate the enthalpies and entropies for the dehydrogenation reactions. For the lower plateau, a dehydrogenation enthalpy ΔH of $78.0 \pm 2.3\,\mathrm{kJ\,mol^{-1}\,H_2}$ and an entropy ΔS of $137.9 \pm 3.7\,\mathrm{J\,K^{-1}\,mol^{-1}\,H_2}$ were calculated, whereas for the higher plateau an enthalpy of $66.1 \pm 1.0\,\mathrm{kJ\,mol^{-1}\,H_2}$ and an entropy of $122.1 \pm 1.6\,\mathrm{J\,K^{-1}\,mol^{-1}\,H_2}$ were determined.

Figures 4.24, 4.25 and 4.26 show dehydrogenation isotherms for the Mg/Cr, Mg/V and $\mathrm{Mg}_{control}$ samples at a range of different temperatures and their corresponding van't Hoff plots. These pressure-composition isotherms exhibit plateaus with no indication of a multi-phase hydrogen storage material. The enthalpies and entropies of the dehydrogenation reactions were calculated and for the Mg/Cr sample the van't Hoff plots produced a ΔH of $73.6 \pm 0.6\,\mathrm{kJ\,mol^{-1}\,H_2}$ and ΔS of $133.7 \pm 1.0\,\mathrm{J\,K^{-1}\,mol^{-1}\,H_2}$.

For the Mg/V sample the enthalpy and entropy were calculated with a ΔH of $73.3 \pm 0.3\,\mathrm{kJ\,mol^{-1}\,H_2}$ and ΔS of $133.4 \pm 0.5\,\mathrm{J\,K^{-1}\,mol^{-1}\,H_2}$. The $\mathrm{Mg}_{control}$ sample had plateau pressures that resulted in an enthalpy and entropy ΔH of $73.9 \pm 0.6\,\mathrm{kJ\,mol^{-1}\,H_2}$ and ΔS of $134.8 \pm 0.9\,\mathrm{J\,K^{-1}\,mol^{-1}\,H_2}$.

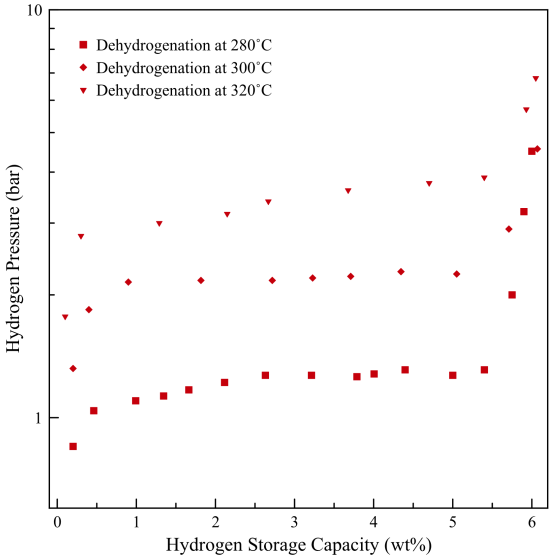

(a)

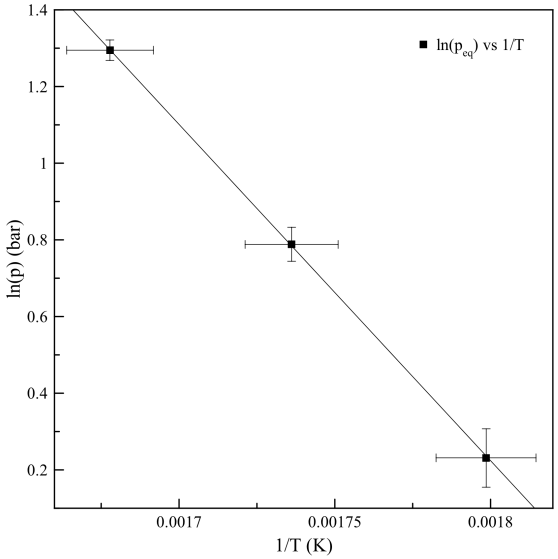

(b)

Figure 4.24: a) Pressure-composition isotherm of the Mg/Cr sample at a range of different temperatures and b) the corresponding van't Hoff plots for the dehydrogenation plateau

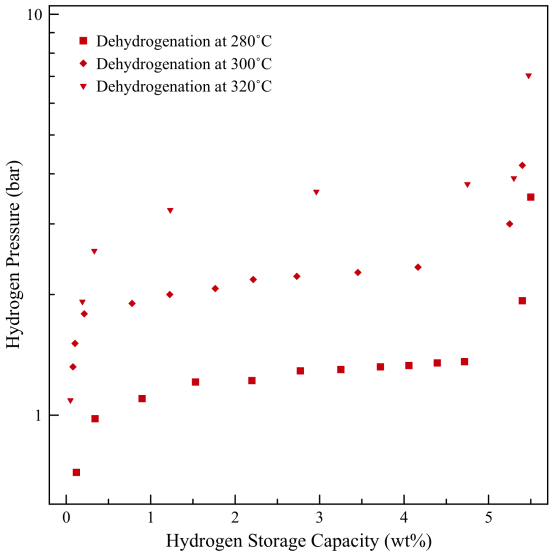

(a)

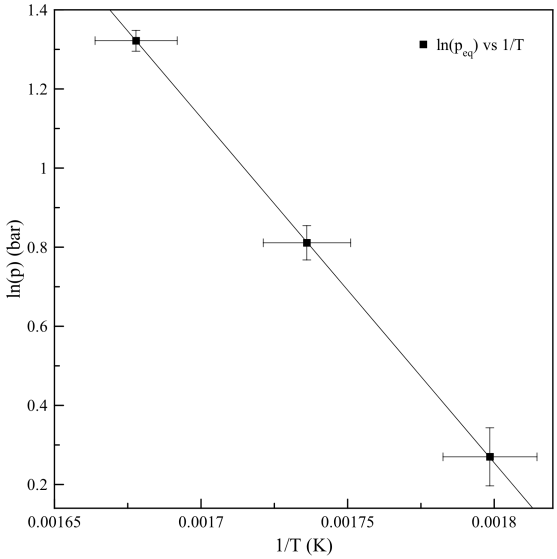

(b)

Figure 4.25: a) Pressure-composition isotherm of the Mg/V sample at a range of different temperatures and b) the corresponding van't Hoff plots for the dehydrogenation plateau

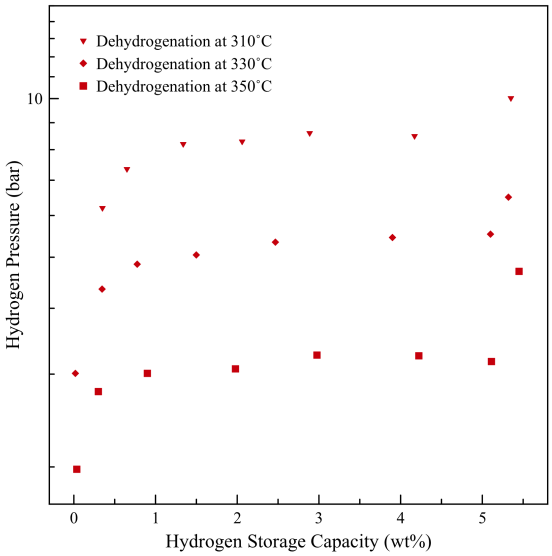

(a)

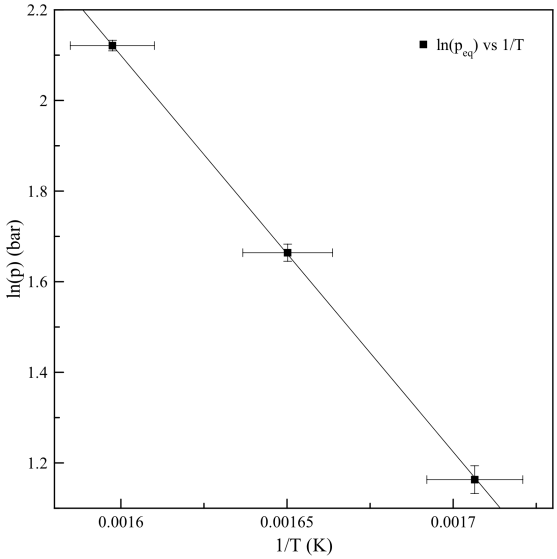

(b)

Figure 4.26: a) Pressure-composition isotherm of the $Mg_{control}$ sample at a range of different temperatures and b) the corresponding van't Hoff plots for the dehydrogenation plateau

4.3.2 Hydrogen Storage Kinetics

A number of hydrogenation experiments were done at a range of temperatures between 250°C and 350°C to investigate the fast hydrogenation kinetics of the thin film samples at different temperatures.

Sample	Temperature (°C)	Time (min)
Mg/TM	250	3.1
	270	2.5
	310	1.2
	350	0.6
Mg/Cr	250	29.0
	270	7.5
	300	3.5
	320	2.5
Mg/V	250	17.5
	270	10.4
	300	3.6
	320	2.1
$Mg_{control}$	270	36.0
	300	11.6
	320	2.2
	350	1.5

Table 4.4: Time taken to hydrogenate the 4 samples to 90% (Mg/TM) and 80% (Mg/Cr, Mg/V and $Mg_{control}$) of their maximum capacity between cycles 50 and 60

Table 4.4 compares the time taken to hydrogenate the Mg/TM sample to 90% of its maximum capacity and, due to kinetic limitations, the time taken to hydrogenate the Mg/Cr, Mg/V and $Mg_{control}$ samples to 80% of their maximum capacity at the different temperatures once the activation process described in section 4.3.4 was completed.

Similarly, a number of dehydrogenation experiments were performed on the 4 samples at a range of temperatures between 250°C and 350°C. Figures

4.27, 4.28, 4.29 and 4.30 compare the dehydrogenation kinetics of the samples at different temperatures, showing the data collected for 90% dehydrogenation of all samples, linearised using JMAK (equation 4.1) and CV (equation 4.2) kinetic models where

$$kt = [-\ln(1-\alpha)]^{1/n} \tag{4.1}$$

and

$$kt = 1 - (1-\alpha)^{1/2}. \tag{4.2}$$

From the slopes of linear regression lines for the different materials' kinetic model at different temperatures, Arrhenius plots of $\ln(k)$ vs $1/T$ were generated, linearising the Arrhenius equation

$$k = k_0 e^{-E_a/RT} \tag{4.3}$$

and allowing the calculation of the activation energy (E_a) from the gradient of the linear regression line.

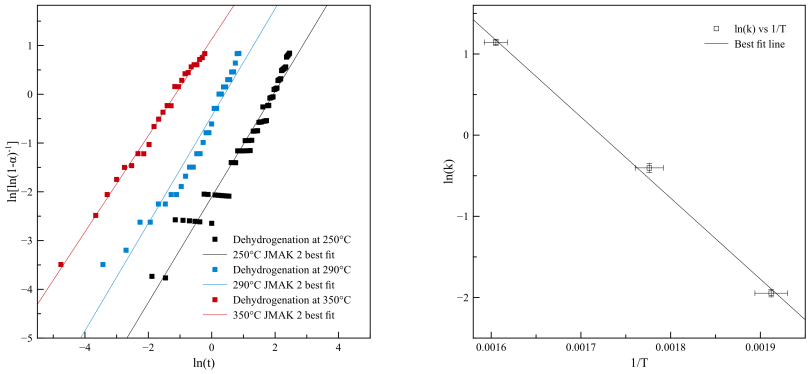

(a) (b)

Figure 4.27: a) Dehydrogenation kinetics linearised using the JMAK model of the Mg/TM thin film sample at 250°C, 290°C and 350°C and b) the corresponding Arrhenius plot

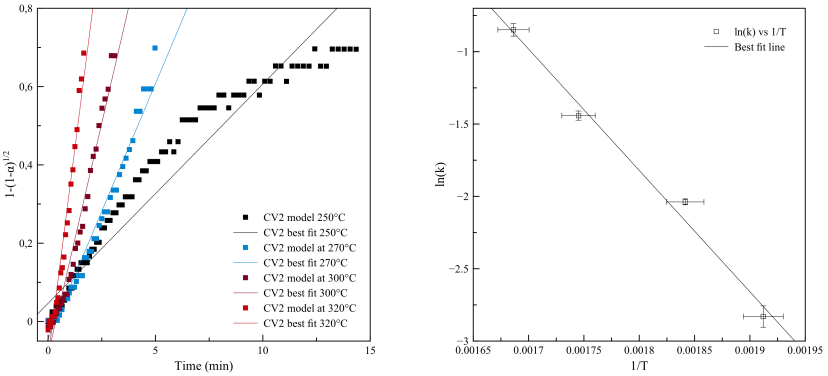

(a) (b)

Figure 4.28: a) Dehydrogenation kinetics linearised using the CV model of the Mg/Cr thin film sample at 250°C, 270°C, 300°C and 320°C and b) the corresponding Arrhenius plot

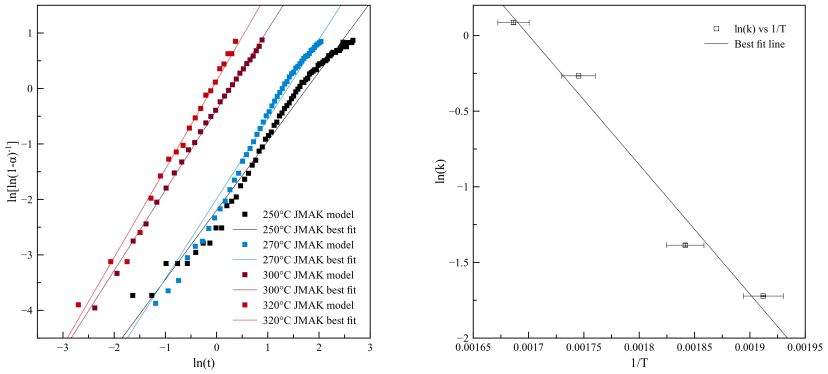

(a) (b)

Figure 4.29: a) Dehydrogenation kinetics linearised using the JMAK model of the Mg/V thin film sample at 250°C, 270°C, 300°C and 320°C and b) the corresponding Arrhenius plot

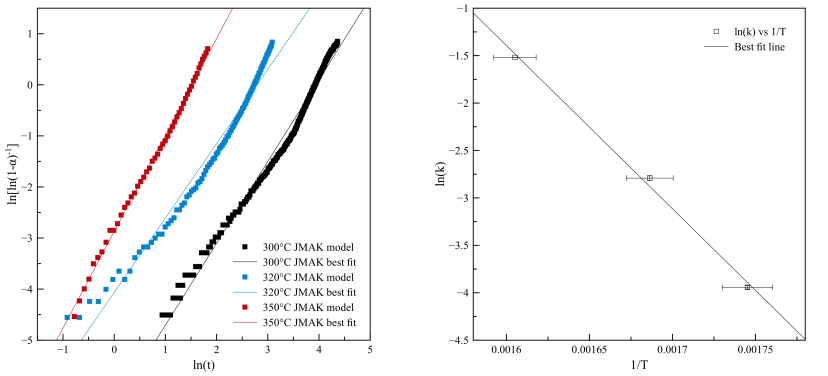

(a) (b)

Figure 4.30: a) Dehydrogenation kinetics linearised using the JMAK model of the $Mg_{control}$ thin film sample at 300°C, 320°C and 350°C and b) the corresponding Arrhenius plot

From the slope of these Arrhenius plots, shown in figures 4.27b, 4.28b, 4.29b and 4.30b, the activation energies for the dehydrogenation reactions of the 4 materials were derived, which are presented in table 4.5.

Sample	Activation Energy
Mg/TM	$80.0 \pm 4.4\,\mathrm{kJ\,mol^{-1}}$
Mg/Cr	$69.7 \pm 5.8\,\mathrm{kJ\,mol^{-1}}$
Mg/V	$71.1 \pm 5.0\,\mathrm{kJ\,mol^{-1}}$
$Mg_{control}$	$142.9 \pm 5.0\,\mathrm{kJ\,mol^{-1}}$

Table 4.5: Table showing the activation energies of the 4 multilayer samples derived, using the Arrhenius equation, from the modelled dehydrogenation rates of the samples at a range of temperatures between 250°C and 350°C

The actual times measured for the 4 samples to dehydrogenate 90% of their total capacity, at the temperatures used in the activation energy calculations, are presented in table 4.6.

Sample	Temperature (°C)	Time (min)
Mg/TM	250	12.5
	290	2.5
	350	0.6
Mg/Cr	250	13.2
	270	5.2
	300	3.0
	320	1.8
Mg/V	250	12.1
	270	8.3
	300	2.9
	320	1.7
$Mg_{control}$	300	79.0
	320	23.4
	350	6.6

Table 4.6: Time taken to dehydrogenate 90% of the 4 samples' maximum capacity between cycles 50 and 60

4.3.3 Differential Scanning Calorimetry

In order to verify the modelling data presented in section 4.3.2, a number of differential scanning calorimetry endotherms were measured. The results are presented in figures 4.31 - 4.35 for heating rates of between 2°C and 20°C min^{-1}.

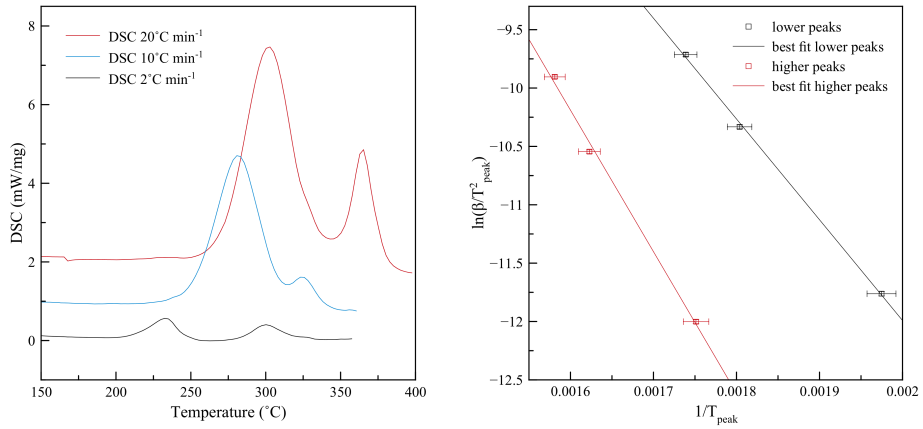

(a) (b)

Figure 4.31: a) DSC endotherms and b) the corresponding Kissinger plot for the Mg/TM sample

Shown in figure 4.31a, the DSC experiments revealed two clearly separate peaks for the Mg/TM sample at all three heating rates. In the case of the Mg/Cr (figure 4.32a) and Mg/V (figure 4.33a) samples these two peaks were identifiable, but overlapping required deconvolution using *MagicPlot* peak fitting software. The $Mg_{control}$ sample however, shown in figure 4.34a, produced only a single peak during the dehydrogenation reaction.

To avoid sintering the samples, as discussed in section 2.2.2, the maximum temperature was limited to 350°C, which meant limiting the maximum

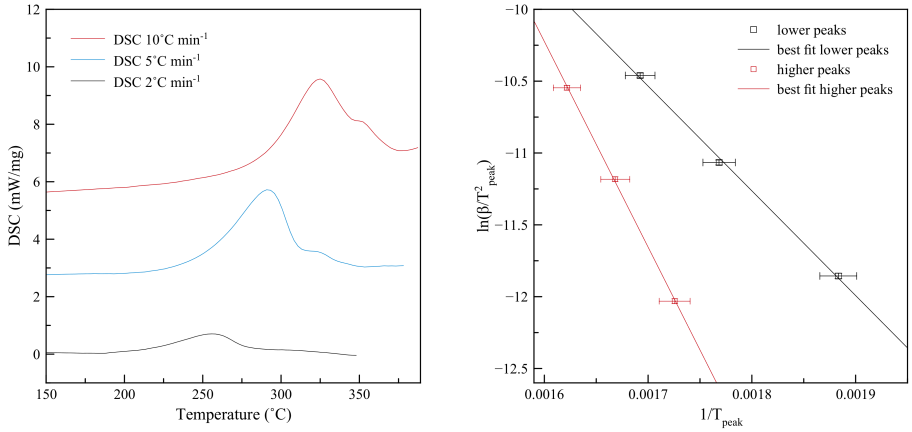

(a) (b)

Figure 4.32: a) DSC endotherms and b) the corresponding Kissinger plot for the Mg/Cr sample

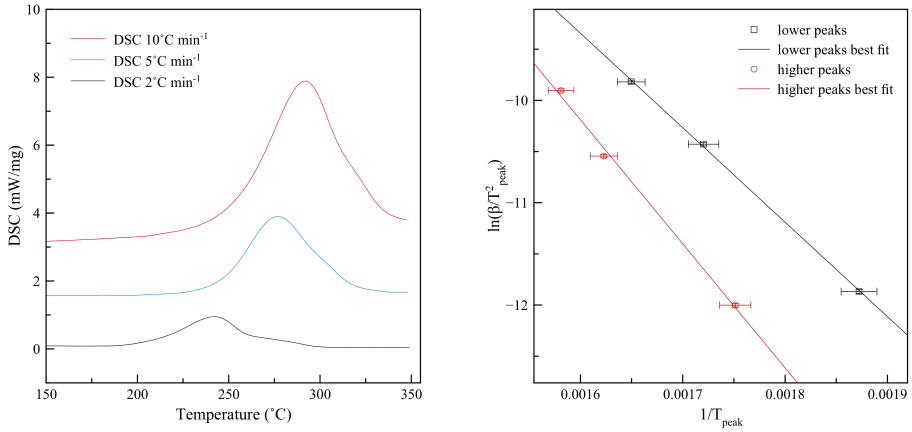

(a) (b)

Figure 4.33: a) DSC endotherms and b) the corresponding Kissinger plot for the Mg/V sample

ramp rate to 10°C min^{-1} in order provide enough time to allow full dehydrogenation at reduced temperatures. In the case of $Mg_{control}$ sample, the maximum temperature was raised to 390°C for the 10°C min^{-1} measurement

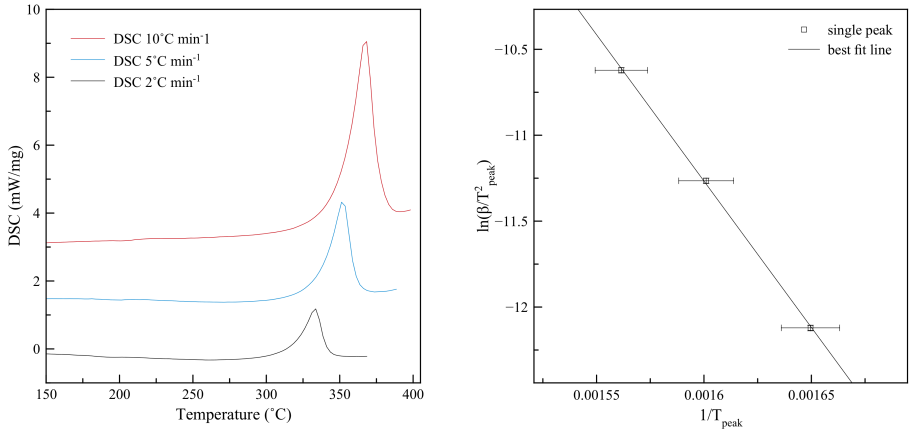

(a) (b)

Figure 4.34: a) DSC endotherms and b) the corresponding Kissinger plot for the $Mg_{control}$ sample

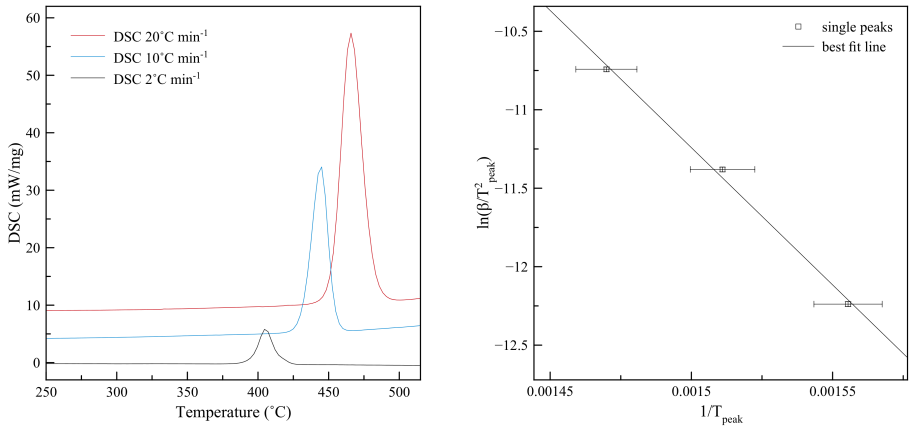

(a) (b)

Figure 4.35: a) DSC endotherms and b) the corresponding Kissinger plot for an as-received MgH_2 sample

to allow full dehydrogenation. The 5°C min^{-1} and 2°C min^{-1} measurements' maximum temperatures were also adjusted to 375°C to ensure full dehydrogenation. The peak temperatures were used for all samples at all heating

rates to plot a series of Kissinger plots of $1/T_{peak}$ against $\ln(\beta/{T_{peak}}^2)$. From the slopes of these Kissinger plots, shown in figures 4.31 - 4.34 the activation energies of the different samples' dehydrogenation reactions were calculated as discussed in section 5.8. For comparison to a known standard, DSC measurements were also taken for an as-received MgH_2 sample (Alfa Aesar, 98% MgH_2), plotted together with its corresponding Kissinger curve in figure 4.35. Tabulated in figure 4.7 are the activation energies of the dehydrogenation reactions of all 4 samples as derived from the DSC experiments.

	Activation Energy	
Sample	Lower Temperature Peak	Higher Temperature Peak
MgTM	$71.6 \pm 1.8\,\mathrm{kJ\,mol^{-1}}$	$92.9 \pm 6.8\,\mathrm{kJ\,mol^{-1}}$
Mg/Cr	$60.6 \pm 2.5\,\mathrm{kJ\,mol^{-1}}$	$119.0 \pm 2.5\,\mathrm{kJ\,mol^{-1}}$
Mg/V	$65.9 \pm 1.1\,\mathrm{kJ\,mol^{-1}}$	$80.8 \pm 2.0\,\mathrm{kJ\,mol^{-1}}$
$Mg_{control}$	$141.6 \pm 3.2\,\mathrm{kJ\,mol^{-1}}$	N/A
MgH_2	$147.7 \pm 6.0\,\mathrm{kJ\,mol^{-1}}$	N/A

Table 4.7: Table showing the activation energies of the dehydrogenation reactions of the 4 thin film samples and as-received magnesium hydride

4.3.4 Kinetic Evolution

Data between the 50^{th} and 60^{th} cycles were used to measure the hydrogenation and dehydrogenation times and to model the dehydrogenation kinetics to ensure the hydrogenation and dehydrogenation kinetics had stabilised, allowing repeatable and consistent measurements. Figures 4.36 to 4.39 highlight the activation process the 4 samples underwent during the first 50 cycles that each sample was subjected to. A general increase in hydrogenation kinetics is observed during the first few cycles, followed by stability throughout the rest of the cycles in each case.

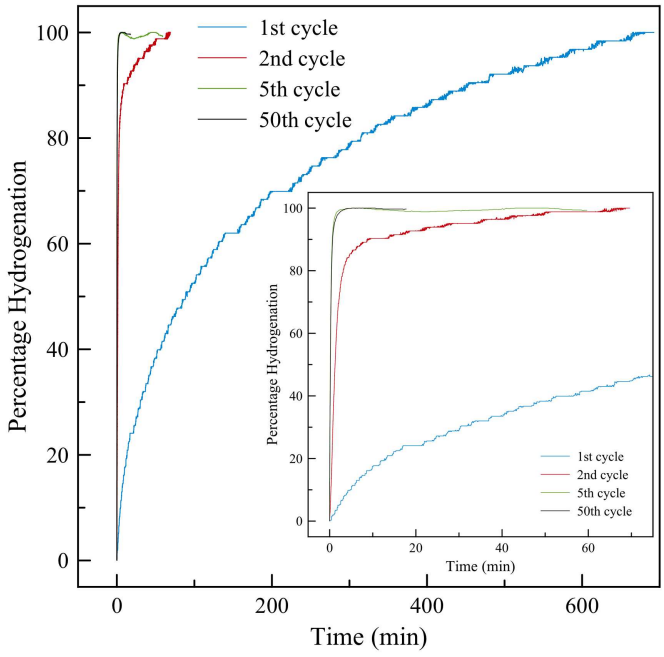

Figure 4.36: Activation and kinetic evolution of the hydrogenation of the Mg/TM sample with an inset showing the same graph on a shorter time scale

Figure 4.36 shows the Mg/TM sample fully hydrogenates to a maximum

reversible capacity of 4.6 ± 0.2 wt% at 350°C in the first cycle, followed by a significant increase in hydrogenation kinetics in the following cycles. From the 5th cycle onwards, the hydrogenation kinetics remain unchanged.

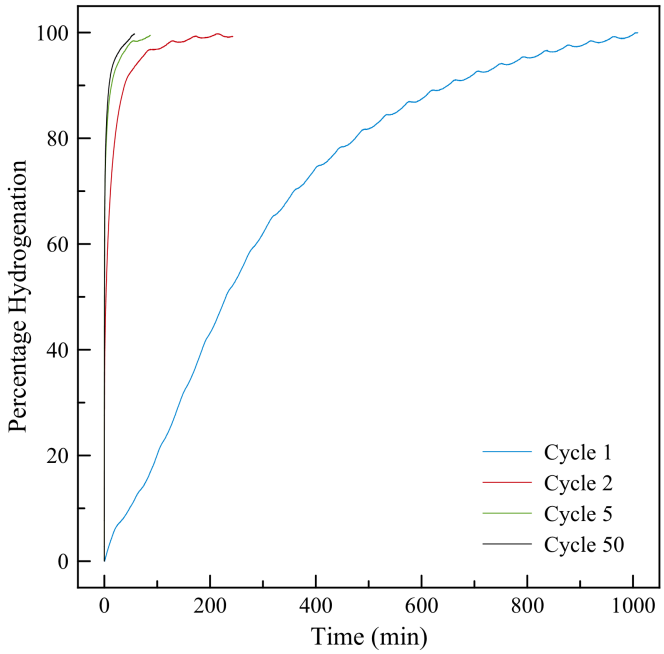

Figure 4.37: Activation and kinetic evolution of the hydrogenation of the Mg/Cr sample

The Mg/Cr and Mg/V samples were activated at 320°C and figures 4.37 and 4.38 show how the kinetics evolve during activation of the materials. In both cases the initial hydrogenation to a full reversible capacity of 6.1 ± 0.3 wt% for the Mg/Cr sample and 5.4 ± 0.3 wt% for the Mg/V sample takes more than 10 hours, followed by a significant increase in hydrogenation kinetics for the second cycle. From the fifth cycle onwards, the hydrogenation kinetics of both materials remain constant.

Figure 4.39 highlights the activation process of the $Mg_{control}$ sample at

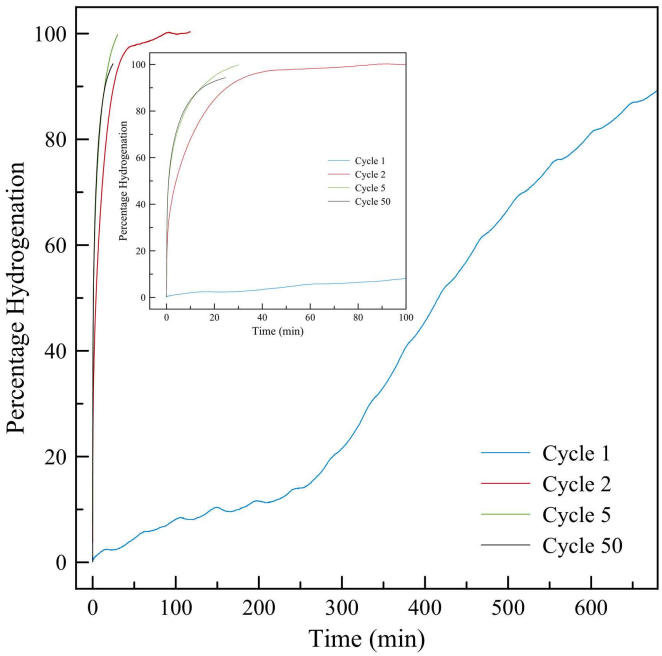

Figure 4.38: Activation and kinetic evolution of the hydrogenation of the Mg/V sample with an inset showing the same graph on a shorter time scale

350°C. The first hydrogenation cycle plateaued at around 10% of the maximum capacity of the sample which was measured at 5.4 ± 0.2 wt%. In the second cycle the material absorbed 40% of its maximum capacity and from the third cycle the material reached its full measured capacity of 5.4 ± 0.2 wt%. This was followed by a slow increase in hydrogenation kinetics until about cycle 20 (shown in figure 4.39), after which the hydrogenation kinetics remained unchanged.

The evolution of the dehydrogenation kinetics of the 4 thin film samples is presented in figures 4.40 and 4.41, and shows the change in the dehydrogenation kinetics of the samples during the first 50 hydrogenation and dehydrogenation cycles that the materials were subjected to. Illustrated in

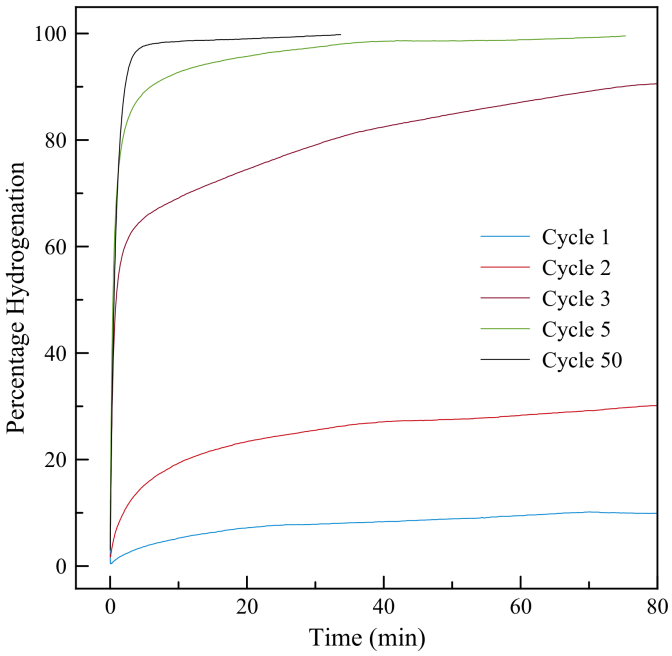

Figure 4.39: Activation and kinetic evolution of the hydrogenation of the $Mg_{control}$ sample

figure 4.40a, the Mg/TM sample shows an initial increase in dehydrogenation during the first 5 cycles, followed by stable dehydrogenation kinetics throughout the tested lifetime of the material at 350°C.

The Mg/Cr and Mg/V samples were activated at 320°C and, as shown in figures 4.40b and 4.41a, exhibit no change in the kinetics during the first 5 cycles. In both cases there is a small but measurable slowing of dehydrogenation at the 50^{th} cycle compared with the first 5 cycles of around 1 minute for dehydrogenation of 90% of the reversible capacity. The evolution of the dehydrogenation kinetics of the $Mg_{control}$ sample, studied at 350°C, is shown in figure 4.41b. The first dehydrogenation cycle following the very small uptake in the first hydrogenation cycle is characterised by a very slow release of

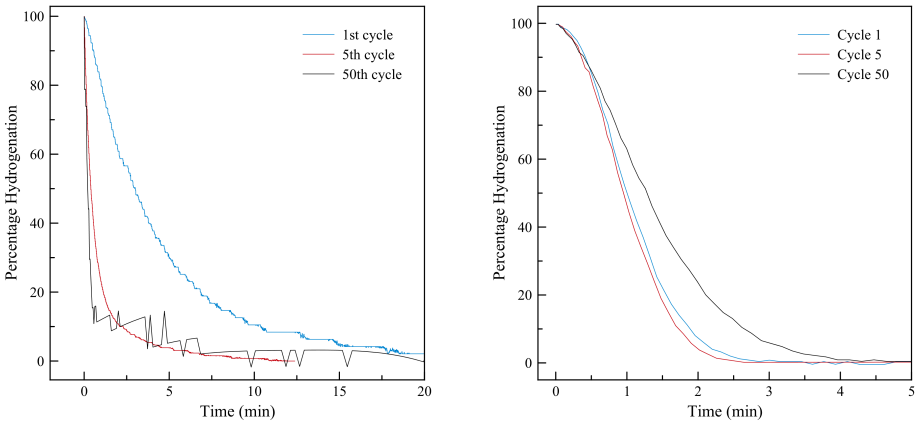

(a) (b)

Figure 4.40: Activation and kinetic evolution of the dehydrogenation of a) the Mg/TM and b) the Mg/Cr samples

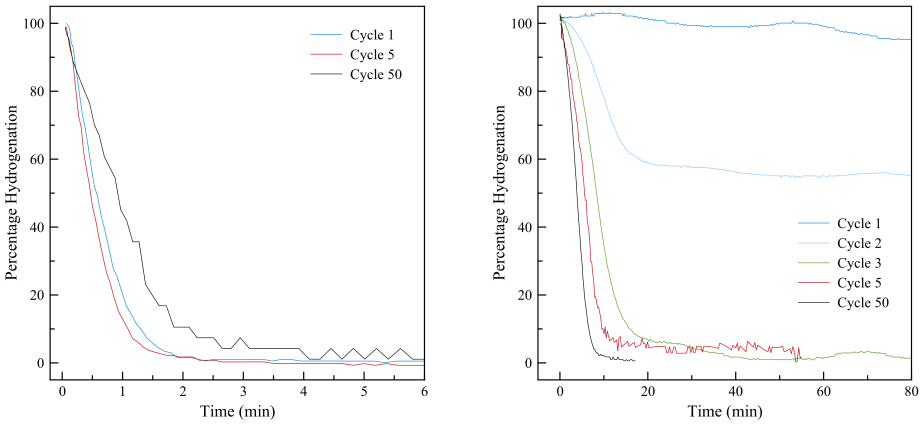

(a) (b)

Figure 4.41: Activation and kinetic evolution of the dehydrogenation of a) the Mg/V and b) the $Mg_{control}$ samples

hydrogen. The second cycle exhibits much faster dehydrogenation kinetics followed by even faster kinetics in the third cycle which dehydrogenates the full 5.4 wt%. Shown also are cycles 5 and 50 which suggest an increase in

dehydrogenation kinetics throughout the tested lifetime of the material of around 3 minutes for dehydrogenation of 90% of the reversible capacity.

4.3.5 Thermogravimetric Analysis

Controlled heating of all 4 samples at 10°C min^{-1} during thermogravimetric analysis (TGA) to 400°C for the catalysed samples and 500°C for the $Mg_{control}$ sample provided a second, independent measurement of the hydrogen storage capacity of the thin film materials. Figures 4.42 and 4.43 show TGA traces of the 4 materials together with the DSC data of the materials, both at 10°C min^{-1}. The Mg/TM sample releases 4.2 ± 0.1 wt% of hydrogen between 240°C and 340°C, overlapping both DSC peaks, indicative of a full dehydrogenation. A graph showing the TGA and DSC data is shown in figure 4.42a.

The Mg/Cr sample releases 5.7 ± 0.1 wt% of hydrogen between ca. 270°C and 370°C, overlapping the matching DSC endotherm taken at the same heating rate of 10°C min^{-1} as shown in figure 4.43a. Figure 4.43a highlights the TGA and DSC data for the Mg/V sample at a 10°C min^{-1} heating rate showing a hydrogen release of 5.2 ± 0.1 wt% from the sample between ca. 260°C and 340°C. The $Mg_{control}$ sample releases 5.1 ± 0.1wt% of hydrogen between ca. 310°C and 390°C at a heating rate of 10°C min^{-1} which corresponds to the DSC endotherm for the same heating rate as shown in figure 4.43b.

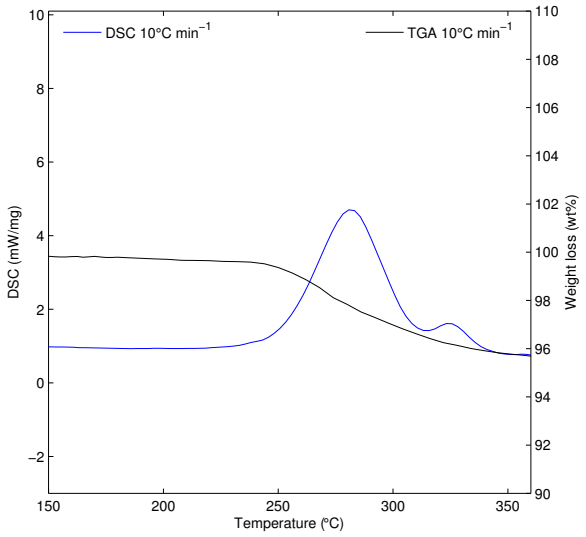

(a)

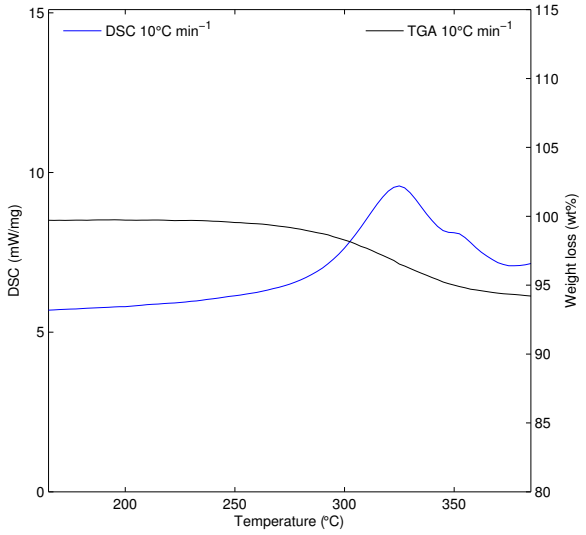

(b)

Figure 4.42: Graphs illustrating the weight loss due to dehydrogenation upon heating at 10°C min^{-1} overlaid onto the DSC traces at the same heating rates of a) the Mg/TM sample and b) the Mg/Cr sample

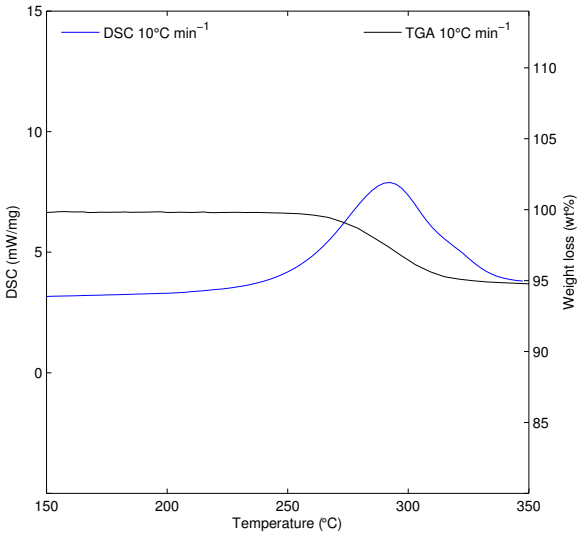

(a)

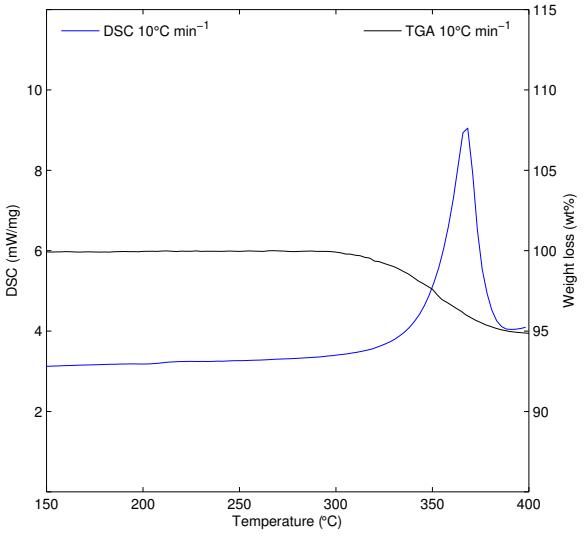

(b)

Figure 4.43: Graphs illustrating the weight loss due to dehydrogenation upon heating at 10°C min^{-1} overlaid onto the DSC traces at the same heating rates of a) the Mg/V sample and b) the $Mg_{control}$ sample

4.3.6 Cycling Behaviour

Presented in figure 4.44 is a graph illustrating the cycling behaviour of the Mg/TM sample. The measurements were taken initially on the manual Sievert's type apparatus described in section 3.4.1 (cycles 1-19) and the sample was then transferred to the PCTpro2000 described in section 3.4.1.

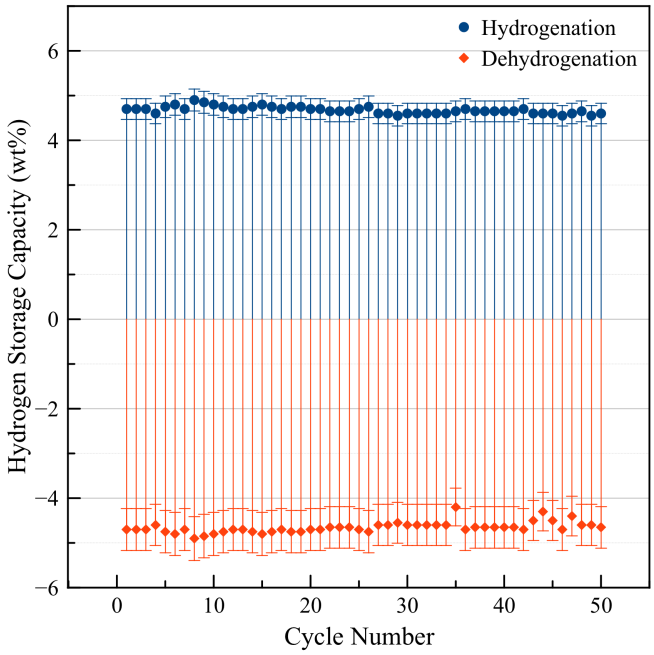

Figure 4.44: Cycling behaviour over 50 cycles of hydrogenation and dehydrogenation of the Mg/TM sample

The graph suggests a constant capacity of about 4.6 ± 0.2 wt%, within experimental errors. There is also a good match between the two instruments' measurements of hydrogen storage capacity, with both the lab-built Sievert's and the PCTpro2000 measuring 4.6 ± 0.2 wt% in cycles 19 and 20 respectively.

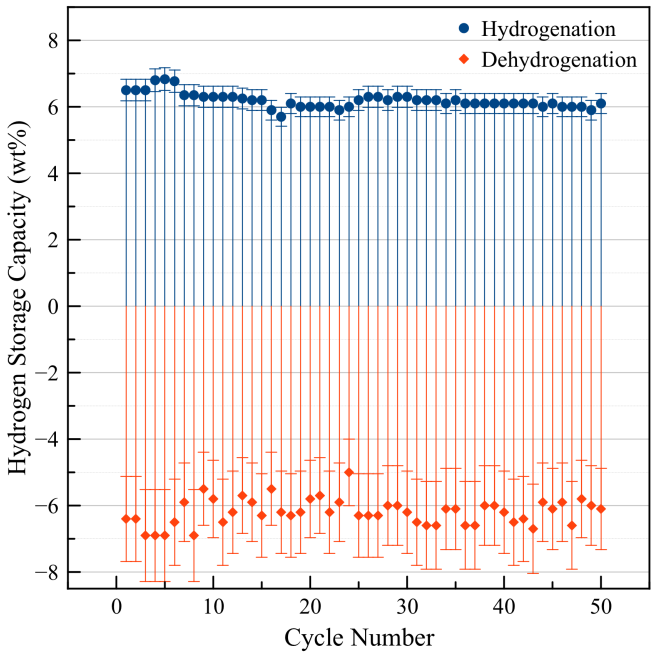

Figure 4.45: Cycling behaviour over 50 cycles of hydrogenation and dehydrogenation of the Mg/Cr sample

The Mg/Cr, Mg/V and $Mg_{control}$ samples were activated and cycled on the PCTpro2000 at various temperatures between 250°C and 320°C in the case of the Mg/Cr and Mg/V samples and between 270°C and 350°C in the case of the $Mg_{control}$ sample, and the results of the cycle life studies are presented in figures 4.45, 4.46 and 4.47. Figure 4.45 shows that the Mg/Cr sample maintains a constant capacity of around 6.1 ± 0.3 wt%.

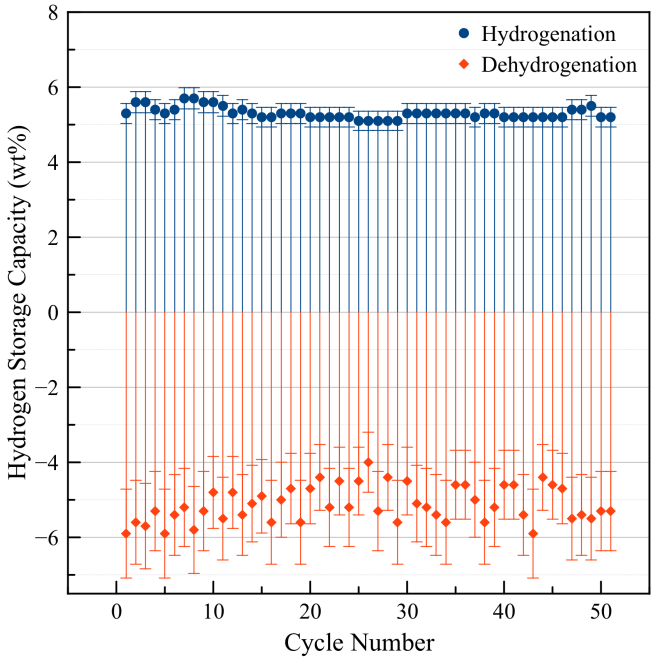

Figure 4.46: Cycling behaviour over 50 cycles of hydrogenation and dehydrogenation of the Mg/V sample

The capacity of the Mg/V sample does not change throughout the first 50 cycles remaining within experimental error of 5.4 ± 0.3 wt%, as shown in figure 4.46.

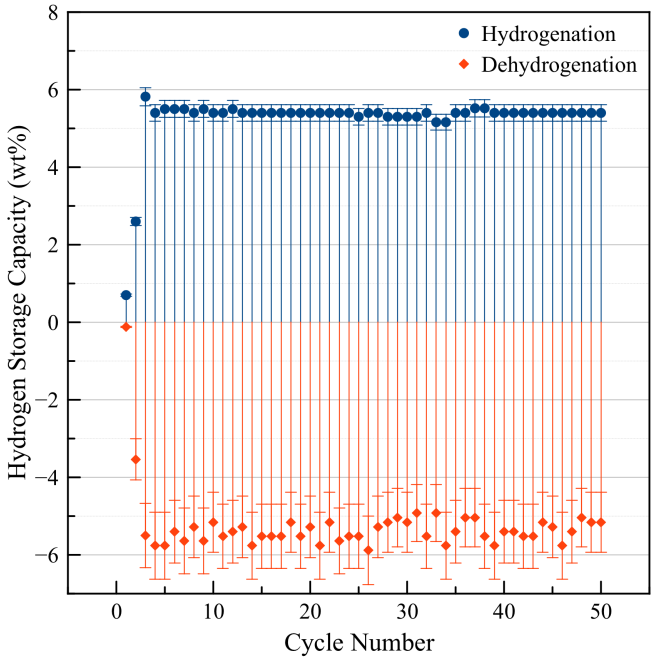

Figure 4.47: Cycling behaviour over 50 cycles of hydrogenation and dehydrogenation of the $Mg_{control}$ sample

Similarly, figure 4.47 shows that the $Mg_{control}$ sample's capacity remains constant at 5.4 ± 0.2 wt% throughout the first 50 cycles.

Chapter 5

Discussion

5.1 Introduction

Section 2.1.2 shows that a good way of achieving favourable operating conditions for a magnesium-based hydrogen storage system is by catalysing the reaction. This improves the reaction kinetics, allowing fast and reversible hydrogen storage at temperatures closer to the temperature at which magnesium hydride releases 1 bar of hydrogen (T_{1bar}), as opposed to the 400°C required for uncatalysed magnesium hydride (Zaluska and Zaluski, 1999).

The following sections will review the evidence presented in chapter 4 with a view to explain and understand how the materials' composition and structure evolved during hydrogen cycling and how the structure and evolution affects the hydrogen storage properties that are of concern for hydrogen storage applications in order to meet the objectives set out in chapter 1.

Section 5.2 discusses the results of the XRD studies undertaken on the thin film samples both in their as-deposited and hydrogenated state. The results of the electron microscopy analysis of the samples are then discussed in sections 5.3 and 5.4 before sections 5.5 and 5.6 discuss the results of the

hydrogen cycling experiments that were carried out on the thin film samples. Sections 5.7, 5.8 and 5.9 then draw together and further analyse the structural evolution and hydrogen storage properties of the samples in order to understand the effect of and relationship between the process employed, the materials used and the structural evolution and hydrogen storage properties of these thin film materials.

5.2 X-Ray Diffraction

Section 4.2 presents results on the microstructural properties of the thin film samples and their microstructural evolution caused by hydrogen cycling at elevated temperatures. With the exception of the palladium capping layers of the Mg/TM sample, and after careful calibration, all 4 samples were produced using the same coating conditions changing only the power on the different magnetrons to adjust the ratio between magnesium and transition metal sputtering rates in order to achieve the desired compositions. As detailed in section 3.2.1, the Mg/TM capping layers were sputtered from a palladium target mounted directly on a suitably-sized (57 mm) magnetron, as opposed to co-sputtered from a stainless steel 316L target (175 × 380 mm) as was the case for the capping layers of the Mg/Cr, Mg/V and $Mg_{control}$ samples due to the configuration of the Teer Coatings UDP650 PVD coating unit. This is reflected in the X-ray diffraction patterns of the as-deposited thin film sample shown in figure 4.2. The diffraction patterns for the Mg/TM, Mg/Cr, Mg/V and $Mg_{control}$ samples are very similar in that they all exhibit a single, intense and broad peak around 34.5° 2θ, corresponding to the (002) planes of HCP magnesium. A second peak at around 72.7° 2θ is visible on

all 4 patterns coming from the Mg(004) planes. The locked-coupled set-up of the scans makes them sensitive to those planes of atoms that are parallel to the surface of the substrate, indicating a strong directionality in the thin film samples where the (002) planes of atoms are parallel to the surface of the substrate following columnar crystal growth during deposition in the <001> direction.

For the Mg/TM sample this was further confirmed by the unlocked-coupled scans that are shown in figure 4.2. As explained in section 3.3.1, with the sample effectively tilted by the inter-planar angle between the Mg(002) and Mg(104), Mg(114), Mg(105) and Pd(311) planes, these same planes were observed in the diffraction pattern which confirms the crystal structure as well as the strong orientation and direction of crystal growth in the Mg/TM thin film. This directional growth of the magnesium phase is also widely supported in the literature Higuchi *et al.* (1999), Yamamoto *et al.* (2002), Blawert *et al.* (2008) and Qu *et al.* (2009b) showing only reflections from the Mg(002) and Mg(004) planes of HCP magnesium crystallites in their XRD patterns.

In addition, the scans show broad humps corresponding to diffraction from the Pd(111) planes at around 40° 2θ. These peaks are very similar in the Mg/Cr, Mg/V and $Mg_{control}$ scans and in all three cases there is a small shift of these peaks to higher angles of 2θ of ca. 0.6° 2θ. The Pd (111) peak from the palladium phase in the Mg/TM sample's diffraction pattern has a higher intensity relative to the same peak in the other three samples and in addition there is a second palladium peak at around 86.4° 2θ coming from the Pd(222) planes. The lower intensity and shift in the Pd(111) position,

as well as the lack of a detectable Pd(222) peak in the Mg/Cr, Mg/V and $Mg_{control}$ samples might be a result of co-sputtering the palladium capping layers from the stainless steel 316L target as described in section 3.2. If a small amount of stainless steel was co-sputtered with the palladium, despite the high relative sputtering yield ratio of palladium and stainless steel 316L (ca. 2.1:1) and the shutter arrangement employed to reduce the amount of steel contamination to a minimum, then, looking at iron-palladium (Ghosh *et al.*, 1999), nickel-palladium (Ghosh *et al.*, 1999) and chromium-palladium (Ghosh and Olson, 2000) phase diagrams, it is conceivable that one or more of the elements present in the steel has formed a solid solution with the palladium, which, given the smaller atomic radius of iron (126 pm), nickel (124 pm) and chromium (128 pm) compared with palladium (137 pm), would cause the peak to shift to higher values of 2θ.

The intensity of the magnesium peaks is very similar for the Mg/TM, Mg/Cr and Mg/V samples. In comparison, the $Mg_{control}$ sample has more intense peaks coming from the magnesium phase, relative not only to the scans of the other thin films but also to the intensity of the Pd(111) peaks. Twice as intense as the Mg(002) peaks measured for the Mg/TM, Mg/Cr and Mg/V samples, this is caused by the larger crystallites in the $Mg_{control}$ thin film, estimated using the *Scherrer* equation (equation 3.2) at around 50 nm as opposed to the 16 – 17 nm estimated for the catalysed samples, causing a lower degree of peak broadening in the diffracted beam. This suggests that the insertion of a thin layer of transition metal between layers of magnesium limits the grain size of the magnesium phase to the thickness of the layers.

In none of the scans performed on the as-deposited thin films was there

any evidence of a crystalline transition metal phase. Given the composition of the thin films (table 4.1), which are known to contain transition metal, this could be a result of the low concentration of transition metal in the thin films, the thickness of the transition metal layers and the associated peak broadening due to the small crystallite size in the growth direction and therefore detectable orientation, and the absence of a crystalline transition metal phase.

After hydrogen cycling, the shiny, metallic-looking flakes that the delamination of the thin films from their substrates produced had disintegrated into flaky, grey powders. The XRD traces of these powders shown in figures 4.3 – 4.6 show similar trends of highly complex diffraction patterns containing sharp peaks as well as broad ones. This sharpening of the diffraction peaks, corresponding to a 10-fold increase in grain size from < 20 nm to > 100 nm for the magnesium(-hydride) phase has been widely reported in the literature. Dal Toè *et al.* (2004) report an increase in grain size from 5 to 120 nm during activation at 350°C for magnesium hydride ball milled with 1 wt% graphite whilst Huhn *et al.* (2005) witness an increase from 11 to 200 nm for their Nb_2O_5-catalysed magnesium hydride sample at temperatures above 300°C. Similarly, Pelletier *et al.* (2001) report an increase from 9 to 30 nm for the magnesium hydride phase during dehydrogenation of their niobium-catalysed sample, followed by an increase to 57 nm for the magnesium phase at up to 310°C.

Apart from the transformation of the magnesium phase observed in the XRD patterns of the as-deposited samples to magnesium hydride, all four samples showed evidence of alloying of the palladium capping layers with

some of the magnesium in the form of Mg_6Pd, despite, in the case of the Mg/TM, Mg/Cr and Mg/V samples, the deposition of a double-thickness transition metal layer between the magnesium layers and the palladium caps. This was evident from the disappearance of the reflections corresponding to palladium and the presence of reflections from the $Mg_6Pd(422)$, $Mg_6Pd(820)$, $Mg_6Pd(822)$ and $Mg_6Pd(664)$ reflections at 21.68, 36.87, 37.96 and 42.23° 2θ. Based on the evidence presented in section 2.2.4, this might be expected as the hydrides of iron, chromium and vanadium have much higher dehydrogenation enthalpies of -10 $kJ\,mol^{-1}\,H_2$ (Tan *et al.*, 2009), 4 $kJ\,mol^{-1}\,H_2$ (Zahiri *et al.*, 2010) and 40.1 $kJ\,mol^{-1}\,H_2$ (US DOE, 2013) and will therefore be in a metallic state at equilibrium conditions for magnesium hydride. This is in agreement with the findings Tan *et al.* (2009) make where metallic interlayers allow magnesium-palladium inter-diffusion and alloy formation, discussed in section 2.2.4.

The emergence of new, crystalline transition metal phases was also observed in the catalysed samples after hydrogen cycling. In the XRD pattern of the Mg/TM sample (figure 4.3) there is evidence of a crystalline phase of FCC Mg_2NiH_4 in the form of broad peaks for reflections from $Mg_2NiH_4(111)$, $Mg_2NiH_4(200)$, $Mg_2NiH_4(311)$ and $Mg_2NiH_4(400)$ at 23.61, 27.34, 46.14 and 56.41° 2θ, but visible especially at around 39° 2θ with a peak corresponding to reflections from $Mg_2NiH_4(220)$, as well as a crystalline phase of BCC iron, also represented by very broad peaks. The main reflection from the Fe(110) planes at 44.71° 2θ was sufficiently strong and unaffected by neighbouring peaks to derive an estimate of the average grain size of the iron phase in the material at around 50 nm. Together with the average grain size calcu-

lated for the magnesium hydride phase (ca. 85 nm), this then leads to the suggestion that the Mg/TM thin film underwent a transformation whereby the amorphous nickel-rich transition metal interlayers disintegrated, with the nickel diffusing into the magnesium phase. Mg_2Ni and Mg_2NiH_4 were then formed, depending on the state of hydrogenation, whilst the iron formed BCC nano-crystallites. The magnesium layers were allowed to hydrogenate and de-hydrogenate repeatedly, whilst undergoing grain growth during cycling between HCP magnesium and rutile, β-phase magnesium hydride at elevated temperatures.

Very similar observations can be made for the Mg/Cr and Mg/V samples. In the hydrogenated state both samples produce strong diffraction lines for β-phase magnesium hydride, which are significantly sharper than those of the thin films' magnesium phases in their as-deposited state. This sharpening is more pronounced than in the case of the Mg/TM sample and, as a result of the scans being of better quality, due to more of the sample being scanned, there are more, less convoluted peaks for magnesium hydride that enabled the quantification of the peak broadening using *Williamson-Hall* plots, as presented in section 4.2.1. The results show that, despite the lower temperatures at which the Mg/Cr and Mg/V samples were cycled, with a maximum temperature of 320°C as opposed to the 350°C at which the Mg/TM sample was cycled, there was a larger increase in average crystallite size at ca. 136 nm and ca. 100 nm for the Mg/Cr and Mg/V samples respectively. Strain broadening was measured at only 0.04% for both samples, which supports the approximation used to estimate the crystallite size of the Mg/TM sample which did not account for strain broadening. It needs to be noted that this

method of estimating grain size from peak broadening loses accuracy very fast for crystallites larger than 100 nm, putting these results at the outer limit of what can be measured reliably using peak broadening (Klug and Alexander, 1974).

For the Mg/Cr sample, the chromium peak at 44.4° 2θ however was very broad at ca. 0.56° 2θ and, using the *Scherrer* equation (equation 3.2), an average crystallite size of around 20 nm was calculated. This indicates that, as with the Mg/TM sample, the possibly amorphous layers of chromium interspersed between the magnesium layers formed nano-crystals during hydrogen cycling of the sample at elevated temperatures.

The vanadium diffraction lines in the Mg/V sample's XRD pattern are too convoluted with the neighbouring Mg_6Pd, magnesium and periclase peaks to extract any information about the crystallite size of the vanadium phase. However, the presence of a large, broad, hump between the magnesium hydride peak at 39.8° 2θ and the periclase peak at 43° 2θ, not present in the Mg/Cr and $Mg_{control}$ samples' XRD patterns suggests there might be a nano crystalline phase of vanadium present in the Mg/V sample after hydrogen cycling.

The $Mg_{control}$ sample was produced to separate the effects the coating process and material handling have on the properties of the thin film samples studied to better understand the effect the transition metal catalysts have on the hydrogen storage behaviour of the thin film multilayers. The $Mg_{control}$ sample's XRD pattern, after hydrogen cycling at up to 350°C, exhibits very similar features to those of the Mg/TM, Mg/Cr and Mg/V samples' diffraction patterns. The diffraction lines for the magnesium hydride phase in the

$Mg_{control}$ sample are very sharp, which puts the grain size well outside the range suitable for peak broadening analysis. The sample does however also produce diffraction lines corresponding to the database pattern of Mg_6Pd similar to the other three samples. Other than the magnesium oxide peaks, this is the only main difference detectable when comparing the $Mg_{control}$ sample's XRD pattern with that of as-received magnesium hydride, as shown in figure 4.6.

The detected levels of grain growth in the magnesium phase above and beyond 100 nm after hydrogen cycling at elevated temperatures match those reported in the literature. Although some authors claim to observe no grain growth in ball-milled magnesium hydride at temperatures as high as 450°C (Zaluska and Zaluski, 1999), others have reported grain growth increasing with temperature, with grain sizes of around 100 nm for magnetron-sputtered magnesium thin films annealed at 300°C (Qu *et al.*, 2009a), which compares to grain growth from 32 nm to 422 nm for a ball milled magnesium hydride powder (Paik *et al.*, 2010). The thin films reported in this work are consistent within themselves but also with these results in terms of crystallite size.

5.3 Scanning Electron Microscopy

In order to better understand the structural changes the materials underwent during hydrogen cycling, a series of SEM images are shown in section 4.2.2 which highlight the morphological change from a thin film (figure 4.7) to a (flaky) powder (figures 4.8 – 4.10) that all 4 samples underwent.

The SEM images of the hydrogenated samples reveal that the powders are made up of particles with sizes ranging from sub-micron, evident from the TEM study on the hydrogenated powders, to millimetre size. As exemplified in figures 4.8 to 4.10, the particles all have in common the fact that they have retained a large width-to-thickness ratio, where the thickness is consistently significantly smaller than the width and height, resulting in the flat, flake-like appearance of the powder particles. Figure 4.8c shows one of the thinnest particles found in the Mg/TM sample which appears to have a degree of transparency towards electrons making the smallest particles in the powders suitable for TEM analysis. Noteworthy is the comparison with the backscattered electron image of the same particle in figure 4.8b, which enhances the contrast between the bulk of the material and a series of bright, circular features (indicating the presence of heavier elements) that are uniformly distributed throughout the bulk of the specimen. Given the composition of the sample, this suggests fine particles of higher atomic number catalyst material distributed in or on the bulk of the lower atomic number magnesium particles. Figures 4.8d and 4.9b show an Mg/TM and an Mg/V thin film hydride flake respectively. These illustrate not only the thickness of larger flakes of thin film hydride, thicker than the original thin films in their as-deposited

states, but also the porous nature of these thin film flakes, suggesting they might be an agglomeration of much smaller particles.

The $Mg_{control}$ sample is of slightly different appearance than the catalysed samples. Even though the sample disintegrated into porous flakes, in a similar manner to the catalysed samples, the $Mg_{control}$ hydride particles appear to have a smoother surface and less of a plate-like structure. The principal difference between the $Mg_{control}$ sample and the catalysed samples is the absence of transition metal in magnesium structure. It is likely then that the formation of nano-crystalline transition metal phases, as observed for the Mg/TM, Mg/Cr and Mg/V samples, caused some disintegration of the thin film structure along the layer interfaces, resulting in the plate-like morphology observed in figure 4.9c and the very thin flakes shown in figure 4.8c.

Coupled with the transformation of the interlayers from amorphous to (nano-)crystalline, discussed in section 5.2 and, in the case of the Mg/TM sample, the formation of a new, intermetallic Mg_2Ni phase, is the volume expansion and contraction upon hydrogenation and dehydrogenation of the magnesium layers. This expansion, which has been reported at over 30% (Kalisvaart *et al.*, 2011; Singh *et al.*, 2007), might also play a part in the decrepitation process, transforming the dense, thin film materials to porous, flaky powders. This decrepitation has been observed for co-sputtered materials (Tan *et al.*, 2009) as well as multilayered materials (Kalisvaart *et al.*, 2011). The morphological changes observed in the latter are said to have been caused by repeated expansion and contraction of the magnesium layers during hydrogen cycling whilst the former is merely observed.

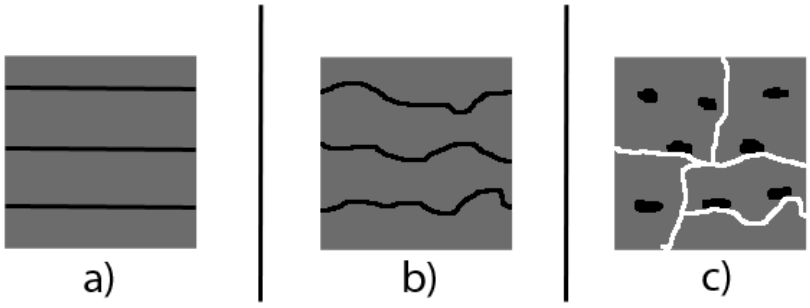

Figure 5.1: Schematic showing the suggested mechanism of the thin films' transformation and breakup with a) the as-deposited coating, b) deformed by hydrogen cycling and c) the transition metal layers forming nano-crystallites leading to the breaking up of the samples into a flaky powder

Figure 5.1 shows a schematic of the suggested mechanism where the as-deposited structure is first distorted by hydrogen cycling followed by the formation of nano-crystallites which leads to decrepitation of the thin film structure along some of the magnesium-transition metal interfaces. The volume expansion, recrystallisation and grain growth of the magnesium phase results in further decrepitation of the thin film flakes, breaking them up into smaller particles.

The EDX analysis shown in tables 4.1 and 4.2 compares the composition of the 4 samples, both in their as-deposited and their hydrogenated state. While the as-deposited Mg/TM sample has a total content of about 87.7 at.% magnesium, this is 96.3 at.% and 94.0 at.% for the Mg/Cr and Mg/V samples and 99.4 at.% for the $Mg_{control}$ sample. These values were measured with the electron beam penetrating the sample through the top, palladium-coated surface of the thin films. For comparison purposes, table 4.2 shows the 4 samples' elemental composition post cycling, as measured via EDX on several thin film particles. Comparing the as-deposited and hydrogenated samples,

there is a maximum variation of 1.2 at.% in the magnesium content measured for the Mg/Cr sample, as well a variation in the transition metal content, measured at 1 at.%. There seems to be no pattern to this variation, which suggests the hydrogenated powders are not perfectly homogeneous.

The as-deposited samples are all very similar in appearance as mirror finish, metallic looking coatings on glass substrates when observed optically. The electron images of their cross-sections in figure 4.7 show that they are all of uniform thickness and appear fully dense. There is some variation in thickness of the 4 coatings, which might to some extent be expected given the different compositions and sputtering conditions that were employed to achieve these compositions. Noteworthy is the reduced thickness of the Mg/V sample over that of the Mg/Cr sample, both of which were sputtered under the same conditions. The interlayer content of 5.2 at.% in the Mg/V sample as opposed to 3.3 at.% in the Mg/Cr sample was achieved by retaining the sputtering conditions on the magnesium target, whilst increasing the power on the vanadium target. An unused magnesium sputtering target was used in making the Mg/Cr coating, as opposed to a part-worn target in the case of the Mg/V sample, which might have caused the < 1 nm reduction in thickness of each magnesium layer that would make up the 140 nm difference between the two coatings. It is conceivable that the changing angle of the target surface due to the erosion of the target material in the race track area leads to an increased number of collisions within the sputter flux. This would result in a less directional flux with increased scattering and thus a decreased sputter rate, similar to the effect of gas pressure on the sputter rate, as detailed in section 2.2.1.

5.4 Transmission Electron Microscopy

The TEM study on the Mg/TM multilayer in its as-deposited state reveals that the sample is in fact what the set-up of the coating process aimed to make — a micron-sized, nanostructured thin film multilayer of magnesium layers interspersed with thin layers of a nickel-rich transition metal mix. The hypothesis that the average crystallite size of the Mg(002) planes of atoms in the Mg/TM sample (estimated at ca. 16 nm using the *Scherrer* equation (equation 3.2)) might be representative of the magnesium layer thickness in the thin film structure, was proven to be within 0.5 nm of the true magnesium layer thickness, which was measured at 16.5 nm by high-resolution TEM. Together with the measured 2.5 nm for the interlayer region, shown in figure 4.12b, 150 bi-layers of 16.5 + 2.5 nm equates to 2.85 μm, which is in good agreement with the total thin film thickness of 2.84 $\pm$ 0.1 μm measured using SEM.

Since the crystallite size calculated from the peak broadening of the magnesium peaks using the *Scherrer* equation (equation 3.2) corresponds well to the thickness of the magnesium layers in the thin film as measured by TEM on the cross-section of the sample, it can be concluded that there is only a very small amount of micro-strain contributing to the peak broadening of the diffraction lines in the as-deposited sample. Similarly, a thickness of 14.4 nm was measured for the palladium capping layer by TEM, which matches well with the value established from the peak broadening of the palladium peaks in the XRD study of the as-deposited thin film, determined at 14 $\pm$ 2 nm.

The magnesium layers shown in figure 4.12b exhibit strong lattice fringes

corresponding to the Mg(002) planes of atoms, as indicated by the measured d-spacing of ca. 2.58 Å. This confirms the directionality and direction of the thin film growth that was seen in the XRD measurement for the Mg/TM coating as well as the other three coatings shown in figure 4.2. This matches with the diffraction pattern shown in 4.11a which exhibits a number of spots coming from the Mg(002) and Mg(101) planes of atoms, showing no evidence however for any level of crystallinity in the transition metal layers.

Further supporting the argument that the interlayers are in fact made up of an amorphous transition metal mix is the fact that in the transition metal layer, shown in figure 4.12b, there is an absence of lattice fringes. The figure clearly shows how the transition metal layer, deposited onto a magnesium crystal, interrupts the crystal structure of the magnesium layer, forming an amorphous interlayer of transition metal upon which the next layer of magnesium crystals can form. The fact that these interlayers appear to have no detectable level of crystallinity explains why they do not result in any diffraction lines in the XRD pattern of the Mg/TM sample in its as-deposited state.

The image however also hints at the potential growth mechanism behind the magnesium thin film growth. Figure 5.2 shows that the lattice fringes from the Mg(002) planes of atoms are not seen until ca. 2 nm into the magnesium layer in its growth direction. It can be seen that there are islands of amorphous-looking magnesium (highlighted with an arrow) in-between the orderly magnesium crystals. These crystals themselves may have been formed from islands of magnesium that were clustered on the transition metal layer, whilst the space in-between the growing crystals was filled with a few atomic

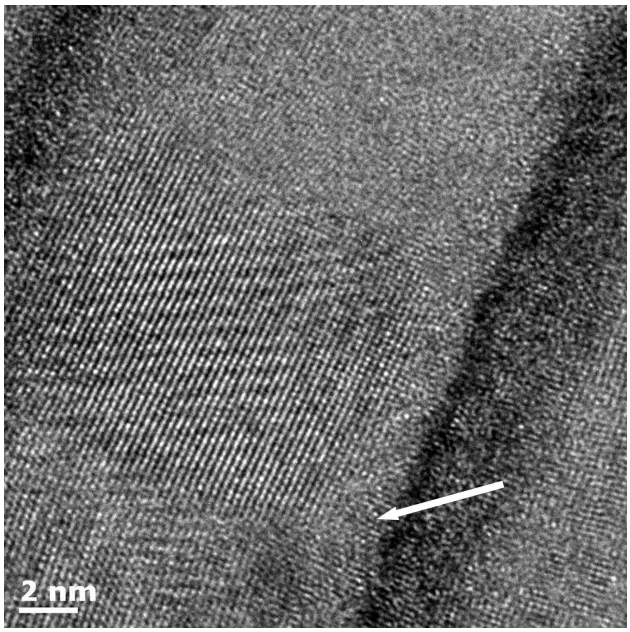

Figure 5.2: High-resolution TEM image of the magnesium-transition metal interface showing evidence of the prominent thin film growth mechanism

layers of amorphous magnesium. About 3 nm into the layer, the growing crystals would then meet and continue to grow side-by side into columnar structures such as those observed widely in the literature (Higuchi *et al.*, 2002; Singh *et al.*, 2007; Siviero *et al.*, 2009). The Stransky and Krastanov model of thin film formation, discussed by Sree Harsha (2005, chap. 9), describes thin film growth as an initial layer-by-layer deposition of a finite number of layers of atoms, followed by the formation of discrete nuclei and three-dimensional growth of the thin film. This theory matches well with the observations that were made in high-resolution TEM, which suggests that this is the dominant growth mechanism behind the magnesium layer growth.

Both the Mg/Cr and Mg/V samples are very similar in appearance to the Mg/TM sample in cross-sectional TEM. Once again it can be seen that

the samples are made up of 150 distinct layers of magnesium separated by layers of chromium and vanadium.

Due to a fault with the FIB instrument used to prepare the Mg/Cr TEM sample, the sample was left with high levels of amorphisation due to the ion beam milling process which did not allow high-resolution imaging. For the Mg/V sample however, a distinct discontinuity in crystal structure can be seen in the high-resolution TEM image shown in figure 4.14b. Magnesium crystal growth in the <001> direction, as shown by the strong lattice fringes coming from the (002) planes of HCP magnesium, appears to be followed by an interruption in the crystal structure by an amorphous layer of vanadium. This in turn is followed by renewed nucleation and growth of new magnesium crystallites, as described for the Mg/TM sample. This suggests that even for vanadium layers as thin as 1.2 nm, an interruption of the magnesium crystal growth and crystal structure occurs and renewed nucleation has to take place before crystalline layers of magnesium may grow again.

This structural separation of the magnesium layers contradicts results reported for similar structures in the literature by Baldi *et al.* (2010). They report a level of structural coherence across several multilayers of magnesium and titanium, as well as a degree of homogenisation in the uppermost 6 layers of their thin film. This consisted of only 20 multilayers of magnesium separated by interlayers of titanium. Figures 4.12a and 4.13b show clearly that there is no homogenisation in the top 4 layers of the Mg/TM multilayer, nor in the top 8 layers of the Mg/Cr coating. This might be explained by the similar, HCP crystal structure and lattice spacing of both Mg(002) and Ti(002) at 2.605 Å and 2.341 Å respectively which is not present for the BCC

transition metal elements used in this work.

From the elemental separation of the multilayers, shown in figure 4.15, it is clearly visible that the transition metal is heterogeneously distributed throughout the Mg/TM multilayer structure in separate interlayers. The thickness of the interlayers, at around 2.5 nm, is very close to the STEM beam's spot size of 1 nm, which causes blurring of the EDX signal. In addition, any buckling of the sample through its thickness or a slight misalignment would angle the plane of the layer interfaces towards the electron beam which, together with the limited resolution, explains why no layer separation of the magnesium layers can be observed by EDX. The brighter bottom line in the EDX signal, coming from the transition metal elements shown in figures 4.15a to 4.15d, shows that the bottom layer has a higher concentration of transition metal than the layers that follow. This may be due to the double-thickness layer of transition metal that was deposited, in an attempt to provide separation of the palladium capping layer and the magnesium in the thin film in order to prevent alloying between the two, described in section 3.2.1.

Similar results were found for the Mg/Cr sample which shows a non-homogeneous distribution of chromium throughout the coating in the form of distinct layers.

The palladium capping layers of the Mg/Cr, Mg/V and $Mg_{control}$ samples produced a broad, low intensity XRD peak at ca. 0.6° 2θ above the diffraction angle that can be expected from database Pd(111) diffraction patterns. The EDX maps in figures 4.16d and 4.16c show that, as well as a palladium signal, there is an X-ray signal characteristic of iron coming from the

palladium-cap layer region at the thin film-glass interface of the Mg/Cr thin film cross-section which is much stronger than the underlying iron-signal in the noise that can be seen in the bulk of the Mg/Cr sample. This suggests a degree of iron contamination in the palladium capping layers, which supports the argument made in section 5.2 that co-sputtering of steel from the 316L backing plate, on which the palladium target was mounted, has caused substitution of iron into palladium, resulting in a shift of the palladium peaks in the XRD patterns of the Mg/Cr, Mg/V and $Mg_{control}$ samples, each of which were capped with co-sputtered palladium.

The TEM images of the hydrogenated samples in section 4.2.2 help understand better the microstructural changes the samples underwent during hydrogen cycling. There is a distinct similarity between the SEM images of very small Mg/TM samples, as shown in figure 4.8, and the TEM images of the same sample, shown in figure 4.17. The backscattered-electron SEM image in figure 4.8b reveals a very thin Mg/TM multilayer flake, which in parts has a degree of transparency towards the electron beam, similar to the particles shown in the TEM images in figure 4.17. The TEM images exhibit a number of dark, circular features, which were shown to produce an EDX signal characteristic for iron, as well as diffraction spots corresponding to the d-spacing of BCC iron. These dark, circular features can be seen in the SEM image in figure 4.8b where they appear as bright, circular features due to iron having a higher atomic number than magnesium.

The three catalysed samples all exhibit these nano-sized transition metal features. Dark, circular features similar to those in the Mg/TM sample shown in figure 4.17b can be seen both in the Mg/Cr sample, highlighted in figure

4.19, and the Mg/V sample, shown in figure 4.21. The XRD patterns of the hydrogenated powders presented in section 4.2.1, showing broad transition metal peaks, indicate that these are crystalline. Selected area electron diffraction patterns (SAED) of all three catalysed samples are shown in figures 4.18, 4.19a and 4.21a, exhibiting spots corresponding to the d-spacings of their respective transition metal catalysts. Diffraction patterns taken from areas with a low concentration of these dark transition metal features lack these diffraction spots and exhibit only diffraction patterns coming from the magnesium oxide phase that is present in all three samples. For example, the pattern in figure 4.18a shows very clear diffraction rings coming from a magnesium rich region of the Mg/TM particle, such as the one shown in figure 4.17a. These rings indicate a level of polycrystallinity which, given the volume of the sample, suggests a very small crystallite size.

The XRD pattern of the Mg/TM multilayer and, more importantly, the PCI measurements presented in section 4.3.1 indicate the presence of an Mg_2NiH_4 phase which has also been confirmed by TEM. Figure 5.3 shows an image of an Mg/TM particle and a corresponding diffraction pattern. EDX analysis suggested the darker region of the image contains nickel. The diffraction pattern was analysed and a series of bright spots overlaying the magnesium oxide diffraction rings were indexed to the diffraction pattern of $MgNiO_2$ which has an FCC crystal structure and d-spacings within $\pm$ 0.01 Å of those of magnesium oxide, which has also got an FCC crystal structure. This makes differentiation between the two difficult. A series of unidentified spots were also found that match diffraction patterns of Mg_2NiH_4 and magnesium hydride. These were not found in any of the other, more

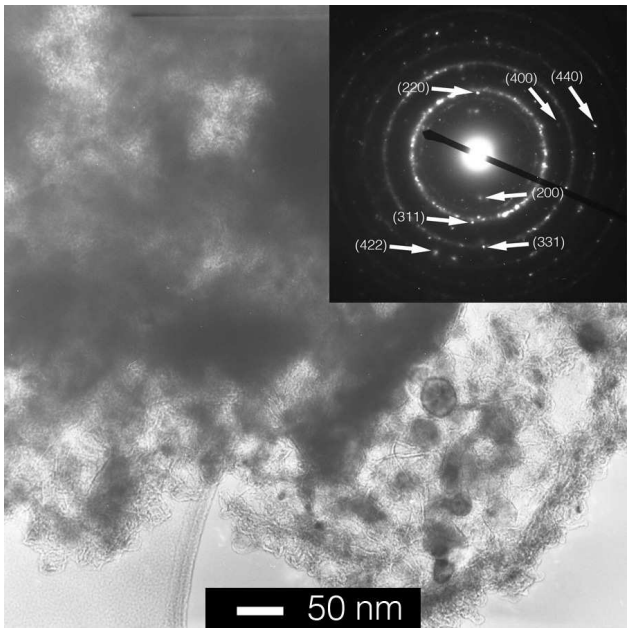

Figure 5.3: SAED pattern showing diffraction rings corresponding to magnesium oxide and a series of spots that can be matches to the pattern of FCC $MgNiO_2$

transparent-looking samples, suggesting that only the smallest particles and the thinnest sections of particles have oxidised.

The nature of the catalyst features in the Mg/Cr and Mg/V samples was further investigated by high-resolution TEM. Figures 4.19b and 4.21b exhibit a series of lattice fringes, with d-spacings matching those of Cr(110) and V(110), obtained from the dark transition metal features in both samples confirming the spots indexed on the diffraction patterns in figures 4.19 and 4.21. This leaves little doubt that what were amorphous layers of transition metal, are now crystalline nano-particles, finely distributed throughout the bulk of the material. Finally, the EDX maps shown in figures 4.20 and 4.22 provide two-dimensional information about the location of elemental chromium and vanadium within the samples. Comparing the corresponding

Z-contrast images with the EDX maps, it is clear that the bright features, which replace the dark features seen in the bright-field images, correspond strongly with the transition metal EDX signal, providing further evidence of the size and location of the transition metal nano-crystals.

The evidence from the XRD, SEM and TEM studies clearly suggests that hydrogen cycling of the thin film material at elevated temperature has caused a significant transformation of the thin films' morphology and microstructure. Kalisvaart *et al.* (2011) compare a number of multilayered and co-sputtered Mg/FeTi thin films that, like the samples presented in this work, were produced by magnetron sputtering. The conditions used were comparable to the ones used in this work with an argon pressure of 5×10^{-3} mbar and continuous sample rotation. 1.5 microns thick, they too were delaminated from the substrate and repeatedly hydrogen cycled. Their multilayer, built from 28 nm thick magnesium layers sandwiched between 5 nm layers of an FeTi alloy, capped on both sides with palladium (Mg/FeTi), is closest in composition to the transition-metal catalysed samples presented in this work and, as such, provides the basis of this comparison. Like the Mg/TM, Mg/Cr and Mg/V samples presented in this work, the Mg/FeTi thin film was subjected to a number of cycles of hydrogenation and dehydrogenation at temperatures of up to 300°C and, after an initial activation period, transforms into a flaky powder. Similarly, the initial microstructure is highly structured in TEM, with highly oriented layers of magnesium separated by FeTi layers that produce neither electron- nor X-ray diffraction. After cycling however the Mg/FeTi particles are reported to have retained some of the layered structure, whereas in the case of the Mg/TM, Mg/Cr and Mg/V

samples there is no clear evidence of any retained layering of magnesium and transition metal layers. This is explained as being a result of cycling the material at temperatures below the re-crystallisation temperature, which is defined as the temperature at which full recrystallisation occurs within 1 hour and it is typically a function of the melting temperature of a given metal or alloy (Callister and Rethwisch, 2011, chap. 8). Upon examining the iron-titanium phase diagram, it can be seen that the melting point for FeTi is 1317°C — far below the melting point of iron (1538°C), let alone chromium (1907°C) and vanadium (1910°C). Thus, given the hypothesis of Kalisvaart *et al.* (2011), it would be expected to see similar behaviour in the materials presented here. Tsai (1989) show that amorphous chromium coatings form crystallites at temperatures as low as 300°C and, given the evidence for crystalline iron and vanadium in the TEM and XRD studies of the Mg/TM and Mg/V coatings in their hydride state, the two transition metal elements appear to behave in a similar manner.

The results presented in this work on the reaction of the palladium capping layers with the magnesium metal to Mg_6Pd agree with the findings Kalisvaart *et al.* (2011) make, both for their multilayers and their co-sputtered $Mg_{80}Fe_{10}Ti_{10}$ thin film. This is despite the insertion of a tantalum layer between the magnesium and the palladium layers, reported by Tan *et al.* (2009) as being an effective barrier for Mg_6Pd alloy formation.

The findings presented by Wang *et al.* (2008) on a 250 nm multilayer, composed of 5 bi-layers of magnesium and nickel, show that annealing of alternating layers of magnesium and nickel for just 4 hours at 200°C is sufficient for the magnesium and nickel phases to disappear from the XRD

pattern and form Mg_2Ni. This concurs with the findings presented in this work on the Mg/TM sample, which was repeatedly cycled at above 250°C for several weeks, forming Mg_2Ni and its hydride Mg_2NiH_4.

Similar to the co-sputtered $Mg_{80}Fe_{10}Ti_{10}$ sample that Kalisvaart *et al.* (2011) compare their Mg/FeTi multilayer sample to, there exist a range of thick, magnesium-based, co-sputtered, transition metal catalysed coatings including one of $Mg_{80}Cr_{10}V_{10}$ (Kalisvaart *et al.*, 2012), one of $Mg_{80}Fe_{10}Cr_{10}$ (Fritzsche *et al.*, 2012) and one of $Mg_{70}Al_{12}Fe_{18}$ (Kalisvaart *et al.*, 2010), that have undergone a structural evolution upon hydrogen cycling to produce hydrogen storage materials with microstructural characteristics similar to the ones presented in this work, caused by a precipitation of transition metal nano-crystallites within the bulk, resulting in small thin film particles with an even distribution of nano-sized transition metal crystallites. For example, the TEM data presented by Fritzsche *et al.* (2012) in their paper on the catalytic effect of FeCr intermetallics shows evidence of FeCr nano-crystallites. The authors suggest they are precipitates, from which it can be inferred that these crystallites were not present in the as-deposited structure.

This opens up questions as to the potential advantages and disadvantages of using multilayer structures over co-deposition of magnesium and catalyst materials, as discussed in section 2.2.6.

5.5 Thermodynamics

Section 4.3.1 describes a range of experiments that were undertaken to study the interaction of the 4 thin film structures with hydrogen. A range of pressure-composition isotherms at temperatures between 250°C and 350°C were measured which were used to derive the thermodynamic properties of the different materials. Whilst the Mg/Cr, Mg/V and $Mg_{control}$ samples' thermodynamics were studied using the manual Sievert's apparatus described in section 3.4.1, the Mg/TM sample's thermodynamics were studied using the PCTpro2000 instrument described in section 3.4.1.

The Mg/Cr, Mg/V and $Mg_{control}$ samples' PCI curves, presented in figures 4.24 to 4.26, show flat dehydrogenation plateaus, characteristic for magnesium hydride. The corresponding van't Hoff plots show a very good fit of the linear regression lines that were used to calculate the enthalpies and entropies of the dehydrogenation reactions of the three thin film materials. At $\Delta H = 72.9 \pm 0.5\,kJ\,mol^{-1}\,H_2$ for the Mg/Cr sample, $\Delta H = 72.6 \pm 0.3\,kJ\,mol^{-1}\,H_2$ for the Mg/V sample and $\Delta H = 72.7 \pm 0.5\,kJ\,mol^{-1}\,H_2$ for the $Mg_{control}$ sample, the enthalpies of the dehydrogenation reactions are very close to literature values for magnesium hydride of $\Delta H = 72.9\ kJ\,mol^{-1}\,H_2$ (Bogdanovic *et al.*, 1999) which suggests that the reactions observed are that of $Mg + H_2 \overset{\Delta H}{\rightleftharpoons} MgH_2$. Similarly, the entropies of the reactions are very close to the theoretical value for magnesium hydride of $\Delta S = 130.7\ J\,K^{-1}\,mol^{-1}\,H_2$ (Grochala and Edwards, 2004) at $\Delta S = 133.1 \pm 1.6\,J\,K^{-1}\,mol^{-1}\,H_2$, $\Delta S = 132.8 \pm 1.6\,J\,K^{-1}\,mol^{-1}\,H_2$ and $\Delta S = 133.9 \pm 1.6\,J\,K^{-1}\,mol^{-1}\,H_2$ for the Mg/Cr, Mg/V and $Mg_{control}$ samples respectively. Unlike many of the palladium

capped thin films in the literature (Baldi *et al.*, 2009a; Barcelo *et al.*, 2010), the thermodynamics of these multilayer structures do not appear to be affected by the choice of process. Regardless of the nano-structure that the samples were given, or the combination of materials, the samples behave like as-received magnesium hydride. Similar behaviour was also observed by Kalisvaart *et al.* (2011), who state an enthalpy of -79 $\mathrm{kJ\,mol^{-1}\,H_2}$ for their Mg/FeTi multilayer which, depending on the errors in their measurements which were not quantified, is in the acceptable range for magnesium hydride.

The formation of Mg_2NiH_4 in the Mg/TM sample is evident from both the X-ray and electron diffraction studies discussed in sections 5.2 and 5.4. It is well known however that the hydride forming alloy Mg_2Ni has thermodynamic properties different to those of magnesium hydride (Reilly and Wiswall, 1968), which is reflected in the PCI study presented in section 4.3.1. Unlike the Mg/Cr, Mg/V and $Mg_{control}$ samples, the Mg/TM sample exhibits a double plateau, which is indicative of either a partial destabilisation of the magnesium hydride phase or a two-phase material. Given the respective enthalpies and entropies derived for the two plateaus from the van't Hoff plots, shown in figure 4.23b, of $\Delta H = 78.0 \pm 2.3\,\mathrm{kJ\,mol^{-1}\,H_2}$ and $\Delta S = 137.9 \pm 3.7\,\mathrm{J\,K^{-1}\,mol^{-1}\,H_2}$ for the lower plateau and $\Delta H = 66.1 \pm 1\,\mathrm{kJ\,mol^{-1}\,H_2}$ and $\Delta S = 122.1 \pm 1.6\,\mathrm{J\,K^{-1}\,mol^{-1}\,H_2}$ for the higher plateau, and by comparing these figures with the literature, it is evident that the lower plateau corresponds to the reaction $Mg + H_2 \overset{\Delta H}{\rightleftharpoons} MgH_2$. This reaction has widely been reported to have an enthalpy of between 72.9 $\mathrm{kJ\,mol^{-1}\,H_2}$ (Bogdanovic *et al.*, 1999) and 79 $\mathrm{kJ\,mol^{-1}\,H_2}$ (Kalisvaart *et al.*, 2011). The higher pressure, lower enthalpy plateau corresponds to reported values of between ΔH

= 64.4 kJ mol^{-1} H_2 (Reilly and Wiswall, 1968) and ΔH = 69.3 kJ mol^{-1} H_2 (Liang *et al.*, 1998) for the reaction $Mg_2Ni + 2\,H_2 \rightleftharpoons^{\Delta H} Mg_2NiH_4$. The entropy change during the dehydrogenation reaction is generally known to be governed by the release of hydrogen gas which has been shown to be ΔS = 130.7 J K^{-1} mol^{-1} H_2 (Grochala and Edwards, 2004). Literature values of the entropy of hydrogen release from magnesium hydride have been reported as high as ΔS = 142.1 J K^{-1} mol^{-1} H_2 (Liang *et al.*, 1998), which is in good agreement with the value calculated for the lower plateau. The value for the higher plateau of ΔS = 122.1 J K^{-1} mol^{-1} H_2 agrees with the value of ΔS = 122.2 J K^{-1} mol^{-1} H_2 that Reilly and Wiswall (1968) report for the dehydrogenation of Mg_2NiH_4.

Comparing the thermodynamic data of the Mg/Cr, Mg/V and $Mg_{control}$ samples with that of the Mg/TM sample, in the light also of the structural study of the materials, it is evident that the alloy formation of the magnesium and nickel phases in the as-deposited thin films resulted in a two-phase hydrogen storage material with two distinct plateau pressures. Derived from equations 1.3 and 1.4, the temperature at which the different materials release 1 bar of hydrogen can be calculated from the relationship

$$T_{1bar} = \frac{\Delta H}{\Delta S} \tag{5.1}$$

and table 5.1 lists the T_{1bar} for the different materials and, in the case of the Mg/TM sample, the separate phases.

The literature value of T_{1bar} of magnesium hydride is 278.4°C, and from these results it can clearly be seen that the measured T_{1bar} of the coatings is

Sample		T_{1bar}
Mg/TM	MgH_2 phase	$292.6 \pm 22.5°C$
	Mg_2NiH_4 phase	$268.4 \pm 10.8°C$
Mg/Cr		$277.5 \pm 7.6°C$
Mg/V		$276.5 \pm 7.0°C$
$Mg_{control}$		$275.2 \pm 7.6°C$

Table 5.1: T_{1bar} of the 4 multilayer samples

within measurement errors of the theoretical value.

5.6 Kinetics

Having established the thermodynamics of the chemical reactions forming the underlying mechanism by which the materials presented store and release hydrogen, section 4.3.2 looks at a range of experiments that were undertaken to establish, given the thermodynamic constraints, the kinetics of the 4 materials' reaction with hydrogen at realistic operating temperatures.

The hydrogenation experiments carried out at different temperatures show that all 4 samples are sensitive to changes in temperature within the measured range and the time taken to hydrogenate the samples to 80%, and 90% in the case of the Mg/TM sample, slows significantly as the temperature decreases. The 80% and 90% cut-off points for the completion of the reaction were chosen because above this point, especially in the case of the Mg/Cr, Mg/V and $Mg_{control}$ samples, the reaction becomes very slow, possibly due to a change in the mechanism that limits the reaction rate. Given the reduction of the diffusion coefficient during hydrogenation, as discussed by Kalisvaart *et al.* (2011), this phenomenon can be put down to diffusion of hydrogen through the hydride phase slowly taking over from the dissociation of hy-

drogen and nucleation and growth of the hydride phase as the predominant reaction-rate limiting factor, slowing down the reaction progressively.

From the results presented in table 4.4, it is evident that the Mg/TM sample is consistently much faster than the other 3 samples, hydrogenating to 90% of its maximum capacity at 310°C in almost half the time it takes to hydrogenate the next-fastest sample, the Mg/V coating, to only 80% at 320°C. If diffusion through the hydride phase in the Mg/Cr, Mg/V and $Mg_{control}$ samples is the rate-limiting factor during the later stages of the reaction, this might be explained by the fact that the Mg/TM sample has two hydride-forming phases, one of which forms Mg_2NiH_4. In an Mg-23.5 wt% Ni alloy, Mg_2NiH_4 has been shown to have a more favourable coefficient for the diffusion of hydrogen through the hydride phase compared with magnesium hydride (Čermák and Král, 2008).

Comparing the hydrogenation kinetics of the Mg/Cr and Mg/V samples with the $Mg_{control}$ sample, it is clear that at 320°C there is no significant difference between the three materials. At the lower temperatures however the $Mg_{control}$ sample's hydrogenation kinetics slow down substantially compared with the two catalysed samples. Given the relationship of the reaction rate and temperature used in the Arrhenius equation (equation 4.3) to establish the activation energy of a chemical reaction, this implies a lower activation energy for the hydrogenation reaction of the catalysed samples. This could be caused by the smaller grain size compared with the $Mg_{control}$ sample, allowing faster diffusion of hydrogen through the growing hydride phase (Siviero *et al.*, 2009), as well as improved dissociation of hydrogen at the catalyst sites (Yang *et al.*, 2010) and an increase in the rate of nucleation and growth

of the hydride phase (Croston *et al.*, 2010).

Since a practical hydrogen store has to be able to release the stored hydrogen as well as store it, a range of similar experiments were done to measure the rate of hydrogen release from the 4 samples at different temperatures. Since the dehydrogenation of the Mg/Cr, Mg/V and $Mg_{control}$ samples was much faster than the hydrogenation, the cut-off point for the measurement was set to 90% for all 4 samples. It is evident comparing the 4 samples that the three catalysed samples have very similar dehydrogenation kinetics, dehydrogenating 90% of their maximum capacity between 12.1 and 13.2 minutes at 250°C. The $Mg_{control}$ sample in contrast is significantly slower, taking 6 times as long to dehydrogenate, which implies that both the increased grain size and the absence of a (nano-)crystalline transition metal catalyst phase result in a significant slowing of the dehydrogenation kinetics of magnesium thin films.

The Mg/Cr and Mg/V samples are several minutes faster in dehydrogenating 90% of their maximum capacity at the lower temperatures than they are in hydrogenating only 80% of their maximum capacity at the same temperatures, which supports the argument that the hydrogenation kinetics of these two samples are limited not only by the thermodynamics of the (de-)hydrogenation reaction but also somewhat by the different diffusivity of hydrogen atoms through the magnesium and magnesium hydride phases.

Whilst it has kinetics comparable to the Mg/Cr and Mg/V samples in dehydrogenation, the Mg/TM sample has superior hydrogenation behaviour. Given that in general, as will be shown in section 5.7, transition metal catalysts including the ones used in this work promote similar kinetic benefits,

the much improved hydrogenation kinetics in the Mg/TM sample compared with the Mg/Cr and Mg/V samples can only be due to the formation of the Mg_2Ni phase in addition to the formation of transition metal nano-crystals, which was also seen in the Mg/Cr and Mg/V samples.

5.7 Reaction Mechanisms

Other than the diffusion of hydrogen through the metal or hydride phase, the mechanism and rate of growth of the hydride phase, in the case of the hydrogenation reaction, and the metal phase, in the case of the dehydrogenation reaction, and their relationship with temperature are important factors that determine the kinetics that govern the reactions and result in the times measured. Since the rate of the reaction changes with the degree of hydrogenation, given a known mechanism, mathematical models can be used to linearise the (de-)hydrogenation curves from which the rate constant k can be derived. A plot of $\ln(k)$ vs $1/T$, as described in section 4.3.2 then allows calculation of the activation energy E_a which, as part of the Arrhenius equation 4.3, describes the relationship between the reaction rate of any given reaction and temperature, and provides a measure of the effectiveness of a catalyst in catalysing a reaction.

Three different models exist that have been widely used to describe the (de-)hydrogenation kinetics of hydrogen storage materials (Varin *et al.*, 2008). These models describe the relationship between the fraction converted, α, and time, linked by the rate constant k and, when fitted to experimental data, reveal the rate-limiting mechanism (Barkhordarian *et al.*, 2004) since the faster mechanisms won't affect the actual kinetics of the sample.

If the dissociation or re-combination of hydrogen molecules on the material's surface is the rate-limiting mechanism, the surface-controlled (SC) reaction model applies (Barkhordarian *et al.*, 2006), in which the converted fraction α has a linear relationship with time through

$$\alpha = kt. \tag{5.2}$$

The contracting volume (CV) model assumes nucleation at the surface of the a particle has already occurred and describes the growth of the new phase from the surface into the bulk of a particle with a constant interface velocity (Barkhordarian *et al.*, 2006; Varin *et al.*, 2008). This is assuming that the initial nucleation is fast in comparison with the bulk of the reaction and that the diffusion of hydrogen through the bulk is not rate-limiting. This model is represented by the relationship

$$1 - [1 - \alpha]^{\frac{1}{x}} = kt \tag{5.3}$$

where x is either 2 or 3 depending on whether the growth occurs in two or three dimensions.

Mintz and Zeiri (1994) derive an equation, similar to equation 5.3, that takes into account a slowing of the CV growth interface by diffusion which might occur in samples where diffusion of hydrogen through the transformed phase might become rate-limiting. The equation that describes this situation

for three-dimensional CV growth is

$$1 - (\frac{2\alpha}{3}) - (1-\alpha)^{\frac{2}{3}} = kt \tag{5.4}$$

which is also known as the Ginstling-Brounshtein model (Khawam and Flanagan, 2006).

Finally, the Johnson-Mehl-Avrami-Kolmogorov (JMAK) model is a mathematical model for random nucleation of a new phase in the bulk and on the surface of a material and assumes that the sample size is significantly larger than any individual transformed region (Kelton, 1997). This sigmoidal reaction curve is described by

$$\alpha = 1 - e^{-(kt)^n} \tag{5.5}$$

which can be linearised to

$$-\ln(1-\alpha)^{\frac{1}{n}} = kt \tag{5.6}$$

where n is the Avrami exponent. This exponent provides information about the dimensionality of the transformation and whether the phase transformation is diffusion- or interface limited (Kelton, 1997), with $n = 2$ for two-dimensional growth of existing nuclei with a constant interface velocity, and $n = 3$ for three-dimensional growth with a constant interface velocity (Varin *et al.*, 2008).

Data for the converted fraction α from the dehydrogenation experiments described in section 4.3.2 was entered into the left hand side of these models'

equations and plotted against time to generate a series of graphs. A good fit with a particular model was then judged from the shape of the resulting curve in comparison to a straight line.

Khawam and Flanagan (2006) show and compare typical reaction curves that the different models describe for the different mechanisms. Reactions that follow the JMAK model generally follow a sigmoidal curve, the exact shape of which is determined not only by the rate of the reaction but also by the Avrami exponent, n. As a result of this, double-logarithm fitting (Kelton, 1997) is generally recommended over simple fitting to equation (5.6) (Varin *et al.*, 2008) to ensure the best fit which results in

$$\ln[\ln(\frac{1}{1-\alpha})] = n\ln(k) + n\ln(t). \tag{5.7}$$

Fitting this equation to the experimental data should produce a straight line from which both the Avrami exponent n and the rate constant k can be calculated.

Re-arranging the Arrhenius equation (equation 4.3) reveals the linear relationship

$$\ln(k) = -\frac{E_a}{R}\frac{1}{T} + \ln(A) \tag{5.8}$$

from which, by a plotting of $\ln(k)$ vs $\frac{1}{T}$, the activation energy of the reactions can be calculated from the slope of the linear regression line.

A reasonable fit was established between the JMAK model and the data for the Mg/TM sample. Table 5.2 compares the n and k values calculated from the slopes and intercepts of the straight lines, shown in figure 4.27a that were fitted to the data linearised using equation 5.7. These n and k

Temperature (°C)	n	k
250	1.1	0.143
290	1.1	0.668
350	1	0.319

Table 5.2: n and k values derived from the JMAK model for the Mg/TM sample

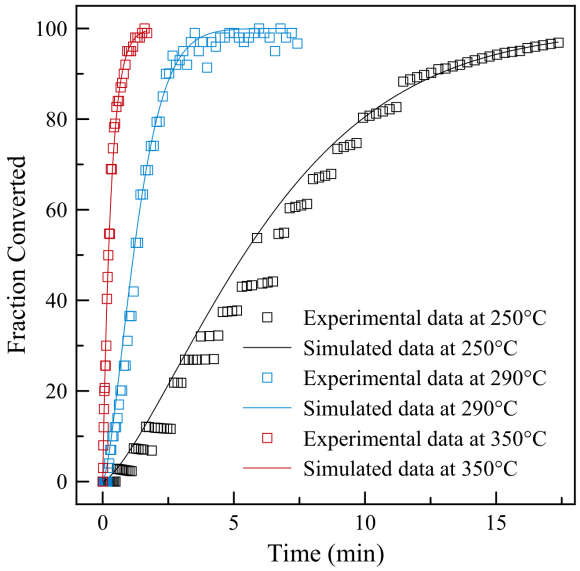

Figure 5.4: Dehydrogenation kinetics of the Mg/TM sample showing the experimental data and the data derived from the JMAK model using the parameters from table 5.2 at 250°C, 290°C and 350°C

values were then used to produce the graph in figure 5.4, which compares the experimental dehydrogenation data for the Mg/TM sample with data modelled using the JMAK parameters shown in table 5.2.

The figure shows a good fit between the experimental data and the model, verifying the linear correlation of the model and the experimental data shown in figure 4.27a.

The Mg/Cr sample did not fit the JMAK model well, resulting in a con-

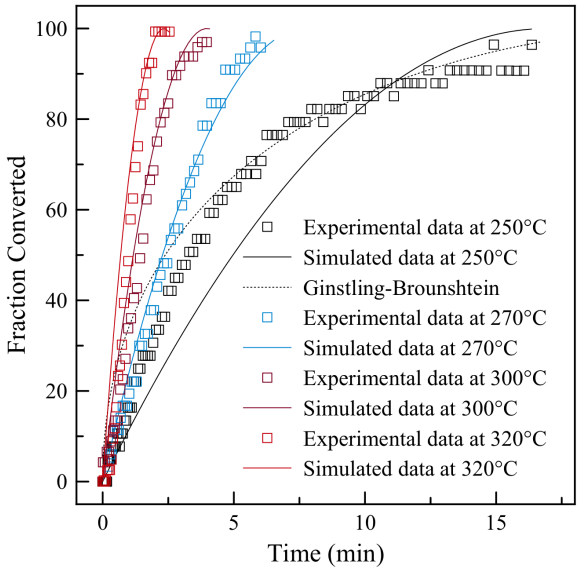

Figure 5.5: Dehydrogenation kinetics of the Mg/Cr sample showing the experimental data and the data derived from the CV model with $x = 2$ at 250°C, 270°C, 300°C and 320°C

tinuous curve rather than the straight line that is prescribed for a good fit. Kelton (1997) explains this is a symptom of a violation of the basic assumptions that are made in the model and means a different model has to be chosen. In this case, the CV model with $x = 2$ was chosen (equation 5.3) since it provided the best fit at all temperatures. At 250°C however, the Ginstling-Brounshtein model (equation 5.4) provided the best fit, which suggests that the tailing-off of the CV model is due to diffusion taking over as the rate-limiting factor, resulting in a slowing of the reaction beyond what the CV model dictates. Figure 5.5 compares the experimental data with data modelled using the rate-exponents k, calculated from the linear-regression lines shown shown in figure 4.28a.

For the lower temperature reaction at 250°C, the modelled data using the

Ginstling-Brounshtein model (equation 5.4) is also shown, which indicates that the experimental data lies between the two models. The Ginstling-Brounshtein model produces a continuous curve, which is true for the later part of the reaction, but for the first half of the reaction the shape of the $CV_{x=2}$ curve matches the experimental data more closely. This suggests that the $CV_{x=2}$ model is valid for the first part of the reaction, with a higher value for k and therefore a steeper gradient, since the value derived from fitting the experimental data to the model is reduced by the later part of the reaction being slowed by diffusion.

For the Mg/V sample, the JMAK model seemed to provide the best straight-line fit for the dehydrogenation data, except for the dehydrogenation at 250°C, where diffusion was the rate-limiting factor. This results in the tailing-off of the curve above ca. 80% dehydrogenation.

Temperature (°C)	n	k
250	1.3	0.179
270	1.4	0.25
300	1.4	0.766
320	1.6	1.09

Table 5.3: n and k values derived from the JMAK model for the Mg/V sample

Table 5.3 compares the n and k values for the Mg/V samples at different temperatures which were used to plot the reaction curves in figure 5.6, comparing the actual experimental data with data modelled using the JMAK parameters shown in table 5.3.

A good match between the experimental and simulated data is evident from the plot, except for the measurement at 250°C where diffusion slows the

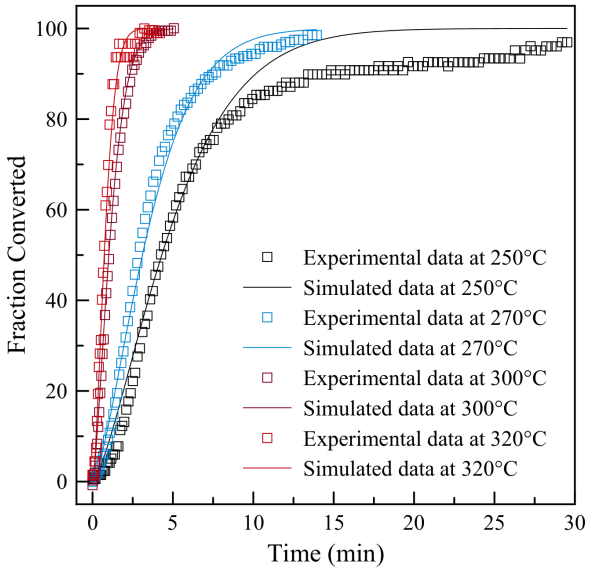

Figure 5.6: Dehydrogenation kinetics of the Mg/V sample showing the experimental data and the data derived from the JMAK model using the parameters from table 5.3 at 250°C, 270°C, 300°C and 320°C

experimental data beyond 80% dehydrogenation. A similar slowing of the experimental kinetics towards the final stages of dehydrogenation is noticeable also at 270°C but to a much lesser extent.

As with the Mg/TM and Mg/V samples, the $Mg_{control}$ sample has a good fit with the JMAK model, resulting in the n and k values which are presented in table 5.4.

Temperature (°C)	n	k
300	1.6	0.019
320	1.5	0.061
350	1.9	0.219

Table 5.4: n and k values derived from the JMAK model for the $Mg_{control}$ sample

These values were used to produce the modelled dehydrogenation curves

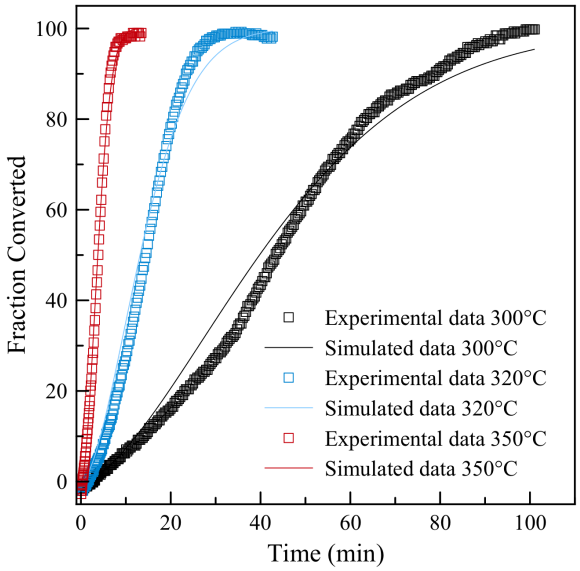

Figure 5.7: Dehydrogenation kinetics of the $Mg_{control}$ sample showing the experimental data and the data derived from the JMAK model using the parameters from table 5.4 at 300°C, 320°C and 350°C

that are compared with the experimental curves presented in figure 5.7. Since the kinetics were prohibitively slow at temperatures below 300°C, no measurements were possible below this temperature and, as a result, no influence of diffusion was noticed. This suggests that the influence of diffusion on the dehydrogenation kinetics of the presented hydrogen storage materials plays a role only at temperatures below 300°C. In the case of the Mg/TM sample, no limitation of the dehydrogenation by diffusion was measured, which might further support the argument of the magnesium-nickel intermetallic providing diffusion pathways inside the material that are not present in the other three samples.

One of the main differences between the JMAK and CV models is the assumption in the CV model that nucleation is fast, and therefore negligible.

Since the only difference between the Mg/Cr, Mg/V and $Mg_{control}$ samples is the presence and composition of catalyst interlayers this might suggest that the element chromium as a catalyst is the cause of the change in the rate-limiting mechanism of the reaction that is observed.

Liang *et al.* (1999a) suggest the catalytic activity of 3d-transition metals in magnesium-based hydrogen storage materials occurs by chemisorption of hydrogen by the catalyst, which then transfers the dissociated hydrogen to the magnesium. They claim that the interface between the magnesium and catalyst material provides an active nucleation site for the formation of magnesium hydride, with the transition metal catalyst acting to reduce the nucleation barrier. The authors observe no nucleation period which, judging by the sigmoidal shape of their dehydrogenation curves, is potentially incorrect, but no best-fit data with kinetic models is shown and instead the authors claim a change from a JMAK-type reaction mechanism to a CV-type mechanism that limits the rate of their reactions. This was seen for the Mg/Cr sample presented in this work, which agrees with the hypothesis that the catalyst materials affect the reaction mechanisms as well as the rate of the reactions.

The Mg/Cr and Mg/V samples presented in this study exhibit very similar kinetic properties both in terms of dehydrogenation time and activation energy for the dehydrogenation reaction. The difference in reaction mechanism however, coupled with the slightly lower activation energy, suggests that the chromium catalyst might be more effective in reducing the nucleation barrier for the dehydrogenation reaction. The difference in activation energy is small (1.4 $kJ\,mol^{-1}$) but consistent with the DSC measurements,

presented in section 4.3.3, which show a reduced activation energy ($\Delta E_a = 5.3\,\mathrm{kJ\,mol^{-1}}$) for the Mg/Cr sample compared with the Mg/V sample.

Although very little is known about the properties of elemental chromium in catalysing the hydrogen storage in magnesium (Zahiri *et al.*, 2012), oxides of chromium have been known to possess very good catalytic properties for magnesium-based hydrogen storage materials (Varin *et al.*, 2011). Whilst Zahiri *et al.* (2012) claim, based on an electrochemical study by Niessen and Notten (2005), that chromium is a poor catalyst in comparison with vanadium and conclude that combining the two is beneficial, Vincent *et al.* (2011) study and compare the characteristics of magnesium, cold rolled and ball milled with various transition metal catalysts. They conclude that chromium and vanadium have very similar kinetics in terms of the dehydrogenation time at 350°C for their cold rolled samples, whereas for their ball milled samples they notice a considerable improvement of kinetics with the vanadium catalyst over the chromium one. The results shown in chapter 4 shows however, that elemental chromium promotes favourable hydrogenation and dehydrogenation kinetics in magnesium hydride, compared with elemental vanadium.

It has been suggested that the reaction mechanism of hydrogen storage materials might change with temperature (Jensen *et al.*, 2006), shown also by the small increase in n for the JMAK-governed materials presented in this work, most likely caused by the changing influence of diffusion on the dehydrogenation kinetics. The Avrami exponent n has been discussed in the literature and it is often said to be linked to the geometry of the phase transformation (Varin *et al.*, 2008), the nucleation rate and growth morphology (Sun *et al.*, 2003), and to whether it is interface or diffusion limited (Kel-

ton, 1997). Bazzanella *et al.* (2011) on the other hand state that a value of $n = 4$, measured for pure MgH_2, indicates that nucleation of magnesium in the hydride phase limits the reaction rate whilst a value of $n = 1$, measured for samples catalysed with up to 5 at.% of niobium, is indicative of instantaneous nucleation, followed a diffusion limited reaction. It is therefore unwise to interpret a lot of meaning into a number that can have such a wide range of meanings. The validity of the model to the reactions presented is however confirmed by the fact that the Avrami exponent is consistent across the different samples, as well as the fact that the data has a very good fit with the model shown in figures 5.4, 5.6 and 5.7.

5.8 Kissinger Analysis

The results of the Kissinger analysis confirm the findings that were derived from the kinetic modelling. The three catalysed samples have, for the lower temperature peaks, activation energies that are ca. 10 $kJ\,mol^{-1}$ lower than the values that were established from the models. The relative energies are however, within the errors, the same, indicative of a possible systematic error. For the catalysed samples, the DSC curves exhibit multiple peaks with different activation energies, as shown in section 4.3.3. The larger, lower temperature peaks have a consistently lower activation energy than the small, higher temperature peaks, which might be explained by a portion of the material not being catalysed as efficiently as the rest. In the Mg/TM sample this second peak is far more intense than in the Mg/Cr and Mg/V samples and might also be caused by the Mg_2NiH_4 phase.

The presence of these multiple peaks however suggests that multiple re-

actions are occurring upon dehydrogenation of the samples, which might have subsequently caused the shift in the activation energy derived from the kinetic models to higher values since this will provide an average of both reactions. By multiplying the two activation energies for each sample with the relative peak area calculated from the fitted peaks, corrected values for the activation energy were calculated. Presented in table 5.5, these values match much more closely the values derived from the kinetic models.

Sample	E_a	
	$DSC_{corrected}$	Kinetic model
Mg/TM	$78.5 \pm 3.5\,kJ\,mol^{-1}$	$80.0 \pm 4.4\,kJ\,mol^{-1}$
Mg/Cr	$65.7 \pm 2.5\,kJ\,mol^{-1}$	$69.7 \pm 5.8\,kJ\,mol^{-1}$
Mg/V	$67.6 \pm 1.2\,kJ\,mol^{-1}$	$71.1 \pm 5.0\,kJ\,mol^{-1}$

Table 5.5: Comparison between the activation energy derived from the kinetic models and the corrected activation energy derived from Kissinger curves for the Mg/TM, Mg/Cr and Mg/V samples

The $Mg_{control}$ sample confirms the validity of both the DSC and modelling data for the activation energy, since the values of $141.6 \pm 3.2\,kJ\,mol^{-1}$ and $142.9 \pm 5\,kJ\,mol^{-1}$, which were derived from the calorimetric and volumetric measurements presented in sections 4.3.2 and 4.3.3, are within the quoted errors of each other and well within the range quoted in the literature, with values between 120 $kJ\,mol^{-1}$ and 156 $kJ\,mol^{-1}$ (Huot *et al.*, 1999; Walker, 2008). Finally, a sample of as-received MgH_2 was run in the DSC under the same conditions as the 4 thin film samples. With an activation energy of 147.7 $kJ\,mol^{-1}$, the results validate the claim that the $Mg_{control}$ sample's kinetics are not catalysed and that the sample therefore provides a good base-line to compare the catalysed samples with.

The activation energies of the thin film samples are comparable also with

Composition	Activation energy	Reference
Mg/TM	71.6 kJ mol^{-1}	(Fry *et al.*, 2013)
Mg/Cr	60.6 kJ mol^{-1}	this work
Mg/V	65.9 kJ mol^{-1}	this work
$MgH_{2_{milled}}$	96 kJ mol^{-1}	(Lu *et al.*, 2009)
$Mg_{0.8}Cr_{0.07}V_{0.13_{thinfilm}}$	91.5 kJ mol^{-1}	(Zahiri *et al.*, 2012)
Mg-$Pd_{thinfilm}$	48-80.4 kJ mol^{-1}	(Qu *et al.*, 2009b, 2010b)
MgH_2+Ti	71.1 kJ mol^{-1}	(Liang *et al.*, 1999a)
MgH_2+TiO_2	72 kJ mol^{-1}	(Croston *et al.*, 2010)
MgH_2+V	62.3 kJ mol^{-1}	(Liang *et al.*, 1999b)
MgH_2+Mn	104.6 kJ mol^{-1}	(Liang *et al.*, 1999a)
MgH_2+Fe	67.6 kJ mol^{-1}	(Liang *et al.*, 1999a)
MgH_2+Ni	88.1 kJ mol^{-1}	(Liang *et al.*, 1999a)
MgH_2+$Nb_{thinfilm}$	51-78 kJ mol^{-1}	(Bazzanella *et al.*, 2011)
MgH_2+Nb_2O_5	61 kJ mol^{-1}	(Barkhordarian *et al.*, 2004)

Table 5.6: Comparison of the catalysed samples' activation energies with literature values for materials of similar composition

the literature. Table 5.6 compares the thin film samples' activation energies with literature values for materials of similar composition. While most of these materials are ball-milled, there are a few thin film samples included in the list which were produced by co-sputtering of magnesium with the respective transition metal(-mix) (Zahiri *et al.*, 2012) or composed of magnesium with a palladium cap (Qu *et al.*, 2009b). The samples presented in this work compare well with the lowest activation energies from the literature, notably the ball-milled magnesium hydride samples catalysed with metallic iron and vanadium (Liang *et al.*, 1999a) and niobium oxide (Barkhordarian *et al.*, 2004).

It is also noteworthy that both the DSC and Sieverts measurements of the dehydrogenation kinetics were done after ca. 50-60 cycles of hydrogenation and dehydrogenation. Whilst Huhn *et al.* (2005) observe a degradation

of the storage kinetics of their niobium oxide-catalysed, ball-milled magnesium hydride material, the values of activation energy measured for the samples presented in this work tally with literature values of similar materials, as shown in table 5.6. This suggests the dehydrogenation kinetics remain favourable even after 50-60 cycles of hydrogenation and dehydrogenation.

5.9 Activation and Cycling Behaviour

Looking at the kinetic evolution of the samples, shown in section 4.3.4, an evolution of the hydrogenation and dehydrogenation kinetics, in terms of the (de-)hydrogenation rate, is evident. Whilst the Mg/TM sample sees stability and improvement of the dehydrogenation kinetics between the 1^{st} and the 5^{th} and also between the 5^{th} and the 50^{th} cycles, the Mg/Cr and Mg/V samples see an overall deterioration in their dehydrogenation kinetics, with a decreasing reaction rate after an initial activation period during the first 5 cycles.

An explanation might be found in the structural evolution the materials underwent. Similar behaviour was noticed by Kalisvaart *et al.* (2011) who describe an initial acceleration of the dehydrogenation kinetics followed by a slowing of kinetics between the 10^{th} and 25^{th} cycles for their Mg/FeTi multilayer samples. This is not the case for their co-sputtered sample which shows an improvement in kinetics followed by near-constant kinetics, supporting the argument that the structural evolution in multilayer thin films and subsequent grain growth in the magnesium phase influences the dehydrogenation kinetics by increasing diffusion pathways.

It has been established that diffusion plays an important part in shaping

the hydrogenation behaviour of all 4 materials and it has been demonstrated in section 5.6 that the formation of Mg_2Ni provides favourable conditions for the Mg/TM sample's hydrogenation kinetics. Similarly, the large initial improvement of the Mg/TM sample's dehydrogenation kinetics, relative to the virtually unchanged dehydrogenation kinetics during the first 5 cycles for the Mg/Cr and Mg/V samples, might be explained by the formation of Mg_2Ni providing improved diffusion and thus improved kinetic stability during hydrogen cycling.

The levels of grain growth were shown to be higher for the Mg/Cr sample than for the Mg/TM and Mg/V samples, as shown in section 4.2. This increased diffusion distance might then explain the increased dehydrogenation time between the 5^{th} and 50^{th} cycle between the Mg/Cr and Mg/V samples of 75 s and 37 s. The grain growth of the Mg/TM sample is less pronounced, which might contribute to the kinetic cycling stability, discussed as a result of the formation of of Mg_2Ni.

All three catalysed samples exhibit stable hydrogenation kinetics after the 5^{th} cycle compared with the first 5 cycles. After the first cycle the kinetics improve drastically, followed by a small improvement up to cycle 5. This might be a result of the structural transformation the thin films underwent during hydrogen cycling. This includes the formation of new intermetallic phases such as Mg_6Pd in all samples and Mg_2Ni in the Mg/TM sample, the formation of (nano-)crystalline transition metal particles in the transition metal catalysed samples and the resulting breaking up of the thin film structures into flaky powders, exposing a much larger surface area to hydrogen, which allows better dissociation of hydrogen at the surface. Indeed, Atias-Adrian

et al. (2013) and Andreasen *et al.* (2005) credit the activation processes they observe in their Mg_2Ni and magnesium-based samples respectively, to the creation of new surfaces and reduced diffusion pathways during initial hydrogen cycles. The initial formation of MgH_2 might also introduce crystal defects into the coatings, which may act as new nucleation sites for hydride formation, speeding up the nucleation and ultimately growth of the hydride phase.

In the case of the $Mg_{control}$ sample, the activation process takes much longer, with the sample reaching only 80% of its maximum capacity in cycle 3 compared with full hydrogenation in the catalysed samples. This might support the argument that the formation of (nano-)crystalline transition metal phases assists the decrepitation of the thin film material, speeding up the rate of activation. This is further supported by the SEM images shown in section 4.2.2, where the $Mg_{control}$ sample appears to have retained more of its original thin film structure than the catalysed samples. Finally, the $Mg_{control}$ sample has a bigger crystallite size to start with and experiences a higher level of grain growth during hydrogen cycling which leads to an increased length of diffusion pathways.

This then also explains the $Mg_{control}$ sample's continuous activation process for the dehydrogenation reaction. Incomplete hydrogenation, due to reduced kinetics, is continually improved by decrepitation of the thin film structure, but at a much slower rate than for the catalysed samples due to the absence of amorphous transition metal interlayers, which distort the structure through the formation of (nano-)crystallites.

The TGA results shown in section 4.3.5 confirm, within errors, the ca-

pacities measured by volumetric methods as described in section 3.4.2.

A third, theoretical measure of capacity for the four samples was calculated from the elemental composition of the thin film samples presented in tables 4.1 and 4.2. Theoretical capacities were derived from the atomic composition of the samples, presented in section 4.2.2. All hydrogenated powders exhibit diffraction lines of Mg_6Pd, as shown in section 4.2, and there is no evidence of hydrogen storage in the magnesium-palladium intermetallic phase which would have presented itself as diffraction lines for Mg_2Pd_5 (Dufour and Huot, 2007). The formation of Mg_6Pd will therefore have contributed to the capacity loss observed, since any magnesium alloyed with the palladium capping layers will no longer be able to contribute to the (de-)hydrogenation reactions. Kalisvaart *et al.* (2011) also show XRD peaks for Mg_6Pd in their hydrogenated Mg/FeTi multilayer, suggesting their magnesium-palladium intermetallic is inactive, as seen with the materials presented in this work. Hence, adjustments were made for the formation of Mg_6Pd, which was treated as inactive material.

Sample	Capacity (wt%)		
	Theoretical	TGA	Sieverts
Mg/TM	5.1 ± 0.3	4.2 ± 0.1	4.6 ± 0.2
Mg/Cr	6.6 ± 0.4	5.7 ± 0.1	6.1 ± 0.3
Mg/V	6.3 ± 0.4	5.2 ± 0.1	5.4 ± 0.3
$Mg_{control}$	7.1 ± 0.4	5.1 ± 0.1	5.4 ± 0.2

Table 5.7: Comparison between the calculated, theoretical capacity of the 4 samples and the capacity measured by gravimetric and volumetric methods

Table 5.7 compares the 4 samples' theoretical capacities with those measured by gravimetric and volumetric methods. It is evident, even after accounting for the losses shown during cycling due to kinetics, that there is

a discrepancy between the theoretical capacity and measured capacity. The XRD patterns in section 4.2.1 show evidence of magnesium oxide, which, an inactive phase in itself, might also act as an activation barrier, further reducing the actual capacity of the material (Sandrock, 1999).

The discrepancy between the theoretical and measured capacity is particularly pronounced in the $Mg_{control}$ sample at 2 wt%. A possible explanation might be an incomplete reaction caused by poor kinetics due to the lack of an active catalyst which would enable better dissociation and diffusion of hydrogen and thus facilitate hydrogen cycling.

Comparing the materials presented in this work with co-sputtered thin film materials of similar composition it becomes clear that the distribution of catalyst material throughout the bulk is very important. Whilst the dehydrogenation kinetics are comparable with those of the Mg/Cr and Mg/V multilayers, co-sputtered materials of similar composition exhibit far superior hydrogenation kinetics at lower temperatures. Fritzsche *et al.* (2012) present a co-sputtered Mg-Fe-Cr composite which hydrogenates at 200°C in ca. 2 minutes, compared with a dehydrogenation at the same temperature in around 20 minutes. The authors suggest the catalytic effect of the BCC alloy comes from its greater ability to permit diffusion of deuterium in the thin film structure. Similar findings were made by Kalisvaart *et al.* (2011) and Zahiri *et al.* (2012), who have produced co-sputtered hydrogen storage materials with well-distributed catalyst precipitates in a magnesium matrix, which have excellent hydrogenation kinetics. This might also support the argument that the Mg_2Ni, formed due to alloying of the magnesium and transition metal layers in the Mg/TM sample, assists the diffusion of hy-

drogen through the hydriding sample, thus speeding up the hydrogenation kinetics drastically compared with the samples that have transition metal interlayers that are immiscible in magnesium.

5.10 Summary

A process has been developed for the University of Nottingham allowing the use of thin film technology to generate thin film multilayer materials for hydrogen storage in quantities sufficient for analysis using volumetric and gravimetric hydrogen sorption equipment. This enables the characterisation of these novel materials using existing equipment.

It has been shown that these materials are comparable in performance to materials synthesised by mechanical methods, including high-energy ball milling, which is a much more energy- and time intensive process compared with PVD technology. Furthermore PVD provides greater levels of control over the (nano-)structure of the resulting material as well as the composition. Co-deposition and multilayering techniques add a further dimension which allows "tailoring" of structures far beyond the capabilities of mechanical synthesis.

The thin film materials presented in this work have the unique characteristic whereby thin, amorphous layers of transition metal catalysts form nano-crystallites during hydrogen cycling, resulting in the decrepitation of the thin film multilayer structure. It has been shown that a fine distribution of these catalyst phases in the magnesium matrix is achieved, resulting in fast hydrogen storage kinetics. It has also been shown that the addition of magnesium-miscible nickel into the interlayer leads to fast hydrogenation

kinetics, due to an increase in diffusion pathways. Although several examples of magnesium thin films with nickel exist in the literature, none study the kinetics, and none combine nickel with other transition metal catalysts, bar a MgNi/Pd system presented by Ouyang *et al.* (2006). Crucially however, palladium is miscible in magnesium, whilst the transition metals added to the nickel interlayer in the Mg/TM sample are not. This leads to further catalysis of the already well studied Mg_2Ni, resulting in fast hydrogen storage kinetics. The magnesium-rich, non-stoichiometric composition of the magnesium-transition metal composite enables a higher capacity compared with stoichiometric Mg_2Ni, providing a cheap and abundant hydrogen storage material with fast kinetics and a high cycling stability.

Chapter 6

Final Thoughts

6.1 Introduction

This chapter aims to draw together the findings presented in chapter 4 in the light of the discussion of these results in chapter 5. The main findings are summarised and conclusions are drawn in order to make this body of work a self-sufficient entity. The conclusions are then used, in conjunction with evidence from the literature, to suggest future work which might be done, placing this body of work at the forefront of future developments, driving forward the development of new technology and linking the processes and ideas used on a laboratory scale to industrial processes.

6.2 Conclusions

The main objective of this work was to produce a novel body of work, using thin film technology, to develop magnesium-based hydrogen storage materials and to study their hydrogen storage behaviour, and hydrogen storage kinetics in particular, in order to understand the effect of transition metal catalysts thereupon. In-depth microstructural characterisation was carried

out in order to understand not only the mechanisms behind the performance and transformation of the thin film coatings, but also the relationship between the processes employed, the materials used and the structural evolution and hydrogen storage properties of the materials generated.

The original contribution to knowledge of this work lies in the development and testing of thin film hydrogen storage materials with novel structures and combinations of materials. Using the findings from the literature, it was identified that, although multilayers of magnesium and transition metals have been studied, the effect of a combination of an alloy forming element (nickel) and elements immiscible in magnesium (iron, chromium, vanadium) on the hydrogen storage behaviour of these thin films has not been studied. In addition, this work pushes the limits of the transition metal layer thickness and the resulting possibilities in terms of reducing the thickness of the magnesium layers in multilayer structures have been explored, showing the effect of re-crystallisation of amorphous layers of transition metals on the structural evolution of these thin films as well as the hydrogen storage properties.

6.2.1 Structural Evolution

It was found that very thin, amorphous layers (< 3 nm) of transition metal catalysts composed of nickel co-sputtered from stainless steel as well as elemental chromium and vanadium form nano-crystallites upon hydrogen cycling of magnesium/transition metal multilayers at temperatures between 250 and 350°C which are finely distributed throughout the bulk of the sample. As a result, the thin films undergo pronounced decrepitation, caused by this microstructural evolution in addition to the cyclic volume expansion

due to hydrogen uptake and release. It was also found that capping layers of palladium, included to prevent oxidation of the thin film structures, are detrimental to the hydrogen storage capacity of the materials presented here due to the formation of an Mg_6Pd alloy upon hydrogen cycling at elevated temperatures.

The processing conditions that were used resulted in highly oriented, discontinuous microstructures consisting of 150 crystalline layers of magnesium (thickness < 20 nm). The crystal growth in the direction of thin film deposition is interrupted at regular intervals by amorphous layers of transition metal catalyst, resulting in highly ordered polycrystallinity in the growth direction. Although the recrystallisation of the transition metal interlayers produces finely distributed catalyst nanocrystallites, conducive to fast hydrogen storage kinetics, the separation of the magnesium layers is lost, leading to grain growth in the magnesium bulk up to an average grain size of ca. 100 nm.

6.2.2 Hydrogen Storage Kinetics

The structural evolution, as well as the elemental composition of the thin film multilayers was used to explain the fast hydrogen storage kinetics that were observed. A substantial reduction in the hydrogenation time of the catalysed thin film samples, compared with the non-catalysed $Mg_{control}$ sample was measured. The latter absorbed 80% of its maximum measured capacity (5.4 $\pm$ 0.2 wt%) in 36 minutes at 270°C, compared with as little as 2.5 minutes for the absorption of 90% of its maximum measured capacity for the Mg/TM (4.6 $\pm$ 0.2 wt%) sample at the same temperature. At the same temperature,

the Mg/Cr sample absorbed 80% of its maximum measured capacity (6.1 ± 0.3 wt%) in 7.5 minutes, whilst the Mg/V sample absorbed 80% of its maximum measured capacity (5.4 ± 0.3 wt%) in 10.4 minutes.

Given the identical processing conditions of all 4 samples, the improvements in hydrogenation kinetics at reduced temperatures for the three catalysed samples over the $Mg_{control}$ sample was explained in part by the catalytic effect of the transition metal elements that were included in the multilayer structures, forming high surface area nanocatalysts upon cycling. The reduced grain growth in these structures that was measured helped shorten and increase the number of diffusion pathways for hydrogen, since the hydrogenation rate was shown to be limited largely by diffusion.

This was further supported by the inclusion of the Mg_2Ni alloy-forming nickel in the Mg/TM multilayer structure vastly improving the hydrogenation kinetics compared with the chromium- and vanadium catalysed samples, resulting in hydrogenation times an order of magnitude shorter at 250°C. The literature suggests this might be a result of a favourable diffusion coefficient for the diffusion of hydrogen through Mg_2NiH_4 compared with MgH_2.

Similar results were shown for the dehydrogenation reaction. Although diffusion was shown to impact the reactions at the lower end of the temperature range which was used (250 – 350°C), the dehydrogenation reactions are affected largely by the choice of catalyst material. From the measurements of the dehydrogenation reaction rates and activation energies for the four samples it is clear that the inclusion of transition metal catalysts has a dramatic effect in improving both the dehydrogenation rates and activation energies for the release of hydrogen from the thin film structures. Impor-

tantly, it has been found that these results match closely with materials of similar composition found in the literature. Therefore, the processing and nano structuring employed in this work does not appear to affect the materials' hydrogen storage properties, making the technique a viable, versatile and highly controllable lab-scale method of producing novel hydrogen storage materials.

6.3 Future Work

Comparison of the structural evolution and hydrogen storage properties of the thin film structures presented in this work with structures of similar composition in the literature has shown that there are many similarities. This work expands the body of knowledge by investigating new elemental compositions of thin film materials and by pushing the limits of physical composition by including extremely thin, amorphous layers of transition metal catalysts between layers of magnesium.

The samples were compared in-depth with similar structures presented by Kalisvaart *et al.* (2011). The crucial difference lies in the recrystallisation of the transition metal interlayer which in this work leads to the formation of nanocrystallites and increased decrepitation of the sample into a fine flaky powder. Kalisvaart *et al.* (2011) did not however push the boundaries towards very thin layers of magnesium, which, in order to maintain a high hydrogen storage capacity, would result in extremely thin layers of transition metal as shown in this work.

Future work might therefore include exploring the possible effect of recrystallisation of the transition metal interlayers in magnesium multilayer

structures on the hydrogen storage properties, along with a comparison of different multilayer thicknesses. Similarly, the deposition of crystalline interlayers and in-situ crystallisation of the interlayers using a heater arrangement might shed more light on the benefits of the formation of nanocrystallites shown in this work. Furthermore, it is suggested that the formation of nanocrystalline catalyst particulates in this work is partially responsible for the decrepitation of the thin film structures and, as well as studying the hydrogen storage properties of amorphous, re-crystallised and in-situ-crystallised magnesium-transition metal multilayers, much might be learnt by studying the decrepitation process and to what extent the hydrogen storage properties are affected by the structural evolution of the transition metal interlayers. Similarly, the structural evolution of the magnesium phase might also provide an insight into potential future-generation thin film materials.

Section 2.2.6 shows a potential advantage of using co-sputtered thin film structures over multilayers. A comparison between co-sputtered structures of similar composition and the ones presented in this work might be beneficial to further understand the effect of multilayering on the hydrogen storage properties and structural evolution of micron-thick, transition metal-catalysed magnesium coatings.

6.3.1 Processing of Metal Hydrides

Having shown and discussed in-depth research on thin film multilayer structures with some promising results, and having suggested options for further development, the question remains how, if at all, this research may be used in commercial applications. Although the PVD coating process employed in

this work is ideal to produce gram-quantities of hydrogen storage material in 2 – 3 hours, on an industrial scale this seems highly impractical, given the financial constraints for a hydride store, exemplified in section 1.2.

Ball-milling, discussed in section 2.1.2, has the similar problem of being an effective lab-scale means of synthesising hydrogen storage materials with improved properties, but using this batch-manufacturing process for mass-production is not likely to be cost-efficient. Several other manufacturing processes have been proposed in an attempt to produce nanostructured hydrogen storage materials with similar levels of grain refinement to those achieved with ball-milling and thin film processes. These severe plastic deformation (SPD) processes include high-pressure torsion (HPT), equal channel angular pressing (ECAP) and cold rolling, all of which have been shown to have positive effects on the hydrogen storage behaviour of magnesium-based hydrogen storage materials (Huot, 2012; Vincent *et al.*, 2011). For mass-production, a continuous production process is favourable which is why much of the literature on alternative routes to nanostructured metal hydrides uses cold rolling to synthesise hydride materials.

6.3.2 Rolling

Lang and Huot (2011) compare the performance of magnesium hydride powders that have been cold rolled with both as-received magnesium hydride powders and ones that have been ball-milled, showing that cold rolling is an effective means of improving reaction kinetics in magnesium-based hydrogen storage materials. Bellemare and Huot (2012) and Vincent *et al.* (2011) show that this can be further improved by the addition of metal- and metal

oxide catalysts to magnesium hydride and cold colling the mixture 5 times, resulting in similar performance seen for the ball-milled systems described in section 2.1.2.

The main issue that was observed with these systems was the poor distribution of the catalyst material in the magnesium matrix which, as established in section 2.1.2, is strongly linked to the efficiency of a catalyst in magnesium-based hydride materials. The authors suggest that this might be improved with an increased number of rolling passes in an inert atmosphere, limiting the amount of oxidation and increasing the level of grain refinement, potentially further improving the reaction kinetics.

Layered structures have also been processed by cold rolling, in an accumulative roll-bonding (ARB) process. Magnesium-titanium and magnesium-stainless steel composites were produced by repeated folding and rolling of magnesium, titanium and stainless steel sheet (Danaie *et al.*, 2011). This produced composite materials with high levels of grain refinement. Using sheet metal has many advantages over powders from a manufacturing point of view, since this is what the cold rolling process is designed to produce and indeed, cold rolled powders consolidate into sheet-like material after a single rolling pass. Due to work hardening effects combined with different levels of ductility in the raw materials, different levels of plastic deformation in magnesium- and catalyst phases leads to 'islands' of catalyst material within the magnesium matrix, with no indication of nanostructuring or homogenisation in the elemental composition of the materials even after 90 folding and rolling operations.

Ueda *et al.* (2005) presents similar results for a magnesium-nickel compos-

ite produced by ARB. Upon heat-treatment at 350°C, the 'islands' of nickel that are formed within the magnesium matrix react with the surrounding magnesium, forming Mg_2Ni, with improved reaction kinetics over cast materials of similar composition.

6.3.3 Rolling Second-Generation Hydrides Using the Mg/TM System

Using the lessons learnt from the thin films study presented in this work and the literature on SPD processing of magnesium-based hydrogen storage materials, promising prospects might be found in combining thin film techniques with SPD techniques to create second generation composites with improved properties, one step closer to the mass-production of affordable, high-capacity hydrogen storage materials with improved reaction kinetics.

Initial experiments have shown that the low ductility of magnesium hydride compared with magnesium leads to the high levels of grain refinement that has been reported in the literature with a crystallite size of 31.3 ± 0.4 nm (Lang and Huot, 2011) for the hydride and 15 μm for the metal (Chang *et al.*, 2010). By mixing magnesium with a brittle phase such as Mg_2Ni, Skripnyuk *et al.* (2007) managed to reduce the grain size of the metallic magnesium phase to a nanometer scale using an ECAP process. This was shown to have a positive effect on accelerating the hydrogenation kinetics of this eutectic magnesium-Mg_2Ni alloy.

The results of this work suggests that the formation of Mg_2Ni is beneficial for fast hydrogen diffusion into the expanding hydride phase, whilst transition metal catalysts have a significant impact on the actual reaction

kinetics. Since the presence of a brittle Mg_2Ni phase promotes grain refinement in magnesium processed by SPD, another important factor for fast hydrogen storage kinetics, it makes sense to combine the findings to develop a system based on a transition-metal catalysed Mg-Mg_2Ni composite which can be processed by SPD techniques, enabling economical, industrial-scale production.

By rolling metallic magnesium and nickel, sheet metal processing rather than powder processing might be possible. Hot rolling in an inert atmosphere might prevent work-hardening, avoiding rolling defects and promoting Mg_2Ni alloy formation between the magnesium and nickel phases. This improves the catalyst distribution that first-generation cold rolled hydrides suffer from (Vincent *et al.*, 2011), whilst producing a brittle phase that promotes grain refinement in a cold rolling process that might follow.

By rolling magnesium with nickel-alloys such as NiCr, this might produce a transition-metal catalysed Mg-Mg_2Ni nano-composite with hydrogen storage properties similar to those observed for the Mg/TM thin film presented in this work.

The role of thin film technologies remains not only in the lab for testing novel compositions of different materials, but has potential to play a part in such an ARB process. It might prove beneficial to coat thin magnesium sheet with alloys such as NiCr in order to achieve improved laminate structures since the compositions required for high hydrogen storage capacities will require a high ratio of thickness between the two materials. Thin film technology might allow much thinner magnesium sheet to be used leading to higher levels of homogenisation in the finished product.

Bibliography

Aceves, S. M., Espinosa-Loza, F., Ledesma-Orozco, E., Ross, T. O., Weisberg, A. H., Brunner, T. C., and Kircher, O. (2010). High-density automotive hydrogen storage with cryogenic capable pressure vessels. *International Journal of Hydrogen Energy*, **35**(3), 1219–1226.

Akyildiz, H., Ozenbas, M., and Ozturk, T. (2006). Hydrogen absorption in magnesium based crystalline thin films. *International Journal of Hydrogen Energy*, **31**(10), 1379–1383.

Amann, W., Eisner, W., Gietz, P., Maier, J., Schierle, W., and Stein, R. (1989). Elemente Chemie II. *Ernst Klett Schulbuchverlag, Stuttgart*.

Amirkhiz, B. S., Danaie, M., and Mitlin, D. (2009). The influence of SWCNT–metallic nanoparticle mixtures on the desorption properties of milled MgH_2 powders. *Nanotechnology*, **20**(20), 204016.

Andreasen, A. (2004). Predicting formation enthalpies of metal hydrides.

Andreasen, A., Vegge, T., and Pedersen, A. S. (2005). Compensation Effect in the Hydrogenation/Dehydrogenation Kinetics of Metal Hydrides. *J. Phys. Chem. B*, **109**(8), 3340–3344.

Atias-Adrian, I. C., Deorsola, F. A., Ortigoza-Villalba, G. A., DeBenedetti, B., and Baricco, M. (2013). Development of nanostructured Mg_2Ni alloys for hydrogen storage applications. *International Journal of Hydrogen Energy*, **36**(13), 7897–7901.

Baldi, A. and Dam, B. (2011). Thin film metal hydrides for hydrogen storage applications. *J. Mater. Chem.*, **21**(12), 4021.

Baldi, A., Gonzalez-Silveira, M., Palmisano, V., Dam, B., and Griessen, R. (2009a). Destabilization of the Mg-H System through Elastic Constraints. *Phys. Rev. Lett.*, **102**(22).

Baldi, A., Gremaud, R., Borsa, D. M., Balde, C. P., van der Eerden, A. M. J., Kruijtzer, G. L., de Jongh, P. E., Dam, B., and Griessen, R. (2009b). Nanoscale composition modulations in $Mg_yTi_{1-y}H_x$ thin film alloys for hydrogen storage. *International Journal of Hydrogen Energy*, **34**(3), 1450–1457.

Baldi, A., Palmisano, V., Gonzalez-Silveira, M., Pivak, Y., Slaman, M., Schreuders, H., Dam, B., and Griessen, R. (2009c). Quasifree Mg–H thin films. *Appl. Phys. Lett.*, **95**(7), 071903.

Baldi, A., Pálsson, G., Gonzalez-Silveira, M., Schreuders, H., Slaman, M., Rector, J. H., Krishnan, G., Kooi, B. J., Walker, G. S., and Fay, M. W. (2010). Mg/Ti multilayers: Structural and hydrogen absorption properties. *Phys. Rev. B*, **81**(22), 224203.

Bao, S., Yamada, Y., Okada, M., and Yoshimura, K. (2006). Titanium-Buffer-Layer-Inserted Switchable Mirror Based on Mg-Ni Alloy Thin Film. *Jpn. J. Appl. Phys.*, **45**(No. 23), L588–L590.

Barcelo, S., Rogers, M., Grigoropoulos, C. P., and Mao, S. S. (2010). Hydrogen storage property of sandwiched magnesium hydride nanoparticle thin film. *International Journal of Hydrogen Energy*, **35**(13), 7232–7235.

Barkhordarian, G., Klassen, T., and Bormann, R. (2004). Effect of Nb_2O_5 content on hydrogen reaction kinetics of Mg. *Journal of Alloys and Compounds*, **364**(1-2), 242–246.

Barkhordarian, G., Klassen, T., and Bormann, R. (2006). Kinetic investigation of the effect of milling time on the hydrogen sorption reaction of magnesium catalyzed with different Nb_2O_5 contents. *Journal of Alloys and Compounds*, **407**(1-2), 249–255.

Bazzanella, N., Checchetto, R., and Miotello, A. (2011). Atoms and Nanoparticles of Transition Metals as Catalysts for Hydrogen Desorption from Magnesium Hydride. *Journal of Nanomaterials*, **2011**(2), 1–11.

Bellemare, J. and Huot, J. (2012). Hydrogen storage properties of cold rolled magnesium hydrides with oxides catalysts. *Journal of Alloys and Compounds*, **512**(1), 33–38.

Berry, G. D. and Aceves, S. M. (1998). Onboard storage alternatives for hydrogen vehicles. *Energy & fuels*, **12**(1), 49–55.

Berube, V., Radtke, G., Dresselhaus, M., and Chen, G. (2007). Size effects on the hydrogen storage properties of nanostructured metal hydrides: A review. *Int. J. Energy Res.*, **31**(6-7), 637–663.

Berube, V., Chen, G., and Dresselhaus, M. S. (2008). Impact of nanostructuring on the enthalpy of formation of metal hydrides. *International Journal of Hydrogen Energy*, **33**(15), 4122–4131.

Blawert, C., Manova, D., Störmer, M., Gerlach, J. W., Dietzel, W., and Mändl, S. (2008). Correlation between texture and corrosion properties of magnesium coatings produced by PVD. *Surface and Coatings Technology*, **202**(11), 2236–2240.

Bobet, J., Grigorova, E., Khrussanova, M., Khristov, M., Radev, D., and Peshev, P. (2002). Hydrogen sorption properties of the nanocomposites Mg–$Mg_2Ni_{1-x}Fe_x$. *Journal of Alloys and Compounds*, **345**(1), 280–285.

Bogdanovic, B. and Schwickardi, M. (1997). Ti-doped alkali metal aluminium hydrides as potential novel reversible hydrogen storage materials. In *J Alloy Compd*, pages 1–9.

Bogdanovic, B., Bohmhammel, K., Christ, B., Reiser, A., Schlichte, K., Vehlen, R., and Wolf, U. (1999). Thermodynamic investigation of the magnesium-hydrogen system. *Journal of Alloys and Compounds*, **282**, 84–92.

Bossel, U. (2006). Does a Hydrogen Economy Make Sense? *Proc. IEEE*, **94**(10), 1826–1837.

Bouaricha, S., Dodelet, J. P., Guay, D., Huot, J., and Schulz, R. (2001). Activation characteristics of graphite modified hydrogen absorbing materials. *Journal of Alloys and Compounds*, **325**(1), 245–251.

Bystrzycki, J., Czujko, T., and Varin, R. (2005). Processing by controlled mechanical milling of nanocomposite powders Mg + X (X = Co, Cr, Mo, V, Y, Zr) and their hydrogenation properties. *Journal of Alloys and Compounds*, **404-406**, 507–510.

Callister, W. D. and Rethwisch, D. G. (2011). *Fundamentals of materials science and engineering: an integrated approach (hardback)*. Wiley.

Čermák, J. and Král, L. (2008). Hydrogen diffusion in Mg–H and Mg–Ni–H alloys. *Acta Materialia*, **56**(12), 2677–2686.

Chang, H., Zheng, M. Y., Wu, K., Gan, W. M., Tong, L. B., and Brokmeier, H. G. (2010). Microstructure and mechanical properties of the accumulative roll bonded (ARBed) pure magnesium sheet. *Materials Science and Engineering: A*, **527**(27-28), 7176–7183.

Chen, J., Yang, H.-B., Xia, Y.-Y., Kuriyama, N., Xu, Q., and Sakai, T. (2002). Hydriding and Dehydriding Properties of Amorphous Magnesium-Nickel Films Prepared by a Sputtering Method. *Chem. Mater.*, **14**(7), 2834–2836.

Croston, D. L., Grant, D. M., and Walker, G. S. (2010). The catalytic effect of titanium oxide based additives on the dehydrogenation and hydrogenation of milled MgH_2. *Journal of Alloys and Compounds*, **492**(1-2), 251–258.

Cullity, B. D. and Stock, S. R. (2001). *Elements of X-ray Diffraction*, volume 3. Prentice hall Upper Saddle River, NJ.

Dai, B., Karl Johnson, J., and Sholl, D. S. (2009). Assessing nanoparticle size effects on metal hydride thermodynamics using the Wulff construction. *Nanotechnology*, **20**(20), 204001.

Dal Toè, S., Lo Russo, S., Maddalena, A., Principi, G., Saber, A., Sartori, S., and Spataru, T. (2004). Hydrogen desorption from magnesium hydride–graphite nanocomposites produced by ball milling. *Materials Science and Engineering B*, **108**(1-2), 24–27.

Dam, B., Gremaud, R., Broedersz, C., and Griessen, R. (2007). Combinatorial thin film methods for the search of new lightweight metal hydrides. *Scripta Materialia*, **56**(10), 853–858.

Danaie, M., Mauer, C., Mitlin, D., and Huot, J. (2011). Hydrogen storage in bulk Mg-Ti and Mg-stainless steel multilayer composites synthesized via accumulative roll-bonding (ARB). *International Journal of Hydrogen Energy*, **36**(4), 3022–3036.

Dehouche, Z., Klassen, T., Oelerich, W., Goyette, J., Bose, T., and Schulz, R. (2002). Cycling and thermal stability of nanostructured MgH_2-Cr_2O_3 composite for hydrogen storage. *Journal of Alloys and Compounds*, **347**(1-2), 319–323.

DTI, U. K. (2003). Energy White Paper: Our energy future–creating a low carbon economy. *DTI, London*.

Dufour, J. and Huot, J. (2007). Study of Mg_6Pd alloy synthesized by cold rolling. *Journal of Alloys and Compounds*, **446-447**, 147–151.

Eberle, U., Felderhoff, M., and Schüth, F. (2009). Chemical and Physical Solutions for Hydrogen Storage. *Angew. Chem. Int. Ed.*, **48**(36), 6608–6630.

Eckert, J., Holzer, J. C., Ahn, C. C., Fu, Z., and Johnson, W. L. (1993). Melting behavior of nanocrystalline aluminum powders. *Nanostructured materials*, **2**(4), 407–413.

Edwards, P. P., Kuznetsov, V. L., David, W. I. F., and Brandon, N. P. (2008). Hydrogen and fuel cells: Towards a sustainable energy future. *Energy Policy*, **36**(12), 4356–4362.

Eigen, N., Keller, C., Dornheim, M., Klassen, T., and Bormann, R. (2007). Industrial production of light metal hydrides for hydrogen storage. *Scripta Materialia*, **56**(10), 847–851.

Ellinger, F. H., Holley, Jr, C. E., McInteer, B. B., Pavone, D., Potter, R. M., Staritzky, E., and Zachariasen, W. H. (1955). The Preparation and Some Properties of Magnesium Hydride. *J Am Chem Soc*, **77**(9), 2647–2648.

European Commission and others (2013). The renewable energy progress report. *SWD (2009)*, **503**.

Fleischer, M. (1954). The abundance and distribution of the chemical elements in the earth's crust. *Journal of Chemical Education*, **31**(9), 446.

Fritzsche, H., Ophus, C., Harrower, C. T., Luber, E., and Mitlin, D. (2009). Low temperature hydrogen desorption in MgAl thin films achieved by using a nanoscale Ta/Pd bilayer catalyst. *Appl. Phys. Lett.*, **94**(24), 241901.

Fritzsche, H., Kalisvaart, W. P., Zahiri, B., Flacau, R., and Mitlin, D. (2012). The catalytic effect of Fe and Cr on hydrogen and deuterium absorption in Mg thin films. *International Journal of Hydrogen Energy*, **37**(4), 3540–3547.

Fry, C. M. P., Grant, D. M., and Walker, G. S. (2013). Improved hydrogen cycling kinetics of nano-structured magnesium/transition metal multilayer thin films. *International Journal of Hydrogen Energy*, **38**(2), 982–990.

Gencoa Ltd. (2013). Gencoa Sputter Rate Calculator.

Ghosh, G. and Olson, G. B. (2000). Thermodynamic modeling of the Cr-Pd and Mo-Pd systems. *Journal of phase equilibria*, **21**(1), 32–39.

Ghosh, G., Kantner, C., and Olson, G. B. (1999). Thermodynamic modeling of the Pd-X (X= Ag, Co, Fe, Ni) systems. *Journal of phase equilibria*, **20**(3), 295–308.

Gladman, T. (1966). On the theory of the effect of precipitate particles on grain growth in metals. *Proceedings of the Royal Society of London. Series A. Mathematical and Physical Sciences*, **294**(1438), 298–309.

Great Britain (2008). Climate Change Act 2008.

Grochala, W. and Edwards, P. P. (2004). Thermal Decomposition of the Non-Interstitial Hydrides for the Storage and Production of Hydrogen. *Chem. Rev.*, **104**(3), 1283–1316.

Gross, K. J., Carrington, K. R., Barcelo, S., Karkamkar, A., Purewal, J., and Parilla, P. (2008). Recommended Best Practices for the Characterization of Storage Properties of Hydrogen Storage Materials.

Hall, W. H. (1949). X-ray line broadening in metals. *Proceedings of the Physical Society. Section A*, **62**(11), 741.

Hanada, N., Ichikawa, T., Orimo, S.-I., and Fujii, H. (2004). Correlation between hydrogen storage properties and structural characteristics in mechanically milled magnesium hydride MgH_2. *Journal of Alloys and Compounds*, **366**(1-2), 269–273.

Hanada, N., Ichikawa, T., and Fujii, H. (2005). Catalytic Effect of Nanoparticle 3d-Transition Metals on Hydrogen Storage Properties in Magnesium Hydride MgH_2 Prepared by Mechanical Milling. *J. Phys. Chem. B*, **109**(15), 7188–7194.

He, Y., Fan, J., and Zhao, Y. (2010). The role of differently distributed vanadium nanocatalyst in the hydrogen storage of magnesium nanostructures. *International Journal of Hydrogen Energy*, **35**(9), 4162–4170.

Heung, L. and Stamford, C. (2003). Using metal hydride to store hydrogen. *US Department of Energy*, pages 1–9.

Higuchi, K., Kajioka, H., Toiyama, K., Fujii, H., Orimo, S., and Kikuchi, Y. (1999). In situ study of hydriding-dehydriding properties in some Pd/Mg thin films with different degree of Mg crystallization. *Journal of Alloys and Compounds*, **293**, 484–489.

Higuchi, K., Yamamoto, K., Kajioka, H., Toiyama, K., Honda, M., Orimo, S., and Fujii, H. (2002). Remarkable hydrogen storage properties in three-layered Pd/Mg/Pd thin films. *Journal of Alloys and Compounds*, **330**, 526–530.

Hjort, P., Krozer, A., and Kasemo, B. (1996). Hydrogen sorption kinetics in partly oxidized Mg films. *Journal of Alloys and Compounds*, **237**(1-2), 74–80.

Holtz, R. and Imam, M. (1999). Hydrogen storage characteristics of ball-milled magnesium-nickel and magnesium-iron alloys. *J Mater Sci*, **34**(11), 2655–2663.

Hu, Y. Q., Zhang, H. F., Wang, A. M., Ding, B. Z., and Hu, Z. Q. (2003). Preparation and hydriding/dehydriding properties of mechanically milled Mg–30 wt% $TiMn_{1.5}$ composite. *Journal of Alloys and Compounds*, **354**(1), 296–302.

Huhn, P. A., Dornheim, M., Klassen, T., and Bormann, R. (2005). Thermal stability of nanocrystalline magnesium for hydrogen storage. *Journal of Alloys and Compounds*, **404-406**, 499–502.

Huot, J. (2012). Nanocrystalline Metal Hydrides Obtained by Severe Plastic Deformations. *Metals*.

Huot, J., Akiba, E., and Takada, T. (1995). Mechanical alloying of Mg-Ni compounds under hydrogen and inert atmosphere. *Journal of Alloys and Compounds*, **231**(1), 815–819.

Huot, J., Liang, G., Boily, S., Van Neste, A., and Schulz, R. (1999). Structural study and hydrogen sorption kinetics of ball-milled magnesium hydride. *Journal of Alloys and Compounds*, **293**, 495–500.

Huot, J., Pelletier, J. F., Liang, G., Sutton, M., and Schulz, R. (2002). Structure of nanocomposite metal hydrides. *Journal of Alloys and Compounds*, **330**, 727–731.

Huot, J., Ravnsbæk, D. B., Zhang, J., Cuevas, F., Latroche, M., and Jensen, T. R. (2013). Mechanochemical synthesis of hydrogen storage materials. *Progress in Materials Science*, **58**(1), 30–75.

Infomine (2013a). Magnesium Prices and Magnesium Price Charts.

Infomine (2013b). Palladium Prices and Palladium Price Charts.

Infomine (2013c). Vanadium Prices and Magnesium Price Charts.

Ingason, A. S. and Olafsson, S. (2006). Influence of MgO nano-crystals on the thermodynamics, hydrogen uptake and kinetics in Mg films. *Thin Solid Films*, **515**(2), 708–711.

Jain, I. P., Lal, C., and Jain, A. (2010). Hydrogen storage in Mg: A most promising material. *International Journal of Hydrogen Energy*, **35**(10), 5133–5144.

Jensen, J., Andreasen, A., Vegge, T., Andreasen, J., Stahl, K., Pedersen, A., Nielsen, M., Molenbroek, A., and Besenbacher, F. (2006). Dehydrogenation kinetics of pure and nickel-doped magnesium hydride investigated by in situ time-resolved powder X-ray diffraction. *International Journal of Hydrogen Energy*, **31**(14), 2052–2062.

Jolibois, P. (1912). Study of pure magnesium and magnesium hydrides. *Compt. Rend. Acad. Sci. Paris*, **155**, 353–355.

Jung, K. S., Lee, E. Y., and Lee, K. S. (2006). Catalytic effects of metal oxide on hydrogen absorption of magnesium metal hydride. *Journal of Alloys and Compounds*, **421**(1-2), 179–184.

Kalisvaart, W. P., Harrower, C. T., Haagsma, J., Zahiri, B., Luber, E. J., Ophus, C., Poirier, E., Fritzsche, H., and Mitlin, D. (2010). Hydrogen storage in binary and ternary Mg-based alloys: A comprehensive experimental study. *International Journal of Hydrogen Energy*, **35**(5), 2091–2103.

Kalisvaart, W. P., Kubis, A., Danaie, M., Amirkhiz, B. S., and Mitlin, D. (2011). Microstructural evolution during hydrogen sorption cycling of Mg-FeTi nanolayered composites. *Acta Materialia*, **59**(5), 2083–2095.

Kalisvaart, W. P., Luber, E. J., Poirier, E., Harrower, C. T., Teichert, A., Wallacher, D., Grimm, N., Steitz, R., Fritzsche, H., and Mitlin, D. (2012). Probing the Room Temperature Deuterium Absorption Kinetics in Nanoscale Magnesium Based Hydrogen Storage Multilayers Using Neutron Reflectometry, X-ray Diffraction, and Atomic Force Microscopy. *J. Phys. Chem. C*, page 120227104754004.

Kelly, P. and Arnell, R. (2000). Magnetron sputtering: a review of recent developments and applications. *Vacuum*, **56**(3), 159–172.

Kelton, K. F. (1997). Analysis of crystallization kinetics. *Materials Science and Engineering: A*, **226**, 142–150.

Khawam, A. and Flanagan, D. R. (2006). Solid-State Kinetic Models: Basics and Mathematical Fundamentals. *J. Phys. Chem. B*, **110**(35), 17315–17328.

Kissinger, H. E. (1956). Variation of peak temperature with heating rate in differential thermal analysis. *Journal of Research of the National Bureau of Standards*, **57**(4), 217–221.

Klug, H. and Alexander, L. (1974). X-Ray Diffraction Procedures. Mellon Institute of Science.

Lang, J. and Huot, J. (2011). A new approach to the processing of metal hydrides. *Journal of Alloys and Compounds*, **509**(3), L18–L22.

Léon, A., Knystautas, E. J., Huot, J., and Schulz, R. (2002). Hydrogenation characteristics of air-exposed magnesium films. *Journal of Alloys and Compounds*, **345**(1), 158–166.

Liang, G., Boily, S., Huot, J., Van Neste, A., and Schulz, R. (1998). Mechanical alloying and hydrogen absorption properties of the Mg–Ni system. *Journal of Alloys and Compounds*, **267**(1), 302–306.

Liang, G., Huot, J., Boily, S., Van Neste, A., and Schulz, R. (1999a). Catalytic effect of transition metals on hydrogen sorption in nanocrystalline ball milled MgH_2-Tm (Tm=Ti, V, Mn, Fe and Ni) systems. *Journal of Alloys and Compounds*, **292**(1-2), 247–252.

Liang, G., Huot, J., Boily, S., Van Neste, A., and Schulz, R. (1999b). Hydrogen storage properties of the mechanically milled MgH_2-V nanocomposite. *Journal of Alloys and Compounds*, **291**, 295–299.

Liang, G., Huot, J., Boily, S., and Schulz, R. (2000). Hydrogen desorption kinetics of a mechanically milled MgH_2 + 5at.% V nanocomposite. *Journal of Alloys and Compounds*, **305**(1), 239–245.

Lu, J. J., Choi, Y. J. Y., Fang, Z. Z. Z., Sohn, H. Y. H., and Rönnebro, E. E. (2009). Hydrogen storage properties of nanosized MgH_2-$0.1TiH_2$ prepared by ultrahigh-energy-high-pressure milling. *J Am Chem Soc*, **131**(43), 15843–15852.

MacKay, D. J. C. (2009). Sustainable Energy.

Mintz, M. H. and Zeiri, Y. (1994). Hydriding kinetics of powders. *Journal of Alloys and Compounds*, **216**(2), 159–175.

Mitchell, P. C. H., Ramirez-Cuesta, A. J., Parker, S. F., Tomkinson, J., and Thompsett, D. (2003). Hydrogen Spillover on Carbon-Supported Metal Catalysts Studied by Inelastic Neutron Scattering. Surface Vibrational States and Hydrogen Riding Modes. *J. Phys. Chem. B*, **107**(28), 6838–6845.

Montone, A., Aurora, A., Gattia, D. M., and Antisari, M. V. (2012). Microstructural and Kinetic Evolution of Fe Doped MgH_2 during H_2 Cycling. *Catalysts*, **2**(3), 400–411.

Murray, P. and White, J. (1955). Kinetics of the thermal dehydration of clays. Part IV. Interpretation of the differential thermal analysis of the clay minerals. *Trans Brot Ceram Soc.*

Niessen, R. A. H. and Notten, P. H. L. (2005). Electrochemical Hydrogen Storage Characteristics of Thin Film MgX (X=Sc,Ti,V,Cr) Compounds. *Electrochem. Solid-State Lett.*, **8**(10), A534.

Nijkamp, M. G., Raaymakers, J. E. M. J., van Dillen, A. J., and de Jong, K. P. (2001). Hydrogen storage using physisorption – materials demands. *Appl Phys A*, **72**(5), 619–623.

NIST (2009). Database of the Thermophysical Properties of Gases Used in the Semiconductor Industry.

Oelerich, W., Klassen, T., and Bormann, R. (2001). Metal oxides as catalysts for improved hydrogen sorption in nanocrystalline Mg-based materials. *Journal of Alloys and Compounds*, **315**(1), 237–242.

Ohring, M. (2002). *Materials science of thin films*. Academic press, San Diego.

Orimo, S., Nakamori, Y., Kitahara, G., Miwa, K., Ohba, N., Towata, S., and Züttel, A. (2005). Dehydriding and rehydriding reactions of $LiBH_4$. *Journal of Alloys and Compounds*, **404-406**, 427–430.

Ouyang, L. Z., Wang, H., Chung, C. Y., Ahn, J. H., and Zhu, M. (2006). MgNi/Pd multilayer hydrogen storage thin films prepared by dc magnetron sputtering. *Journal of Alloys and Compounds*, **422**(1-2), 58–61.

Ozawa, T. C. and Kang, S. J. (2004). Balls&Sticks: easy-to-use structure visualization and animation program. *Journal of Applied Crystallography*, **37**(4), 679–679.

Paik, B., Walton, A., Mann, V., Book, D., Jones, I. P., and Harris, I. R. (2010). Microstructure of ball milled MgH_2 powders upon hydrogen cycling: An electron microscopy study. *International Journal of Hydrogen Energy*, **35**(17), 9012–9020.

Patel, N., Kale, A., Mosaner, P., Checchetto, R., Miotello, A., and Das, G. (2008). Deuterium thermal desorption from Ni-rich deuterated Mg thin films. *Renewable Energy*, **33**(2), 232–236.

Pelletier, J., Huot, J., Sutton, M., Schulz, R., Sandy, A., Lurio, L., and Mochrie, S. (2001). Hydrogen desorption mechanism in MgH_2-Nb nanocomposites. *Phys. Rev. B*, **63**(5), 052103.

Penning, F. M. and Moubis, J. (1940). Cathode sputtering in a magnetic field. *Koninkl. Ned. Akad. Wetenschop, Proc*, **43**(1), 41–56.

Qu, J., Wang, Y., Xie, L., Zheng, J., Liu, Y., and Li, X. (2009a). Hydrogen absorption-desorption, optical transmission properties and annealing effect of Mg thin films prepared by magnetron sputtering. *International Journal of Hydrogen Energy*, **34**(4), 1910–1915.

Qu, J., Wang, Y., Xie, L., Zheng, J., Liu, Y., and Li, X. (2009b). Superior hydrogen absorption and desorption behavior of Mg thin films. *Journal of Power Sources*, **186**(2), 515–520.

Qu, J., Sun, B., Yang, R., Zhao, W., Wang, Y., and Li, X. (2010a). Hydrogen absorption kinetics of Mg thin films under mild conditions. *Scripta Materialia*, **62**(5), 317–320.

Qu, J., Sun, B., Zheng, J., Yang, R., Wang, Y., and Li, X. (2010b). Hydrogen desorption properties of Mg thin films at room temperature. *Journal of Power Sources*, **195**(4), 1190–1194.

Qu, J., Sun, B., Liu, Y., Yang, R., Li, Y., and Li, X. (2010c). Improved hydrogen storage properties in Mg-based thin films by tailoring structures. *International Journal of Hydrogen Energy*, **35**(15), 8331–8336.

Reilly, J. J. and Wiswall, R. H. (1967). Reaction of hydrogen with alloys of magnesium and copper. *Inorganic Chemistry*, **6**(12), 2220–2223.

Reilly, J. J. and Wiswall, R. H. (1968). Reaction of hydrogen with alloys of magnesium and nickel and the formation of Mg_2NiH_4. *Inorganic Chemistry*, **7**(11), 2254–2256.

Richardson, T., Slack, J., Armitage, R., Kostecki, R., Farangis, B., and Rubin, M. (2001). Switchable mirrors based on nickel–magnesium films. *Appl. Phys. Lett.*, **78**(20), 3047.

Richardson, T., Slack, J., Farangis, B., and Rubin, M. (2002). Mixed metal films with switchable optical properties. *Appl. Phys. Lett.*, **80**(8), 1349.

Rousseau, A. and Sharer, P. (2004). Comparing Apples to Apples – Well-to-Wheel Analysis of Current ICE and Fuel Cell Vehicle Technologies. pages 1–21.

Sakintuna, B., Lamaridarkrim, F., and Hirscher, M. (2007). Metal hydride materials for solid hydrogen storage: A review. *International Journal of Hydrogen Energy*, **32**(9), 1121–1140.

San-Martin, A. and Manchester, F. D. (1987). The H-Mg (Hydrogen-Magnesium) system. *Journal of phase equilibria*, **8**(5), 431–437.

Sanders, D. M. and Anders, A. (2000). Review of cathodic arc deposition technology at the start of the new millennium. *Surface and Coatings Technology*, **133**, 78–90.

Sandí, G. (2004). Hydrogen storage and its limitations. *Interface*, **13**(3), 40–44.

Sandrock, G. (1999). A panoramic overview of hydrogen storage alloys from a gas reaction point of view. *Journal of Alloys and Compounds*, **293**, 877–888.

Singh, S., Eijt, S. W. H., Zandbergen, M. W., Legerstee, W. J., and Svetchnikov, V. L. (2007). Nanoscale structure and the hydrogenation of Pd-capped magnesium thin films prepared by plasma sputter and pulsed laser deposition. *Journal of Alloys and Compounds*, **441**(1-2), 344–351.

Siviero, G., Bello, V., Mattei, G., Mazzoldi, P., Battaglin, G., Bazzanella, N., Checchetto, R., and Miotello, A. (2009). Structural evolution of Pd-capped Mg thin films under H_2 absorption and desorption cycles. *International Journal of Hydrogen Energy*, **34**(11), 4817–4826.

Skripnyuk, V., Buchman, E., Rabkin, E., Estrin, Y., Popov, M., and Jorgensen, S. (2007). The effect of equal channel angular pressing on hydrogen storage properties of a eutectic Mg–Ni alloy. *Journal of Alloys and Compounds*, **436**(1-2), 99–106.

Smith, D. K. and Jenkins, R. (1996). The powder diffraction file: past, present, and future. *Journal of research of the National Institute of Standards and Technology*, **101**(3).

Sree Harsha, K. S. (2005). *Principles of Vapor Deposition of Thin Films*. Elsevier Science.

Stampfer, Jr, J. F., Holley, Jr, C. E., and Suttle, J. F. (1960). The Magnesium-Hydrogen System. *J Am Chem Soc*, **82**(14), 3504–3508.

Störmer, M., Blawert, C., Hagen, H., Heitmann, V., and Dietzel, W. (2007). Structure and Corrosion of Magnetron Sputtered Pure Mg Films on Silicon Substrates. *Plasma Process. Polym.*, **4**(S1), S557–S561.

Sun, N. X., Liu, X. D., and Lu, K. (2003). An explanation to the anomalous avrami exponent. *Scripta Materialia*, **34**(8), 1201–1207.

Tajima, K., Yamada, Y., Bao, S., Okada, M., and Yoshimura, K. (2009). Clear transparency all-solid-state switchable mirror with Mg–Ti thin film on polymer sheet. *Solar Energy Materials and Solar Cells*, **93**(12), 2083–2087.

Tan, X., Harrower, C. T., Amirkhiz, B. S., and Mitlin, D. (2009). Nano-scale bi-layer Pd/Ta, Pd/Nb, Pd/Ti and Pd/Fe catalysts for hydrogen sorption in magnesium thin films. *International Journal of Hydrogen Energy*, **34**(18), 7741–7748.

Tan, Z., Chiu, C., Heilweil, E. J., and Bendersky, L. A. (2011). Thermodynamics, kinetics and microstructural evolution during hydrogenation of iron-doped magnesium thin films. *International Journal of Hydrogen Energy*, **36**(16), 9702–9713.

Tanniru, M., Slattery, D. K., and Ebrahimi, F. (2010). A study of stability of MgH_2 in Mg-8 at.% Al alloy powder. *International Journal of Hydrogen Energy*, **35**(8), 3555–3564.

Tsai, R.-Y. (1989). The Microstructures of Devitrified Amorphous Chromium Plating. *J. Electrochem. Soc.*, **136**(5), 1341.

Tsuchiya, H. (2004). Mass production cost of PEM fuel cell by learning curve. *International Journal of Hydrogen Energy*, **29**(10), 985–990.

Ueda, T. T., Tsukahara, M., Kamiya, Y., and Kikuchi, S. (2005). Preparation and hydrogen storage properties of Mg–Ni–Mg_2Ni laminate composites. *Journal of Alloys and Compounds*, **386**(1-2), 253–257.

UK DECC (2009). Digest of UK Energy Statistics 2009. pages 1–402.

UK DECC (2013). 2012 UK Greenhouse Gas Emissions, Providional Figures and 2011 UK Greenhouse Gas Emissions, Final Figures by Fuel-Type and End-User. pages 1–33.

Urbassek, H. M. and Hofer, W. O. (1993). Sputtering of molecules and clusters: Basic experiments and theory. *Mat. Fys. Medd. K. Dan Vidensk. Selsk*, **43**, 97–125.

US DOE (2009). Targets for Onboard Hydrogen Storage Systems for Light-Duty Vehicles. pages 1–22.

US DOE (2013). Hydride Information Center.

Vajo, J. J. (2011). Influence of nano-confinement on the thermodynamics and dehydrogenation kinetics of metal hydrides. *Current Opinion in Solid State and Materials Science*, **15**(2), 52–61.

Vajo, J. J., Mertens, F., Ahn, C. C., Bowman, R. C., and Fultz, B. (2004). Altering Hydrogen Storage Properties by Hydride Destabilization through Alloy Formation: LiH and MgH_2 Destabilized with Si. *J. Phys. Chem. B*, **108**(37), 13977–13983.

Varin, R., Czujko, T., Chiu, C., and Wronski, Z. (2006a). Particle size effects on the desorption properties of nanostructured magnesium dihydride (MgH_2) synthesized by controlled reactive mechanical milling (CRMM). *Journal of Alloys and Compounds*, **424**(1-2), 356–364.

Varin, R., Czujko, T., and Wronski, Z. (2006b). Particle size, grain size and γ-Mg_2 effects on the desorption properties of nanocrystalline commercial magnesium hydride processed by controlled mechanical milling. *Nanotechnology*, **17**(15), 3856–3865.

Varin, R., Czujko, T., and Wronski, Z. S. (2008). *Nanomaterials for solid state hydrogen storage*. Springer Verlag.

Varin, R. A., Zbroniec, L., Polanski, M., and Bystrzycki, J. (2011). A Review of Recent Advances on the Effects of Microstructural Refinement and Nano-Catalytic Additives on the Hydrogen Storage Properties of Metal and Complex Hydrides. *Energies*, **4**(1), 1–25.

Vigeholm, B., Kjøller, J., Larsen, B., and Pedersen, A. S. (1983). Formation and decomposition of magnesium hydride. *J Less-Common Met*, **89**(1), 135–144.

Vincent, S. D., Lang, J., and Huot, J. (2011). Addition of catalysts to magnesium hydride by means of cold rolling. *Journal of Alloys and Compounds*.

Von Zeppelin, F., Reule, H., and Hirscher, M. (2002). Hydrogen desorption kinetics of nanostructured MgH_2 composite materials. *Journal of Alloys and Compounds*, **330**, 723–726.

Walker, G. (2008). *Solid-state hydrogen storage: materials and chemistry*. Woodhead Publishing.

Walker, G. S., Abbas, M., Grant, D. M., and Udeh, C. (2011). Destabilisation of magnesium hydride by germanium as a new potential multicomponent hydrogen storage system. *Chem. Commun.*, **47**(28), 8001.

Wang, P., Wang, A. M., Ding, B. Z., and Hu, Z. Q. (2002). Mg–$FeTi_{1.2}$ (amorphous) composite for hydrogen storage. *Journal of Alloys and Compounds*, **334**(1), 243–248.

Wang, Y., Hua, W., Qu, J., Xie, L., and Li, X. (2008). Structure changes and optical properties of Mg_2Ni switchable mirrors. *International Journal of Hydrogen Energy*, **33**(23), 7207–7213.

Wehner, G. K. (1955). Sputtering by ion bombardment. *Advances in electronics and electron physics*, **7**, 239–298.

Wiberg, E., Goeltzer, H., and Bauer, R. (1951). Synthesis of MgH from the Elements. *Zeitschrift für Naturforschung. B*, **6**, 394–395.

Yamamoto, K., Higuchi, K., Kajioka, H., Sumida, H., Orimo, S., and Fujii, H. (2002). Optical transmission of magnesium hydride thin film with characteristic nanostructure. *Journal of Alloys and Compounds*, **330**, 352–356.

Yan, Y., Lin, X., Yang, S., Blake, A. J., Dailly, A., Champness, N. R., Hubberstey, P., and Schröder, M. (2009). Exceptionally high H_2 storage by a metal–organic polyhedral framework. *Chem. Commun.*, (9), 1025.

Yang, W. N., Shang, C. X., and Guo, Z. X. (2010). Site density effect of Ni particles on hydrogen desorption of MgH_2. *International Journal of Hydrogen Energy*, **35**(10), 4534–4542.

Ye, S. Y., Chan, S. L. I., Ouyang, L. Z., and Zhu, M. (2010). Hydrogen storage and structure variation in Mg/Pd multi-layer film. *Journal of Alloys and Compounds*, **504**(2), 493–497.

Yoshimura, K., Yamada, Y., and Okada, M. (2004). Hydrogenation of Pd capped Mg thin films at room temperature. *Surface Science*, **566-568**, 751–754.

Zahiri, B., Amirkhiz, B. S., and Mitlin, D. (2010). Hydrogen storage cycling of MgH_2 thin film nanocomposites catalyzed by bimetallic Cr Ti. *Appl. Phys. Lett.*, **97**(8), 083106.

Zahiri, B., Danaie, M., Tan, X., Amirkhiz, B. S., Botton, G. A., and Mitlin, D. (2012). Stable Hydrogen Storage Cycling in Magnesium Hydride, in the Range of Room Temperature to 300 °C, Achieved Using a New Bimetallic Cr-V Nanoscale Catalyst. *J. Phys. Chem. C*, pages 3188–3199.

Zaluska, A. and Zaluski, L. (1999). Nanocrystalline magnesium for hydrogen storage. *Journal of Alloys and Compounds*, pages 1–9.

Zaluska, A., Zaluski, L., and Ström-Olsen, J. O. (2001). Structure, catalysis and atomic reactions on the nano-scale: a systematic approach to metal hydrides for hydrogen storage. *Appl Phys A*, **72**(2), 157–165.

Zaluski, L., Zaluska, A., Tessier, P., Ström-Olsen, J. O., and Schulz, R. (1995a). Catalytic effect of Pd on hydrogen absorption in mechanically alloyed Mg_2Ni, LaN_5 and FeTi. *Journal of Alloys and Compounds*, **217**(2), 295–300.

Zaluski, L., Zaluska, A., and Ström-Olsen, J. O. (1995b). Hydrogen absorption in nanocrystalline Mg_2Ni formed by mechanical alloying. *Journal of Alloys and Compounds*, **217**(2), 245–249.

Zaluski, L., Zaluska, A., and Ström-Olsen, J. O. (1997). Nanocrystalline metal hydrides. *Journal of Alloys and Compounds*, **253**, 70–79.

Züttel, A. (2004). Hydrogen storage methods. *Naturwissenschaften*, **91**(4), 157–172.